

Biplanar Fluoroscopic Analysis of in vivo Hindfoot Kinematics During Ambulation

Janelle Ann Cross
Marquette University

Recommended Citation

Cross, Janelle Ann, "Biplanar Fluoroscopic Analysis of in vivo Hindfoot Kinematics During Ambulation" (2015). *Dissertations (2009 -)*. 558.
https://epublications.marquette.edu/dissertations_mu/558

BIPLANAR FLUOROSCOPIC ANALYSIS OF *IN VIVO* HINDFOOT KINEMATICS
DURING AMBULATION

by

Janelle A. Cross, M.S.

A Dissertation submitted to the Faculty of the Graduate School,
Marquette University,
in Partial Fulfillment of the Requirements for
the Degree of Doctor of Philosophy

Milwaukee, Wisconsin

August 2015

ABSTRACT
BIPLANAR FLUOROSCOPIC ANALYSIS OF *IN VIVO* HINDFOOT KINEMATICS
DURING AMBULATION

Janelle A. Cross, M.S.

Marquette University, 2015

The overall goal of this project was to develop and validate a biplanar fluoroscopic system and integrated software to assess hindfoot kinematics. Understanding the motion of the foot and ankle joints may lead to improved treatment methods in persons with foot and ankle pathologies. During gait analysis, skin markers are placed on the lower extremities, which are defined as four rigid-body segments with three joints representing the hip, knee and ankle. This method introduces gross assumptions on the foot and severely limits the analysis of in depth foot mechanics. Multi-segmental models have been developed, but are susceptible to skin motion artifact error. Intra-cortical bone pins studies provide higher accuracy, but are invasive. This dissertation developed and validated a noninvasive biplane fluoroscopy system to overcome the skin motion artifacts and rigid-body assumptions of conventional foot motion analysis.

The custom-built biplane fluoroscopy system was constructed from two fluoroscopes separated by 60°, attached to a custom walkway with an embedded force plate. Open source software was incorporated to correct the image distortion and calibrate the capture volume. This study was the first that quantified the cross-scatter contamination in a biplane fluoroscopic system and its effects on the accuracy of marker-based tracking. A cadaver foot study determined the static and dynamic error of the biplane fluoroscopic system using both marker-based and model-based tracking algorithms. The study also developed *in vivo* 3D kinematic models of the talocrural and subtalar joints during the stance phase of gait.

Cross-scatter degradation showed negligible effects in the smallest phantom, suggesting negligible motion tracking error due to cross scatter for distal extremities. Marker-based tracking error had a maximum absolute mean error of 0.21 (\pm 0.15) in dynamic trials. Model-based tracking results compared to marker-based had an overall dynamic RMS average error of 0.59 mm. Models were developed using custom algorithms to determine talocrural and subtalar joint 3D kinematics. The models offer a viable, noninvasive method suitable for quantifying hindfoot kinematics. Patients with a variety of adult and pediatric conditions which affect foot and ankle dynamics during walking may benefit from this work.

ACKNOWLEDGMENTS

Janelle A. Cross, M.S.

I would like to thank my dissertation director, Dr. Taly Gilat-Schmidt for her unwavering support and assistance during my time at Marquette. I am extremely grateful for all the time she put into our weekly meetings, numerous writing edits, and vast amount of emails answered. I would also like to thank my academic adviser and dissertation committee member, Dr. Gerald Harris for his guidance and mentorship throughout my academics and extending into starting my career. I feel very lucky to have had two great leaders throughout this process.

I would also like to thank the other members of my dissertation committee, Dr. Philip Voglewede, Dr. Jason Long, and Dr. Peter Smith. Your input and expertise was instrumental in the completion of this work. Additionally, I would like to give a special thanks to Dr. Ben McHenry for his invaluable support and leadership throughout this project.

Thank you to the staff of the Biomedical Engineering department and the Orthopaedic and Rehabilitation Engineering Center at Marquette University. Also, thank you to my colleagues for their assistance in the laboratory during numerous data collections.

Finally, I would like to thank my family, especially my parents, for their unconditional love and support throughout my educational adventures. Your endless encouragement helped me persevere to achieve my ultimate goal.

The contents of this dissertation were developed under a grant from the National Institute on Disability, Independent Living, and Rehabilitation Research (NIDILRR grant number 90RE5006-01-00). NIDILRR is a Center within the Administration for Community Living (ACL), Department of Health and Human Services (HHS). The contents of this dissertation do not necessarily represent the policy of NIDILRR, ACL, HHS, and you should not assume endorsement by the Federal Government.

TABLE OF CONTENTS

ACKNOWLEDGMENTS	i
LIST OF TABLES	v
LIST OF FIGURES	vi
LIST OF ABBREVIATIONS	viii
1. INTRODUCTION	2
1.1 Statement of Problem.....	2
1.2 Hindfoot Anatomy	3
1.2.1 Bones and Articulating Surfaces.....	4
1.2.2 Joints and Axis of Motion.....	8
1.2.3 Actions of Ankle and Subtalar Joint during Gait.....	9
1.2.4 Cadaver Foot Studies	10
1.3 External Marker-based Models.....	11
1.3.1 Skin Motion Artifact.....	11
1.3.2 Model Repeatability.....	13
1.3.3 Rigid Segment Assumption	14
1.3.4 Segmental Foot Models	14
1.3.5 Shod and Orthosis Conditions	15
1.4 Bone Pin Models.....	16
1.5 Alternative Imaging Techniques.....	16
1.5.1 Computer Tomography (CT) and Magnetic Resonance (MR) Imaging.....	16
1.5.2 Roentgen Stereophotogrammetric Analysis	17
1.5.3 Single Plane Fluoroscopy	18
1.6 Biplane Fluoroscopic Techniques.....	19
1.6.1 Hardware.....	20
1.6.2 Calibration.....	21
1.6.3 Marker-based Tracking.....	22
1.6.4 Model-based Tracking	23
1.6.5 Fluoroscopic System Validation	26

1.7	Foot and Ankle Fluoroscopy.....	26
1.8	Objectives	28
1.9	Specific Aims.....	28
2.	DEVELOPMENT OF BIPLANE FLUOROSCOPY SYSTEM	30
2.1	Biplane Fluoroscopy System	30
2.2	System Synchronization.....	31
2.3	Exposure of System	32
2.4	Image Distortion Correction	33
2.5	Geometric Calibration.....	34
3.	QUANTIFYING CROSS-SCATTER CONTAMINATION IN BIPLANE FLUOROSCOPY MOTION ANALYSIS SYSTEMS.....	36
3.2	Methodology	36
3.2.1	Phantoms and X-ray Settings.....	36
3.2.2	Scatter Fraction and Contrast-to-Noise Ratio	37
3.2.3	Effects of Gantry Angle on Cross-Scatter	38
3.2.4	Effects of Cross-Scatter on Marker-based Tracking Accuracy	39
3.3	Results.....	40
3.4	Discussion	44
3.5	Conclusion	47
4.	MARKER AND MODEL-BASED VALIDATION OF A BIPLANE FLUOROSCOPIC SYSTEM FOR HINDFOOT ANALYSIS	48
4.2	Methods.....	48
4.2.1	Cadaver Specimen	48
4.2.2	CT Scan.....	49
4.2.3	Static and Dynamic Trials.....	50
4.2.4	Marker-based Tracking.....	51
4.2.5	Model-based Tracking	52
4.3	Results.....	53
4.4	Discussion.....	58
5.	KINEMATIC MODEL FOR ASSESSMENT OF IN VIVO HINDFOOT MOTION DURING GAIT	63
5.2	Methods.....	63

5.2.1 ACS Definitions.....	63
5.2.2 Model Simulation.....	65
5.2.3 Model-based Tracking Method.....	66
5.2.4 Kinematic Models.....	66
5.3 Results.....	67
5.4 Discussion.....	69
6. CONCLUSION.....	72
6.1 Summary of Findings.....	72
6.2 Limitations and Future Work.....	74
BIBLIOGRAPHY.....	78
Appendix A. Steps for Model-Based Biplane Fluoroscopy.....	91
Appendix B. Using Geomagic to Define Anatomical Coordinate Systems.....	99
Appendix C. Marker-based Static Tracking Error Results.....	119
Appendix D. Static Validation: Bias, Precision, RMS.....	124
Appendix E. Dynamic Validation: Bias, Precision, RMS.....	127
Appendix F. User Error: Bias, Precision, RMS.....	128

LIST OF TABLES

Table 1: Exposure measurements of biplane system with fluoroscopy units turned on for 2 seconds.....	32
Table 2: Static and dynamic tracking mean error and SD for images acquired with cross scatter.....	44
Table 3: Marker-based absolute mean tracking error and standard deviation (SD) in mm....	54
Table 4: Model-based tracking accuracy for individual bones (bias and precision reported in mm and SD).....	55
Table 5: Model-based tracking accuracy for individual bones (RMS error reported in mm and SD).	56
Table 6: Talocrural and subtalar joint maximum angles during stance phase (°).....	69

LIST OF FIGURES

Figure 1: Medial and superior view of talus.	4
Figure 2: Medial and superior view of calcaneus.	5
Figure 3: Anterior and inferior view of tibia.	7
Figure 4: Axes of talocrural and subtalar joint.	9
Figure 5: Sketch of a biplane fluoroscopic system with embedded force plate.....	20
Figure 6: Flow chart of model-based tracking method (2).	25
Figure 7: Custom-built biplane fluoroscopy system with x-ray sources attached to right-hand side of walkway and image intensifiers attached to left-hand side. The embedded force plate is placed where x-ray beams intersect.	31
Figure 8: A) Raw, distorted calibration frame. B) Frame after distortion correction. C) Raw, distorted image of phantom foot. D) Foot after distortion correction algorithm applied.....	34
Figure 9: A) Image of 64-point calibration cube. B) Fluoroscopic image of calibration cube. Radiopaque markers were used to identify the beads in the fluoroscopic image.....	35
Figure 10: X-ray images of a) 4-in phantom primary+scatter image and b) 4-in phantom primary+scatter+cross_scatter image displayed at the same window/level settings. c) 10-in phantom primary+scatter image and d) 10-in phantom primary+scatter+cross_scatter image displayed at the same window/level settings.	40
Figure 11: Measured cross-scatter fraction for all phantoms across a range of tube settings. Error bars, representing standard deviation, are smaller than the markers and thus are not visible.	41
Figure 12: Comparison of CSF measured experimentally and estimated through simulations for a gantry angle of 60 degrees. Error bars represent one standard deviation. ..	42
Figure 13: Cross-scatter fractions plotted for gantry angles of 60, 75, and 90-degrees for the 8-in and 10-in phantoms at a range of tube settings, as estimated through simulations...	43
Figure 14: Static tracking error (in mm) between no cross scatter and with cross scatter.	43
Figure 15: Cadaver specimen with steel rod attached to tibia via bone plate.....	49

Figure 16: A) 11 static foot progression angles. B) Grid used for translational measurements.....	51
Figure 17: Manual verses automated model-based tracking across 10 dynamic trials.....	57
Figure 18: Intra-observer user error of model-based tracking ten times for one dynamic trial.	58
Figure 19: Anatomical coordinate system of the bones. Medial and superior views of the calcaneus (A), talus (B), and tibia (C).	65
Figure 20: Talocrural and subtalar joint kinematics during stance phase. Solid lines represent mean of all 10 trials. Dashed lines represent mean \pm 1 standard deviation. The morphology of the talocrural joint plantar/dorsiflexion curve was similar to results found in a 2D fluoroscopy study with human subjects (102).	68
Figure 21: Pilot fluoroscopic image of foot with F-Scan plantar pressure.	76

LIST OF ABBREVIATIONS

2D	Two-Dimensional	II	Image Intensifier
3D	Three-Dimensional	ISB	International Society of Biomechanics
ABD	Abduction	INV	Inversion
ACS	Anatomical Coordinate System	JCS	Joint Coordinate System
ADD	Adduction	kV	Kilovoltage
AJC	Ankle Joint Complex	LCS	Local Coordinate System
AP	Anteroposterior	mA	Milliampere
BW	Body Weight	MFM	Milwaukee Foot Model
CNR	Contrast-to-Noise Ratio	ML	Mediolateral
CSF	Cross-scatter Fraction	MR	Magnetic Resonance
CT	Computed Tomography	MS	Mid Stance
DF	Dorsiflexion	PF	Plantarflexion
DOF	Degree(s) Of Freedom	ROI	Region of Interest
DRR	Digitally Reconstructed Radiograph	ROM	Range of Motion
DLT	Direct Linear Transform	RSA	Roentgen Stereophotogrammetric Analysis
EV	Eversion	SD	Standard Deviation
FF	Foot Flat	SI	Superoinferior
FOV	Field Of View	SMA	Skin Movement Artifact
FP	Force plate	Sv	Sievert
FPS	Frames per Second	TO	Toe Off
GCS	Global Coordinate System	XROMM	X-Ray Reconstruction of Moving Morphology
HS	Heel Strike		
HR	Heel Rise		

1. INTRODUCTION

1.1 Statement of Problem

Dynamic assessment of skeletal kinematics and kinetics is necessary for understanding normal joint function, in addition to effects of injury or disease (1, 2). For lower extremity evaluation, external optical markers are typically placed on specific bony landmarks on the skin so that video cameras can track the motion of the underlying bones (3-5). Software is used to define the markers in a program as a sequence of four rigid-body segments of the pelvis, thigh, shank, and foot with three universal rotary joints representing the hip, knee, and ankle joints (6). Conventional gait analysis has been validated and is used frequently in research and clinical settings (6-8).

Although these optical motion analysis systems are easy to implement and are clinically relevant for several applications, they have issues that need to be addressed when looking more in depth at the foot. Conventional methods do not allow for obtaining intertarsal kinematics or kinetics of the hindfoot. A single rigid body assumption of the foot fails to take into account the major joints and can lead to errors regarding subtalar joint kinematics, especially when applied to the deformed foot (9, 10). It has been found that the most significant source of error in gait analysis is skin movement artifact (SMA) (3, 11). When the markers are placed on the surface of the skin, a motion artifact is introduced that has the potential to greatly affect the kinetics results to estimate the dynamic loads in joints (1).

Understanding the biomechanics of the tarsal complex during gait is critical to the proper care of patients with a variety of orthopaedic impairments. Orthopaedic disorders, such as cerebral palsy or myelomeningocele, often require lower extremity orthoses for

ambulation. Due to obscuring of skin markers, gait analysis to determine the joint kinematics and kinetics cannot be performed with conventional optical methods while wearing braces, orthoses, or modified footwear. Markers placed directly on the shoe remain visible, but data from these markers will not adequately measure the motion of the foot within the shoe. This limitation of optical imaging systems has prevented the analysis of motion of the foot during gait in patients who require orthoses or modified footwear for functional ambulation. The ability to look “inside the shoe” during ambulation is required to provide better means of quantifying the motion and loading patterns of the hindfoot.

Fluoroscopic methods have been introduced for use in gait analysis to aid in eliminating SMA by looking at the motion of the bones directly. X-ray fluoroscopy acquires a time sequence of images while performing a dynamic movement (12). While fluoroscopy is limited to a small field of view, typically allowing for single joint analysis, and has extensive image data processing, it is noninvasive and provides complete three-dimensional (3D) analysis of joints. The ability to track the bones of the foot directly would also greatly reduce the rigid body assumptions. The purpose of this study was to develop and validate a biplane fluoroscopic system that performs dynamic *in vivo* assessment of subtalar joint kinematics. The ability to directly analyze the bones and joints within the body to attain reliable *in vivo* kinematics is beneficial for research in several fields.

1.2 Hindfoot Anatomy

1.2.1 Bones and Articulating Surfaces

The foot contains 26 bones, 33 joints, 107 ligaments and 19 muscles that allow for intricate multiplanar motion (13). The bones of the foot are clustered into 3 groups: 7 tarsal bones, 5 metatarsals, and 14 phalanges (14). The tarsal group consists of the talus, calcaneus, navicular, cuboid, and the medial, intermediate and lateral cuneiforms. The focus of this project is the hindfoot, which is comprised of the talus and calcaneus, along with the lower leg bones, the tibia and fibula.

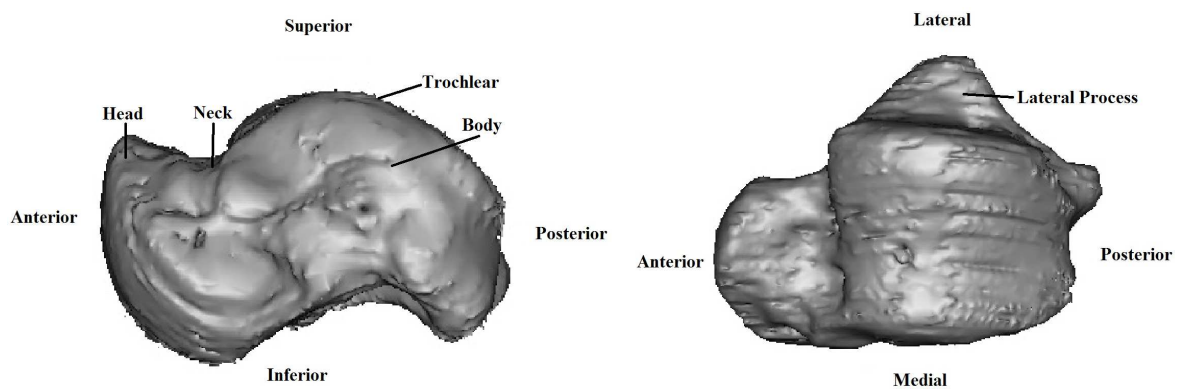


Figure 1: Medial and superior view of talus.

The talus (Figure 1) has a rounded head, projected anteriorly and medially by a short broad neck, which is connected posteriorly to an expanded body (14). The anterior surface of the head is convex for articulation with the navicular. The convex surface extends inferiorly to form three articular facets separated by smooth ridges. The anterior and middle facets articulate with adjacent surfaces on the calcaneus. The other facet is medial to the calcaneal articulations and articulates with the spring ligament. The neck of the talus has a deep groove, the sulcus tali, which passes obliquely forward across the

inferior surface from medial to lateral, and expands dramatically on the lateral side (14). Posterior to the sulcus tali is a large facet for articulation with the calcaneus.

The superior surface of the talus body, called the trochlear, is elevated to fit into the socket formed by the distal ends of the tibia and fibula and articulates with the inferior end of the tibia. The medial surface articulates with the tibia and the lateral surface articulates with the fibula. The lateral articulating surface is larger and projects more inferiorly than the medial surface (14). The lower part of the lateral surface forms the bony projection called the lateral process, which supports the facet for articulation with the fibula. The inferior surface of the body has a large oval concave facet for articulation with the calcaneus. The posterior aspect of the body consists of the posterior process, a posterior and medial facing projection. Its surface has lateral and medial tubercles, which bracket a groove for the flexor hallucis longus tendon (14). There are no muscle insertions on the talus bone (15).

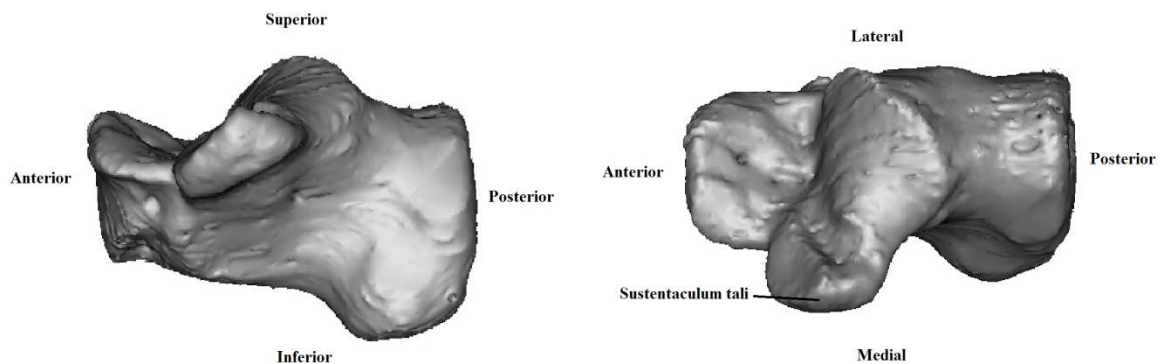


Figure 2: Medial and superior view of calcaneus.

The calcaneus (Figure 2) is an elongated, irregular, box-shaped bone with its long axis generally orientated along the midline of the foot, but deviates laterally to the

midline anteriorly (14). It is the largest tarsal bone, which sits under and supports the talus. The calcaneus projects posteriorly behind the talocrual joint to form the heel. The posterior surface is circular and divided into upper, middle and lower parts. The upper part is separated from the calcaneal tendon by a bursa. The lower part, the weight bearing region of the heel, curves anteriorly and is continuous onto the plantar surface of the bone as the calcaneal tuberosity (14). The tuberosity has a large medial process and small lateral process, separated by a v-shaped notch. The anterior end of the plantar surface of the calcaneus has the calcaneal tubercle for the posterior attachment of the short plantar ligament.

The lateral surface of the calcaneus has a smooth contour except for two slightly raised regions. One region, the fibular trochlea, is anterior to the middle of the surface and has two shallow grooves that pass obliquely across its surface. The second region is superior and posterior to the fibular trochlea. It serves as an attachment site for the lateral collateral ligament. The medial surface of the calcaneus is concave and has one prominent feature, the sustentaculum tali, which is a shelf of bone projected medially and supporting the posterior part of the head of the talus (14). The superior surface of the sustentaculum tali has a facet for articulating with the middle facet on head of the talus.

The superior surface of the calcaneus has two articulating surfaces. The anterior talar articular surface is small and articulates with the anterior facet on the head of the talus. The posterior talar articular surface is large and is approximately near the middle of the superior surface of the calcaneus. Between the posterior talar articular surface and the middle and anterior talar articular surfaces is the calcaneal sulcus, a deep groove running medial-laterally across the calcaneus. The calcaneal sulcus and the sulcus tali on the talus

together form the tarsal sinus, a large gap visible laterally between the anterior calcaneus and talus (14).

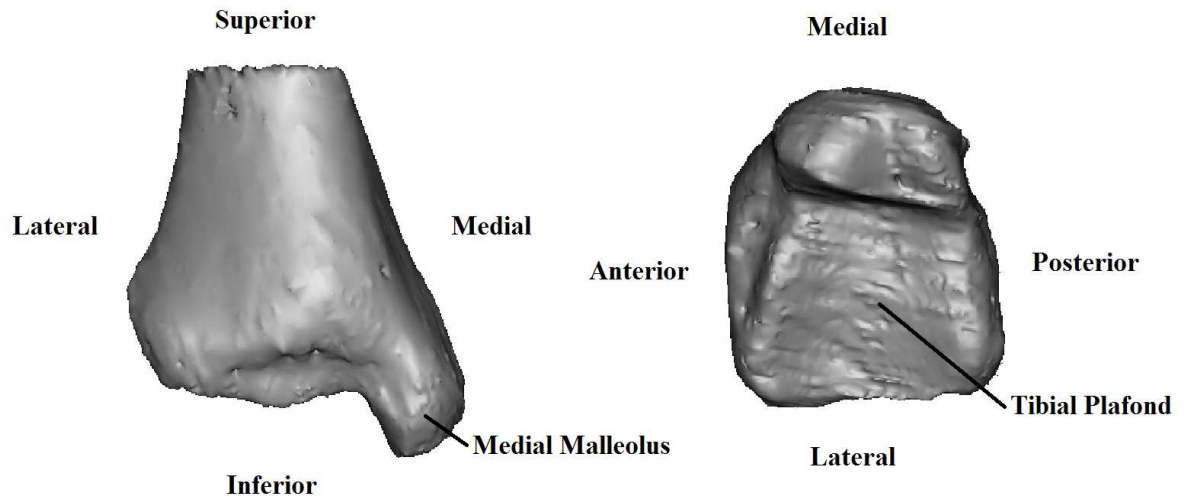


Figure 3: Anterior and inferior view of tibia.

The tibia (Figure 3) is the weight bearing bone of the lower leg. The cross-section of the shaft is triangular, while the distal end is rectangular with a bony protuberance on the medial side, the medial malleolus (14). The inferior surface of the tibia, the tibial plafond, along with the medial malleolus articulates with the talus to form a large part of the talocrural joint. The lateral surface of the distal tibia has the fibular notch, where the distal head of the fibula is anchored by a thickened part of the interosseous membrane (14). The fibula is lateral to the tibia and much smaller in size. Its shaft cross-section is also triangle, expanding distally to form the spade-shaped lateral malleolus. The medial surface of the lateral malleolus has a facet for articulation with the talus, forming the lateral part of the talocrural joint.

1.2.2 Joints and Axis of Motion

The talocrural joint (Figure 4) is often referred to as the ankle joint. The tibia and fibula create a deep bracket-shaped socket for the trochlear surface of the talus. The ankle axis passes through the body of the talus, just above the talo-calcaneal articulation (16, 17). The oblique axis of the ankle is rotated laterally downward 82° from the tibial midline in the frontal plane, and runs laterally and posteriorly $20\text{-}30^\circ$ in the transverse plane, from the medial malleolus to the lateral malleolus (10). The superior surface of the talus is much wider anteriorly than posteriorly. As a result, the bone fits tighter into the socket when the foot is dorsiflexed when the wider surface moves into the joint. Thus, the talocrural joint is most stable when the foot is dorsiflexed (14).

The talocalcaneal joint (Figure 4), typically called the subtalar joint, is between the large posterior calcaneal facet of the talus and the posterior talar facet of the calcaneus. The joint allows for gliding and rotation. The subtalar joint has an oblique axis that runs approximately from antero-medio-superior to postero-latero-inferior through the talus and calcaneus (16-19). This axis forms an angle 42° (10, 19, 20) to 45° (16, 17, 21) from horizontal in the sagittal plane of the foot, and a 16° (16) to 23° (10, 15, 21) from the foot midline in the transverse plane. These angles can vary subject to subject and change the joint range of motion (ROM).

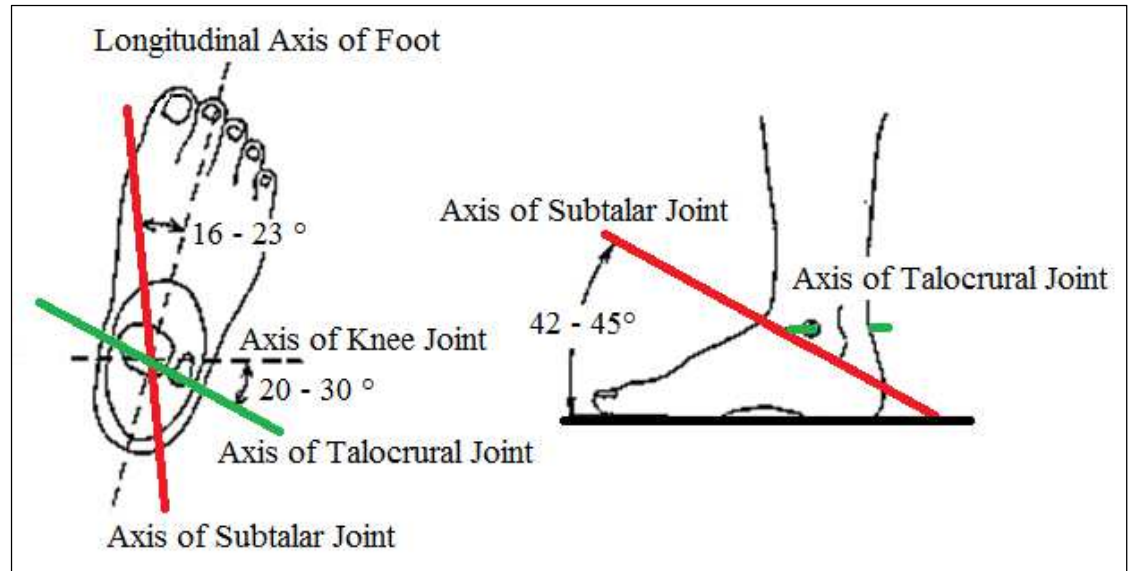


Figure 4: Axes of talocrural and subtalar joint.

The ankle joint is primarily responsible for sagittal plane motions (dorsiflexion/plantar flexion). The subtalar joint is primarily responsible for motions in the frontal plane (inversion/eversion) and the transverse plane (abduction/adduction). The actions are often combined when the ankle and subtalar joint work together as the ankle joint complex (AJC) to generate pronation (dorsiflexion, eversion, abduction) and supination (plantarflexion, inversion, adduction). The triplanar motions of the AJC are further complicated due to the joint axes not being in any of the cardinal planes of motion. A method to locate the talus during gait analysis would allow for more advanced subtalar motion assessment and a more accurate estimate of the subtalar kinematics and kinetics than current models.

1.2.3 Actions of Ankle and Subtalar Joint during Gait

The gait cycle consists of the stance phase (when the foot is in contact with the ground) and swing phase (when the limb is swinging forward) (22). The stance phase is approximately 60% of the gait cycle and has 5 major events: heel strike (HS), foot flat (FF), mid-stance (MS), heel rise (HR), and toe off (TO) (17, 22). The foot must perform various important functions at specific times during the gait cycle for normal ambulation.

At HS, the ankle joint is either in neutral or slightly plantarflexed (22). The foot must be flexible to adjust to the ground surface and simultaneously assist the body's shock absorbing mechanism (22, 23). Heel contact with the ground is lateral to the ankle joint, where the body weight (BW) is transmitted to the talus, creating a pronation moment at the subtalar joint. The talus rotates medially on the calcaneus about the subtalar axis, forcing the calcaneus into pronation (22). Immediately following HS, the foot flexes to the floor, controlled by the dorsiflexors to prevent the foot from slapping down to the FF position (22). At FF, the lower limb begins to rotate laterally, transmitting the lateral rotation to the talus as well. As lateral rotation continues, the foot goes into supination, increasing the stability at the transverse tarsal joint. During MS, the foot needs to be rigid to enable BW to be carried with sufficient stability (22). After HR, the ankle joint moves back into plantarflexion. Just before TO, the combination of weight bearing and supination ensures that the foot is in a maximally stable position for lift-off (22). At TO, the foot must function as a lever to propel the body across the ground (22, 23).

1.2.4 Cadaver Foot Studies

Foot cadaver studies have been performed to determine the relative kinematics and kinetics of the foot during the stance phase of gait (16, 24-29). In 1998, Sharkey and Hamel performed a cadaver study using a dynamic gait simulator to validate the utility of their foot kinetic model (25). Also in 1998, Parenteau et al. assessed the biomechanical properties of cadaveric ankle and subtalar joints in quasi-static loading conditions (26). In their study, the cadaver foot specimens were cemented in a jig upside down, with the calcaneus pinned so that the sole response of the testing was through the ankle and subtalar joints. More advanced kinematics testing was performed by Hamel et al. in 2004 and Nester et al. in 2007 using dynamic gait simulators and markers drilled directly into the cadaver specimen bones (28, 30). The dynamic gait simulator uses the cadaver limb to mimic normal kinetics and kinematics of the tibia, foot and ankle during the stance phase of gait from HS to TO. In both studies, marker clusters were attached to K-wires drilled into the tibia, talus and calcaneus. The results demonstrated the extent to which rigid segment assumptions of conventional skin marker models have oversimplified the foot (30). Cadaver studies have shown potential for often-ignored foot joints to contribute significantly to the overall function of the foot.

1.3 External Marker-based Models

1.3.1 Skin Motion Artifact

Skin movement artifacts (SMA) are due to the relative movement between markers and underlying bone. These movements can be caused by the non-rigid attachment of skin to bone, muscle contractions underneath skin, and inertial effects (3). Various invasive and noninvasive methods have been used to directly measure in vivo

skeletal motion in an effort to eliminate SMA. These methods include bone pins (29, 31, 31-36), external fixation devices (3), percutaneous skeletal tracker (37), and imaging techniques (11, 38, 39). Studies using intra-cortical bone pins attached to bones in the lower extremities have found significant differences in angular displacements about all axes of rotation and displacements of skin markers relative to underlying bone of up to 20 mm (32, 33). A bone pin study involving the foot found that skeletal markers are only gross indicators of the skeletal tibiocalcaneal motion, with a typical overestimate of skeletal kinematics by 46.3% using external markers (31). A study that used external fracture fixation devices on the tibia found skin marker displacements of the lateral malleolus to be 15 mm in all directions (3).

Imaging techniques offer a way to simultaneously visualize skin markers and bone motion during activity. Roentgen photogrammetry has been used to track the relative skin movement of the foot in 2D (39). Marker movement varied from 1.8 to 4.3 mm, with the largest movements occurring more proximally to the malleoli. In another study involving the foot and ankle, the two malleoli markers showed the largest artifact with the mean displacement between skin markers and bones varying from 2.7 to 14.9 mm (40). Single plane fluoroscopy was used to quantify the SMA of a multi-segment foot model using triad cluster markers (34). The translational results of SMA ranged from 6.46 to 16.72 mm, with maximal error occurring at the toe-off position. These results indicate that skin markers placed on bony landmarks of the foot may not be suitable for accurate kinematic analysis of foot motion. The current study used biplane fluoroscopy to eliminate the SMA of tracking bones within the foot.

1.3.2 Model Repeatability

When skin-mounted optical markers are used, model repeatability is a concern because of how the markers define the segments and joints. Several markers in lower extremity models are placed on bony landmarks. The incorrect location of bony landmarks can be caused by: the palpable landmarks are not points but surfaces, soft tissue layer of variable thickness covering the landmark, and the palpation technique used to find the bony landmark (41, 42). The precision and accuracy of bony landmark locations is essential, as they affect the segment orientation and the LCS, as well as the sensitivity of joint kinematic variables (41). A model needs to repeatedly generate accurate results intra-subject, inter-subject, within-day testing, between-day testing, intra-examiner, and inter-examiner. It is critical that the model used is repeatable so that the performed single gait evaluation is representative of a subjects' overall gait performance (43).

In multi-segmental foot models, the external skin markers need to be placed in very specific locations to define the segment center of mass and coordinate system. In the five segmental shank-foot model developed by Leardini et al., inter-subject repeatability tests suggest that the protocol was not repeatable for all the joints (44). While Carson et al. found their four segment foot model to have good repeatability between trials, they had low repeatability between different days and different testers (4). Long et al. performed a validation study involving the use of the four segment Milwaukee foot model (MFM) between test sites (45). The MFM uses weight bearing x-rays to orientate the skin-mounted markers to the orientation of the underlying bony anatomy. Their results showed minimal inter-site differences in foot kinematics, with the largest source

of variability from inter-subject testing (45). The method using biplane fluoroscopy avoids inter-subject repeatability errors and inter-tester repeatability errors by eliminating the need for external markers.

1.3.3 Rigid Segment Assumption

External marker based systems that define multiple bones as a single segment make the assumption that the bones do not move with respect to one another. Violation of the rigid body assumption may lead to overestimated inter-segmental motion, unreported intra-segmental motion, or attributing motion to one joint when in fact it occurs at another (46). Conventional motion analysis models combine the ankle and subtalar joints as a single joint and describe the motion as that of a single rigid segment foot with respect to the tibia. Unlike other segments of the lower extremity, the foot is composed of multiple bones and joints with complex interaction (47). Cadaver studies, discussed in Section 1.2.4, have confirmed the complexity of foot kinematics and the potential for often ignored foot joints to contribute significantly to the overall kinematics. A single rigid segment is a gross assumption of the foot anatomy and function that may violate the rigid body assumption in current foot models. The current study avoided rigid segment assumptions by tracking the calcaneus, talus, and tibia directly to determine joint kinematics.

1.3.4 Segmental Foot Models

To overcome issues associated with modeling the foot as a single rigid body, the foot was subdivided further into multiple segments. Numerous multi-segment foot

models dividing the foot and ankle into anywhere between two to nine segments have been developed to aid in better analysis of the foot during gait (4, 5, 9, 44, 48-55). These models use external markers that define multiple bones of the foot as one or more rigid body segment and assume that the bones do not move with respect to one another. To define a rigid segment, three non-collinear markers are required. Finding palpable locations to place the markers becomes increasingly difficult as the segments get smaller or deeper within the foot. While dividing the foot into multiple segments allows for better analysis of the major joints of the foot, it still has sources of error from SMA, and the violation of rigid body assumption (46, 47). Again, the current study avoided the issues associated with segmental models by tracking the individual bones of the foot.

1.3.5 Shod and Orthosis Conditions

Foot orthoses and shoe modifications can play an important role in noninvasive management of foot and ankle pathologies. Orthopaedic disorders, such as cerebral palsy and myelomeningocele, often require lower extremity braces or shoe modifications for walking (56). Therapeutic shoe wear may be used to treat patients with diabetes, arthritis, neurologic conditions, traumatic injuries or congenital deformities (57, 58). Rocker sole shoe modifications are designed to relieve plantar pressure by altering the motion and force distribution patterns of the foot (58-60). Motion analysis to determine the joint motion and forces cannot typically be performed with conventional optical methods while wearing braces, orthoses, or modified footwear due to their interference with external markers. Although numerous methods have been attempted, they currently limit the validity of measurement in the form of either structural modifications of footwear or

surface marker applications to the external shoe surface (61). Describing foot movement within footwear during ambulation is required to provide better means of quantifying the motion and loading patterns. Fluoroscopy provides dynamic motion measurements within shoes that are otherwise difficult to achieve.

1.4 Bone Pin Models

Bone pin foot models have been developed to circumvent the errors associated with external markers by surgically attaching pins directly to the bone, thus eliminating SMA and marker misplacement (29, 31, 36, 62-64). This method requires the assistance of an experienced orthopaedic surgeon and the use of local anesthesia. Bone pin studies have been performed to analyze hindfoot kinematics during walking (62, 64). These studies are limited due to their invasive nature, possible pain and discomfort for the subjects, influences on the natural gait pattern through anesthetic or soft tissue impingement, and have a risk of infection at the insertion site (33, 62). They are also limited by low subject numbers. Although the current study had low dose radiation exposure, it was noninvasive to the patients and does not cause gait pattern alterations.

1.5 Alternative Imaging Techniques

1.5.1 Computer Tomography (CT) and Magnetic Resonance (MR) Imaging

Imaging methods that allow direct 3D imaging of *in vivo* joint morphology, such as computed tomography (CT) and magnetic resonance (MR) imaging, have been used to study various joints (65-74). While these methods provide noninvasive joint motion analysis, they are expensive and restrict the joint to one position during the CT or MR

scan, preventing the quantification of full motion kinematics during various functional activities (72). Another issue with CT is the amount of effective dose the patient is exposed to. Effective dose is a dose descriptor that reflects the difference in potential biological effects from radiation based on the biological sensitivity of the tissue or organ irradiated (75). The typical effective dose of a chest CT and abdomen CT is 5 to 7 millisieverts (mSv), a pelvis CT is 3 to 4 mSv, and a head CT is 1 to 2 mSv (75). The effective dose during a foot and ankle CT scan is 0.07 mSv, which is slightly less than the 0.08 mSv of effective dose received from a conventional chest x-ray (76). Also, CT and MR images are generally not acquired under weight-bearing conditions and may be distorted in the presence of metal implants (77). While this study currently uses a single CT scan of the foot to generate the bone models, future work includes replacing the required CT with an MR scan to greatly reduce the effective dose patients receive during the analysis.

1.5.2 Roentgen Stereophotogrammetric Analysis

Roentgen stereophotogrammetric analysis (RSA) involves static x-ray imaging of joint implants or beads implanted into bones to determine their positions (78, 79). It was originally developed to measure prosthesis migration (79, 80). Single plane RSA, used in studying hip and knee prostheses, had an accuracy of 0.7 to 0.9 mm (12, 81). In a study of knee prostheses, biplane RSA was found to have accuracy as high as 10-250 μm (82). While RSA has demonstrated highly accurate determination of positioning, it is limited to static imaging and exposes the patient to high radiation dosage compared to x-ray fluoroscopy (83, 84).

1.5.3 Single Plane Fluoroscopy

Whereas RSA acquires biplane x-ray images at one time point, x-ray fluoroscopy acquires a time sequence of images (12). Fluoroscopic technology has been used for over a century for several medical applications. Single plane fluoroscopy allows direct visualization of underlying bones and has been used to track bone movements in animals (85), the forearm (86), fingers (87), spine (88), the knee (77, 89-94) and the ankle (72, 95-102). While fluoroscopy is limited to a small field of view, often a single joint at a time, and has extensive image data processing, it is noninvasive and provides complete 3D analysis of joints without SMA. An average testing procedure of 20 seconds has a radiation exposure of 100 μSv , which is equivalent to the approximate solar radiation exposure received on a 12 hour flight from London to Tokyo (103). The USNRC (United States Nuclear Regulatory Commission) places an annual occupational limit of whole body effective dose at 5 rems (50,000 μSv). In the United States, the average person is exposed to 3000 μSv every year from natural background radiation (104).

Single plane fluoroscopy uses a 3D to two-dimensional (2D) registration technique to match 3D models with x-ray images (86). The six kinematic parameters, three rotations and three translations, can be estimated for each frame. Single plane fluoroscopy is limited to 2D evaluation and is susceptible to out-of-plane errors and motion blur (1). The assessment of out-of-plane translations is unreliable and the accuracy for measuring out-of-plane translations is poor relative to accuracy for measuring in-plane translations (77, 105). Single plane fluoroscopy lacks the ability to capture accurate 3D motion during dynamic functional loading and should not be used to study joints that have combined motions in different planes (104). The unique system

developed in this project performed biplanar fluoroscopic analysis using two gantries to avoid the errors associated with single plane techniques.

1.6 Biplane Fluoroscopic Techniques

In biplane fluoroscopy, radiographic images are captured in two different planes, allowing for assessment of 3D joint motion. It has the potential to quantify six degrees of freedom (DOF) motion with high accuracy and has important applications to a wide range of problems in orthopaedics, sports medicine, and bioengineering (84). Typically, the accuracy of biplane fluoroscopy is higher compared to single plane, with both types of fluoroscopy systems having substantially higher accuracy compared to conventional skin marker techniques.

Biplane fluoroscopy has been used to determine motion in animals (1, 2, 106), the shoulder (107, 108), spine (104, 109, 110), hip (111), knee (112-116) and the ankle (117-123). A biplane study of the shoulder found a dynamic accuracy of ± 0.4 mm for translation and $\pm 0.5^\circ$ for rotation (107). Another biplane study of the cervical spine had high repeatability, with 0.02 mm error in translation and 0.06° error in rotation (104). A direct comparison between fluoroscopic studies is difficult due to differences in techniques, testing conditions, and software packages.

Figure 5 presents a diagram of a biplane fluoroscopy system. The two fluoroscopy gantries are separated by angle θ , allowing 3D localization in the region irradiated by both systems. A walkway containing a force plate (FP) enables kinetic analysis as well. Kinematic data from biplane fluoroscopy, along with patient specific models, can be used to calculate stress distributions and assess deformation to joint structures (124).

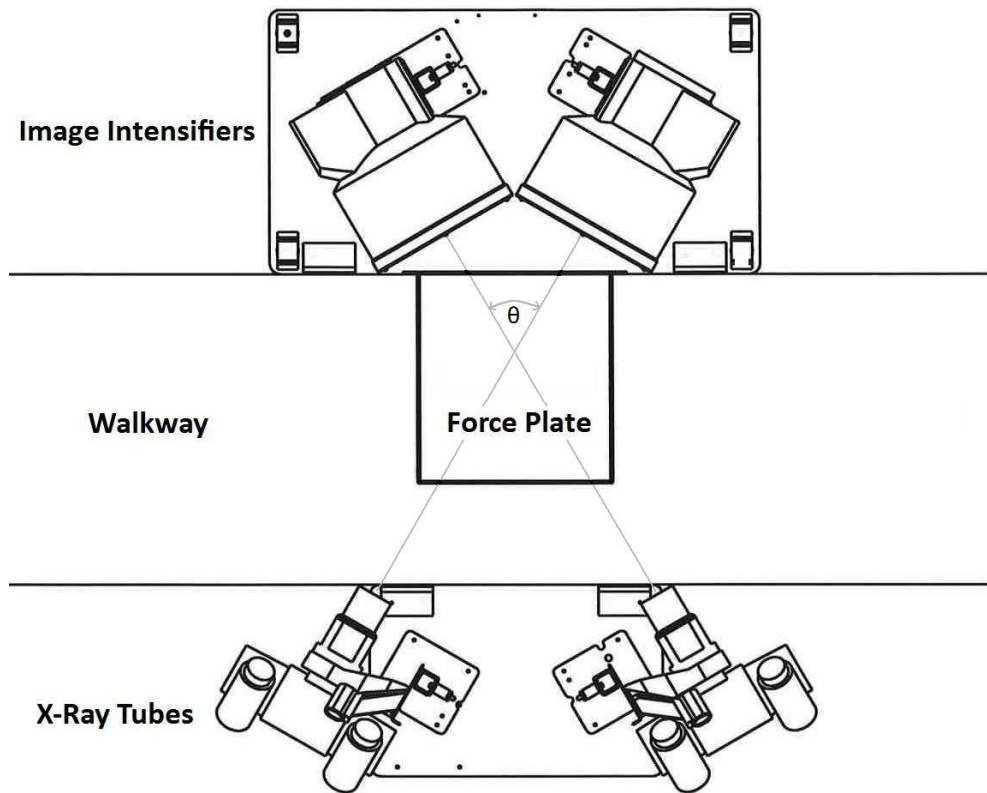


Figure 5: Sketch of a biplane fluoroscopic system with embedded force plate.

Four components are required to perform fluoroscopic gait analysis: 1) a hardware system for acquiring x-ray images; 2) software algorithms for tracking bones or markers; 3) a 3D model, generated from a CT or MR scan (for markerless or model-based tracking); 4) a set of kinematic equations for determining joint motion.

1.6.1 Hardware

Two x-ray fluoroscopes with an image intensifier (II) coupled to a high-speed video camera are typically used to acquire images. The fluoroscopes can be used in the standard C-arm configuration or a custom build gantry. High-speed cameras are typically shuttered and sampled at 250 frames per second (FPS) to reduce motion blur when recording joint motion (84). The settings for x-ray tube current (measured in milliamperes

or mA) and voltage (measured in kilovolts or kV) vary depending on the investigated joint and surrounding soft tissue. The voltage determines the energy distribution of the photons produced by the source, while the current determines how many photons are produced. When the voltage is increased, more photons are produced from the source, thus the current can be reduced to maintain the overall x-ray exposure (125). Lead vests or aprons are typically worn during testing to cover areas not being studied. Image quality is also affected by the beam energy, subject size, image intensifier size, and the distance from the patient to image intensifier (126). Positioning the patient closer to the image intensifier reduces the air gaps and may reduce image blur (84).

1.6.2 Calibration

Inside the II, the x-ray signal is converted to electrons which are then amplified. A curved input phosphor plate converts the energy of the electrons into visible light, and then projects it onto a flat output phosphor. Due to the curved nature of the input plate, the II introduces pincushion distortion toward the edge of the image on the order of 10% that must be corrected to minimize 3D tracking errors (1, 105). Distortion can be corrected by acquiring calibration images with a calibration frame attached to the face of the II. Calibration frames contain uniformly spaced lead beads on a Plexiglass sheet or a perforated metal sheet. The distortion correction algorithm compares the spacing between the beads or holes of the calibration frame in the fluoroscope image with the true spacing and calculates a transformation matrix for correcting the images (106). Each x-ray image undergoes calibration using the distortion correction algorithm prior to joint motion

analysis. Positioning the anatomy of interest in the center of the II also helps minimize distortion.

In biplane studies, a 3D calibration object is needed to calibrate the imaging volume so that the relationship between the 3D coordinates of the bones and the projected 2D image coordinates can be determined. The calibration object is typically acrylic, either a cube or triangle, with beads implanted in known locations. Software using the direct linear transformation (DLT) method calculates the position of each bead to determine the configuration of the biplane system relative to the global reference coordinate system (1, 2). The DLT technique defines the linear transformation between the 3D object space and the 2D image planes by using a group of 11 coefficients to represent the internal parameters and orientation of the cameras (127). The DLT method was used to calibrate the volume of the biplane system built in this study.

1.6.3 Marker-based Tracking

In marker-based fluoroscopy, tantalum beads implanted in bones are used to track and calculate kinematics. A minimum of three beads per bone segment are required for 3D analysis (106). This is an invasive procedure that is limited to subjects who are undergoing a surgical procedure at the same time as implantation (107). To extract the marker coordinates from biplane x-ray images, four steps are required. First, the images are corrected with the distortion correction algorithm. Second, the 3D space is calibrated using the calibration object and required parameters. Third, the marker positions are tracked in the x-ray images. Fourth, the 3D coordinates of the markers are used to calculate the rigid body motions of each bone segment. In addition to being invasive,

some trials can be lost due to the beads becoming obstructed when aligned with implanted joint prostheses, screws or rods. A bead must be simultaneously visible in both fluoroscopy images in order to calculate the 3D bead position (109). Marker-based studies are typically used as the “gold standard” when evaluating the accuracy and validating model-based tracking methods and software. The current study used model-based tracking methods to avoid invasive marker-based techniques.

1.6.4 Model-based Tracking

Markerless or model-based fluoroscopy has been developed because of the invasiveness and limitations of implanting beads into living subjects. The model-based method determines bone positions and orientations by comparing a 3D bone model, obtained with CT or MR, to the acquired biplane fluoroscopic images. The 3D model is typically created from CT images by identifying and segmenting the anatomy of interest using various available software packages. Once 3D bone models are created, a local coordinate system (LCS) is assigned to each model so that the orientation and positions of the models can be determined within the calibrated space using standard rigid-body transformations.

The 3D bone model pose is defined by the six DOF position and orientation of the model’s LCS relative to the global coordinate system (GCS) (83). Two techniques to estimate the pose of the 3D model are currently used: feature-based or intensity-based. The feature-based methods rely on identifying features in the image, such as bony landmarks and contour information. The prosthesis or bone models are projected as a 2D silhouette over the images to determine the position and orientation (77). The bony

landmarks and contours assist in aligning the projection over the image for optimal placement of the model. This method has been effective for assessing *in vivo* kinematics of both prosthetic joints (77, 83, 89, 92, 93) and natural joints (110, 128). Due to the smooth, rounded corners of bones, feature detection in natural joints may be difficult using this technique. This method also requires manual identification of the landmarks on each frame of fluoroscopy images.

The intensity-based method is performed by comparing digitally reconstructed radiographs (DRRs) with the acquired x-ray images. DRRs are x-ray images created by computer simulation using virtual models of the fluoroscopy systems and subject anatomy. Using the calibration object data, the locations and orientations of the x-ray sources and high-speed cameras are modeled within a computer program so that a virtual configuration identical to the actual biplane fluoroscopy system is created (84, 111). The 3D bone models created from the CT images are placed within the virtual configuration so that a pair of DRRs can be generated by ray-tracing projections through the bone models (105). The DRRs change accordingly as the CT models are translated and rotated within the virtual space, resulting in simulated 2D images (DRRs) from the 3D geometry of the modeled bones. The similarity between the modeled DRRs and the acquired biplane x-ray images is calculated, and the positions of the bone models are optimized to find the positions which yield the highest similarity between the simulated DRRs and the acquired images (83, 107). An overview of the model-based method is presented in Figure 6.

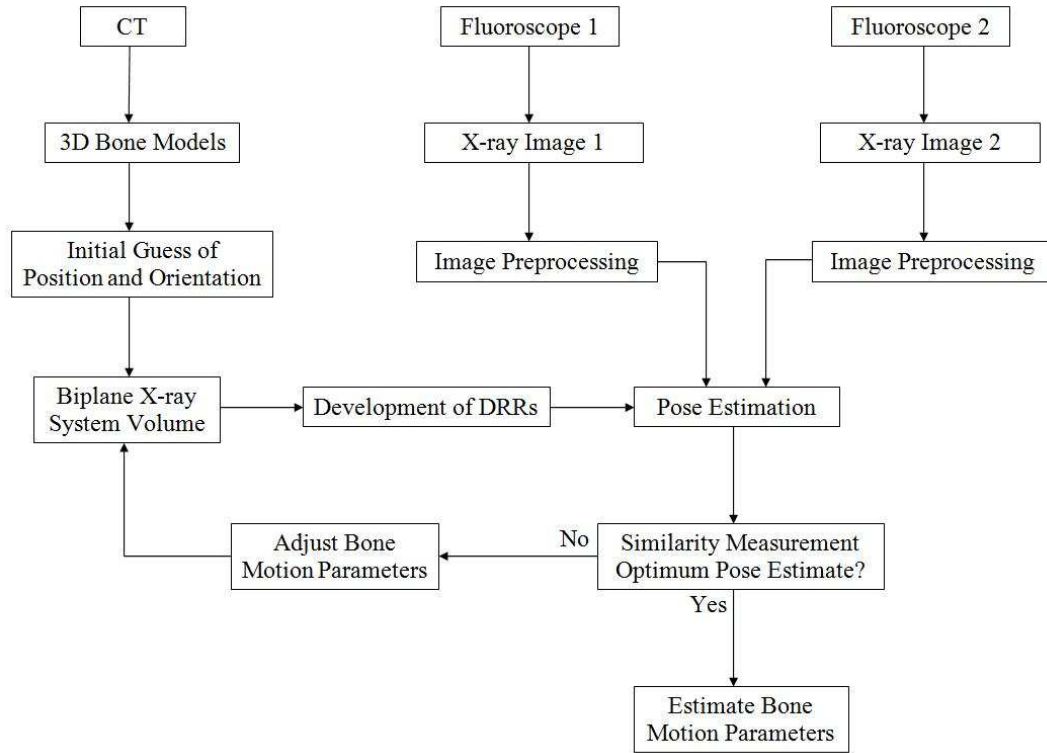


Figure 6: Flow chart of model-based tracking method (2).

Various similarity metrics and optimization algorithms have been proposed, including: Euclidean distance between contours extracted from the DRRs and measured x-ray images (77), root mean square distance between projection lines and model surface (92), similarity measures between the x-ray image and DRRs (128), downhill Simplex optimization (2), and optimization by simulated annealing (89). Once the bone model and biplane x-ray images are optimally aligned for each frame in the sequence, the joint position and orientation are obtained directly from the model using inverse kinematics (84). While intensity-based methods are computationally more expensive than feature-based methods, they have been used successfully to assess *in vivo* joint kinematics of the spine (129), shoulder (107), and knee (2, 112, 113).

1.6.5 Fluoroscopic System Validation

Fluoroscopic methods are expected to reliably quantify motion on the sub-millimeter scale. Currently, there are no commercially available or standard fluoroscopy systems or software specifically designed for motion analysis, causing research groups to build and validate their unique systems. Tashman has recommended that an independent validation be performed of each biplane fluoroscopy system specifically for the anatomical joints and activities that will be analyzed (130). Validating these systems typically requires evaluating how the hardware and software eliminates distortion inherent in fluoroscopy systems, and measuring the static and dynamic accuracy and precision. Numerous validation studies of biplane fluoroscopy system have been reported for marker-based (1, 106, 131-133) and model-based tracking (104, 107, 112, 113, 131, 134). In the current study, the system and tracking software used was validated using previously performed methods of implanting beads into a cadaver specimen (106, 107, 113, 131, 134). The system used a combination of open source software packages: image distortion correction using X-ray Reconstruction of Moving Morphology (XROMM) software (106), DLTdv5 marker-based tracking software (135), and Autoscooper model-based tracking software (131).

1.7 Foot and Ankle Fluoroscopy

Fluoroscopic analysis is expected to have numerous benefits for studying the foot and ankle joint complex. Conventional motion analysis methods often make assumptions of these segments due to the numerous small bones and several joints involved. The absence of external landmarks on the talus limits the ability of skin-mounted markers to

measure the AJC motion accurately (72). Understanding the biomechanics of the tarsal complex during gait is critical to the proper care of patients with a variety of orthopaedic impairments. The first fluoroscopy study involving the foot was performed by Green et al. in 1975 (136). Fluoroscopic images were captured on 16 mm film and bony motion was described as subjects moved their foot through its maximal ROM. Various single plane and biplane studies involving the foot and ankle have since been performed (72, 95-102, 117, 119-123, 137-144).

Wearing et al. used fluoroscopic methods to measure sagittal plane motion of the arch (95, 141), and properties of the heel fat pad during walking (142). Gefen et al. developed a clinical application for biomechanical analysis of the foot (137), and also determined the elastic properties of the plantar fascia during walking using fluoroscopy (139). Several other researchers have used fluoroscopy to analyze AJC kinematics (97, 99, 100, 102, 117, 122, 140). Komistek et al. developed the first 2D static kinematic model of the foot based on fluoroscopic images in 2000 (140). The study measured sagittal plane motion of ten ankles between maximum dorsiflexion and plantarflexion. De Asla et al. developed the first 3D static kinematic model of the hindfoot using fluoroscopy in 2006 (117). 3D bone models of the tibia, fibula, talus and calcaneus were created using MR images. The fluoroscopic images were used to align the 3D bone models into the correct orientation. Anatomical coordinate systems (ACSs) for each bone model were used to complete the kinematic analysis between the different orientations. These studies were all limited by their static nature, and by only analyzing certain poses, or specific points throughout the gait cycle. The overall goal of this project was to develop and validate a biplane fluoroscopic system and integrated software to assess

hindfoot kinematics. This study is the first that quantified the cross-scatter contamination in a biplane fluoroscopic system and its effects on the accuracy of marker-based tracking. This study completed the necessary validation of the biplane system by performing a cadaver foot study, determining the static and dynamic error of the system using both marker-based and model-based tracking algorithms. In addition, the study developed an *in vivo* 3D kinematic model of the talocrural and subtalar joints during the stance phase of gait. To achieve this, the following objectives and specific aims were defined:

1.8 Objectives

1. Develop a biplane fluoroscopy system for *in vivo* studies of hindfoot kinematics.
2. Validate the system and software for use of model-based tracking of the hindfoot.
3. Develop *in vivo* kinematic models of the hindfoot joints.

1.9 Specific Aims

1. Develop a hardware system for performing biplanar fluoroscopic analysis of *in vivo* hindfoot kinematics during the stance phase of gait.
2. Incorporate a software system to track the bones throughout the analyzed motion.
3. Perform imaging study quantifying cross-scatter contamination in biplane system.

4. Evaluate the static and dynamic error of the biplane system with a cadaver specimen using both marker-based and model-based tracking algorithms.
5. Develop *in vivo* 3D kinematic model of the talocrural and subtalar joints with fluoroscopic analysis.

2. DEVELOPMENT OF BIPLANE FLUOROSCOPY SYSTEM

2.1 Biplane Fluoroscopy System

A biplane system was constructed centered along a 7 m, non-obstructed walkway with an embedded 46.4 by 50.8 cm force plate (AMTI OR6-500 6-DOF, Watertown, MA) to allow for clinical gait assessment (Figure 7). The force plate is used to accurately determine heel strike and toe off, as well as collect the ground reaction forces (GRFs) at 3000 Hz. The force plate is connected to a Vicon Nexus system (Version 1.7, Vicon Motion Systems, Lake Forest, CA). Two x-ray sources (OEC 9000, GE, Fairfield, CT), and two images intensifiers (II's, 15" diam., Dunlee, Aurora, IL) are mounted to the walkway with a 60 degree angle between the sources. Prior to obtaining the second gantry, the single plane system, along with a phantom foot (XA241L, Phantom Lab Inc.) and rotary table (30010-S, Parker Daedal, Irwin, PA), were used to simulate biplane images at angles ranging between 45 and 90 degrees. The 60 degree angle allowed for the largest field of view with the least amount of forefoot bone overlap. The sources and II's were disarticulated C-arms that were mechanically and electronically installed in this configuration. All four components had brackets attached to their side, enabling the sources and II's to be placed on posts that are attached to steel plates on either side of the walkway. The posts have 6 height levels to lock in the system. The top level is used for a non-obstructed view of the calibration grid for image distortion correction. The system is then dropped down the lowest level for geometric calibration and to allow for the largest field of view during stance phase of gait. The source-to-detector and source-to-object-center distances are 112 cm and 76 cm, respectively for both source-intensifier pairs. During testing, the x-rays were generated using continuous exposure. High-speed, high

resolution (1024 x 1024) cameras (N4, IDT, Pasadena, CA) are attached to each II. Cameras have 52mm lenses (Nikon, Melville, NY). Images are captured at 200 fps and digitized directly to a controller PC via Motion Studio 64 (Version 2.10.05, IDT, Pasadena, CA).

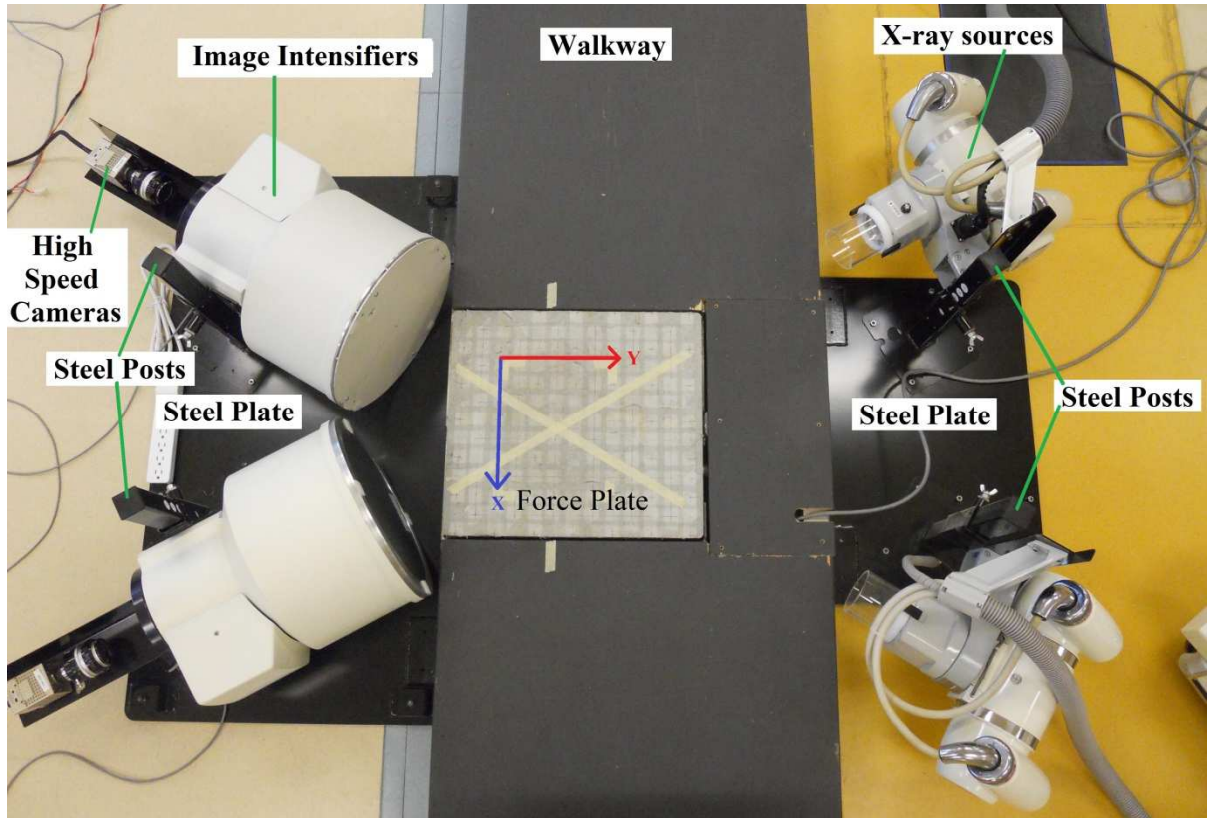


Figure 7: Custom-built biplane fluoroscopy system with x-ray sources attached to right-hand side of walkway and image intensifiers attached to left-hand side. The embedded force plate is placed where x-ray beams intersect. Global lab coordinate system shown with x-axis parallel to the walkway, y-axis across the walkway, and z-axis perpendicular to the walkway (z-axis not shown).

2.2 System Synchronization

The entire system was set up to record synchronously. When the fluoroscopy push-button switch was pressed, both x-ray tubes were turned on and a 5V TTL pulse,

generated by one of the fluoroscopy units, was sent to the trigger circuit. The circuit initiated synchronous recording of the images and while sending a pulse signal to the Vicon system as an external device analog signal. High acceleration impact testing was performed to ensure synchronous recording between the fluoroscopy system high speed cameras and the force plate.

2.3 Exposure of System

Exposure is the amount of ionization per mass of air due to x and gamma rays. It is a useful quantity because ionization is the process by which radiation detectors work and the initial event that can lead to biological damage (125). An in-beam chamber (RadCal 10x6-6, Monrovia, California) was placed in the middle of the radiation area of the biplane system and combined with an x-ray monitor (MDH Industries Model 1015, Monrovia, California) to measure the amount of radiation exposure (unit of roentgen or R) at various voltage and current levels (Table 1). The fluoroscopy units were turned on for two seconds, the approximate length of one gait trial, to record the measurements. As expected, the exposure increased with an increase in the voltage, due to the increased energy of photons produced.

Table 1: Exposure measurements of biplane system with fluoroscopy units turned on for 2 seconds.

kV	mA	R
60	5.0	0.115
70	5.0	0.157
80	4.5	0.190
90	3.5	0.199
100	2.5	0.191
110	2.2	0.214

Not all types of radiation cause the same biological damage per unit dose. The absorbed dose is the amount of energy imparted by radiation per mass (unit of rad). To modify the dose to measure the radiation in producing biological damage, the absorbed dose is multiplied by a radiation weighing factor to obtain the equivalent dose (unit of Sv) (125). An average testing procedure of 20 seconds (10 trials, 2 seconds each) has a total radiation exposure of 100 μ Sv, which is equivalent to the approximate solar radiation exposure received on a 12 hour flight from London to Tokyo (103). In the United States, the average person is exposed to 3000 μ Sv every year from natural background radiation (104).

2.4 Image Distortion Correction

Open source software, X-Ray Reconstruction of Moving Morphology (XROMM, Brown University, Providence, RI) was used for image intensifier distortion correction. Two calibration frames of 1.20 mm thick perforated steel with 3.18 mm diameter holes spaced 4.76 mm apart in a staggered pattern (part no. 9255T641, McMaster-Carr, Robinson, NJ) were cut to fit the face of the image intensifiers. The distortion correction algorithm in XROMM compares the spacing between the holes of the calibration frame in the fluoroscopic image with the known spacing of the frame and calculates a transformation matrix for correcting the images (106). Images of the calibration frames (Figure 8A) were corrected for geometric distortion using XROMM to create a transformation matrix. This matrix was then applied to all image sequences collected (Figure 8B and 8D).

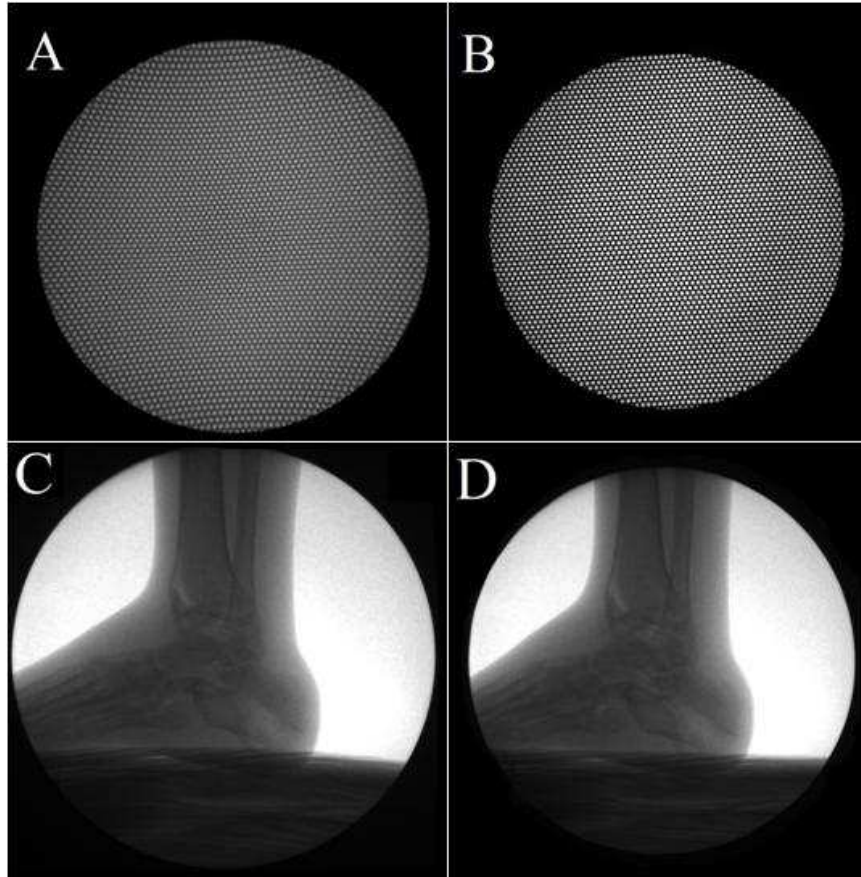


Figure 8: A) Raw, distorted calibration frame. B) Frame after distortion correction. C) Raw, distorted image of phantom foot. D) Foot after distortion correction algorithm applied.

2.5 Geometric Calibration

The direct linear transformation (DLT) technique was used to define the linear transformation between the 3D object space and the 2D image planes. The 11 DLT coefficients represent the internal parameters and orientations of the cameras (127). An acrylic calibration cube (Figure 9A), as described by Brainerd et al., with 64 precisely positioned steel spheres implanted as calibration points was manufactured and imaged with the biplane system (106). A coordinate measuring machine (CMM, Gage 2000, Brown & Sharpe, North Kingstown, RI) was used to measure the physical geometrical

characteristics of the cube to verify the positions of the beads within a linear accuracy of 0.005 mm. Points in the x-ray images of the cube (Figure 9B) were digitized and compared with the known points to determine the 11 DLT coefficients (135). The calibration cube origin was used as the global lab coordinate system origin, with the x-axis parallel to the walkway, y-axis across the walkway, and z-axis perpendicular to the walkway (x- and y-axis shown in Figure 7). The corner of the calibration cube was used as the global coordinate system due to the output of the model-based tracking results being reference to the cube origin. See Appendix A for complete instructions on biplane fluoroscopy.

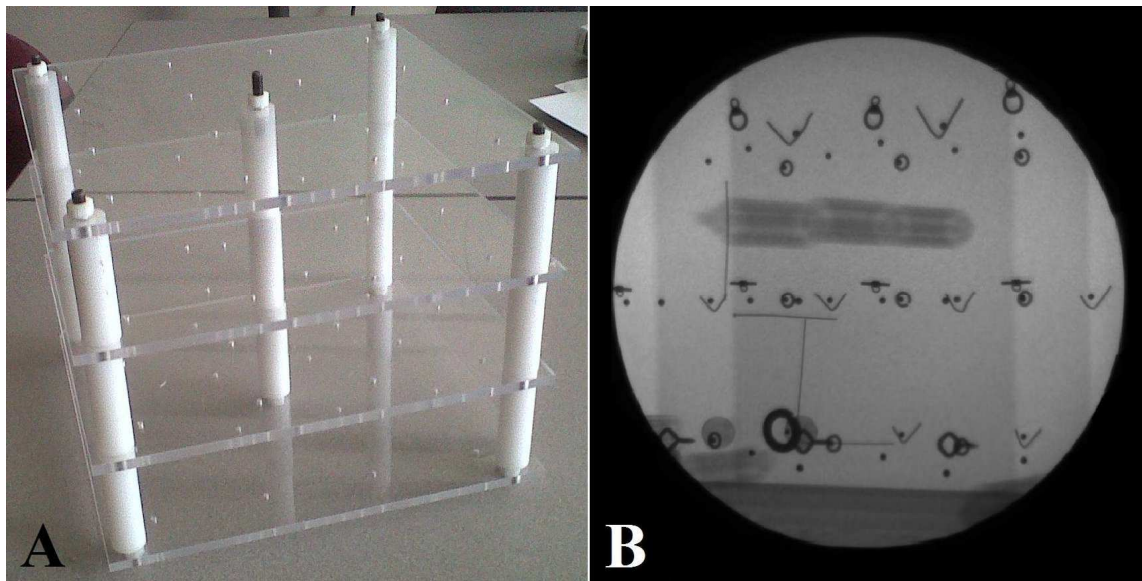


Figure 9: A) Image of 64-point calibration cube. B) Fluoroscopic image of calibration cube. Radiopaque markers were used to identify the beads in the fluoroscopic image.

3. QUANTIFYING CROSS-SCATTER CONTAMINATION IN BIPLANE FLUOROSCOPY MOTION ANALYSIS SYSTEMS

As in conventional x-ray imaging, the detected biplane fluoroscopy image is degraded by photons scattered from the primary beam. In biplane fluoroscopy, additional scattered photons are detected that originated from the second x-ray source, which is referred to as ‘cross-scatter.’ Cross-scatter is a potential source of degradation in biplane fluoroscopy motion analysis, as the two biplane images are typically acquired synchronously to enable accurate localization of the bone segments at each time point. The purpose of this aim was to quantify the magnitude and effects of cross scatter in fluoroscopic images acquired with a biplane x-ray imaging system over a range of object sizes, x-ray tube settings, and gantry angles. This study also quantified the effects of cross-scatter on the accuracy of marker-based tracking. Quantifying the effects of cross-scatter on motion tracking is important for determining whether scatter rejection methods should be developed for this specific application of high-speed motion tracking.

3.2 Methodology

The biplane system (Section 2.1), distortion correction algorithm (Section 2.4) and geometric calibration (Section 2.5) methods previously described were used in this study.

3.2.1 Phantoms and X-ray Settings

Four cylindrical water phantoms of height 12 inches and of diameter 4, 6, 8, and 10 inches were imaged. The 4-in cylinder represented the ankle, the 6-in cylinder the

knee, the 8-in cylinder the shoulder, and the 10-in cylinder simulated the spine. A one-inch-diameter Teflon sphere was suspended in the center of the phantoms for measuring contrast. Teflon and water were used to produce contrast similar to bone and soft tissue. For each phantom, images were acquired at a series of tube settings, with the voltage set at 60, 70, 80, 90, 100, and 110 kV, and the current set at 5.0, 5.0, 4.5, 3.5, 2.5, 2.2 mA. The current settings were varied in order to provide similar detected intensity within x-ray images of the foot across the different voltage levels.

Images containing primary, scatter, and cross-scatter signals (primary+scatter+cross_scatter) were collected by imaging with both sources on. In this work, ‘primary+scatter’ is the signal detected by one II from the beam that is focused on that II. ‘Cross-scatter’ is the signal detected by one II from the beam that is focused on the second II. Images were then acquired with one source turned off, such that one II collected images without cross scatter (primary+scatter), while the second II collected images of only cross-scatter and no primary signal. Fifty images were acquired (sampling frequency of 200 Hz) for each phantom, tube setting, and scatter condition.

3.2.2 Scatter Fraction and Contrast-to-Noise Ratio

Regions of interest (ROIs) of size 30 by 30 pixels were extracted from the water background (ROI1) and Teflon sphere (ROI2) in all the collected images. The background ROI was located at the center of the field of view. These ROIs were used to calculate the cross-scatter fraction (CSF) and the percent change in the contrast-to-noise ratio (CNR) due to cross scatter. The CSF was calculated as:

$$CSF = \frac{\overline{ROI1_{cross_scatter}}}{\overline{ROI1_{primary+scatter}}}. \quad (1)$$

The CNR was calculated for the Teflon bead in images acquired with and without cross scatter as:

$$CNR = \frac{|\overline{ROI1} - \overline{ROI2}|}{\sigma_{ROI1}} \quad (2)$$

The percent change in CNR due to cross-scatter was calculated as:

$$\%CNR = 100 * (1 - \frac{CNR_{primary+scatter+cross_scatter}}{CNR_{primary+scatter}}) \quad (3)$$

3.2.3 Effects of Gantry Angle on Cross-Scatter

The gantry angle is the angle between the central-ray of the two fluoroscopes. The system used in this study (Figure 7) has a fixed gantry angle of 60 degrees. Previous biplane fluoroscopy motion analysis studies have reported gantry angles ranging from 45 to 90 degrees (104, 107, 112). The amount of detected cross-scatter is expected to vary with gantry angle. The effects of gantry angle could not be experimentally quantified in this study, due to the fixed system geometry. Therefore, Monte Carlo simulations were performed to quantify cross-scatter fraction across a range of gantry angles. The biplane fluoroscopy system was modeled using the GEANT4 software (145). X-ray spectra were modeled at 60, 80, and 100 kV using the SPEC78 software (146). As in the experimental system, the source-to-detector distance was 112 cm, and source-to-object-center distance was 76 cm. The simulations modeled an ideal detector, which generated images of the primary and scattered signal. Simulations were performed with gantry angles of 60, 75, and 90 degrees for each of the four cylindrical water phantoms. The CSF was calculated for each gantry angle, phantom, and tube setting, using ROIs as in the experimental

study. To validate the simulation methods, the CSFs estimated from the simulations at 60 degrees were compared to the experimental measurements.

3.2.4 Effects of Cross-Scatter on Marker-based Tracking Accuracy

To determine the effects of cross-scatter contamination on the accuracy of marker-based tracking, a rectangular acrylic plate (50 mm long, 16 mm wide, 2.3 mm thick) with two 2-mm steel beads separated by 30-mm (± 0.03) was suspended in the center of the water phantoms. The water phantoms were then placed on the walkway at the intersection of the two beams. Static images were collected with both x-ray sources on to obtain primary+scatter+cross_scatter images. Images were collected with one source on and the other off to obtain image sequences containing the primary+scatter signal for one II. The on/off status of each source was reversed, to acquire primary+scatter signal for the second II. For dynamic testing, a pendulum moved the acrylic plate through the phantom. Due to the unrepeatable motion of the acrylic plate through the water, only primary+scatter+cross_scatter images were collected during dynamic trials. Static and dynamic images of the markers were collected with the x-ray sources set at 90 kV and 3.5 mA.

After the image distortion was corrected and the volume was calibrated, marker-based tracking was performed using software developed by Hedrick (135). In each fluoroscopic image, the bead positions were found by automatically tracking the center of the bead, using an extended Kalman prediction algorithm. The 3D positions of the beads were then determined from the biplane DLT data. For static tracking, the beads were tracked in 50 images of each phantom. The absolute tracking error for each image was

calculated as the measured distance between the beads minus the true 30-mm inter-bead distance. The mean absolute tracking error and standard deviation for each phantom were calculated. For dynamic tracking, the beads were tracked in 30 images for 5 trials of each phantom. The absolute error was calculated for each image, with the mean and standard deviation determined across all 5 trials. Statistically significant differences between the static tracking error with and without cross scatter were analyzed using a Student's *t*-test.

3.3 Results

Figure 10 shows an x-ray image of the primary+scatter image and the primary+scatter+cross_scatter image of the 4-in and 10-in water phantoms, demonstrating the negligible effect of cross-scatter for the 4-in phantom. Figure 10 also demonstrates the increased signal and reduced contrast due to cross scatter for the 10-in phantom.

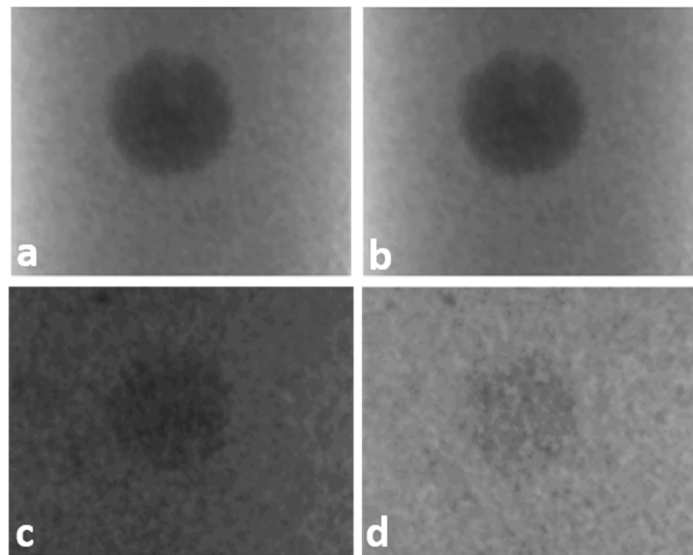


Figure 10: X-ray images of a) 4-in phantom primary+scatter image and b) 4-in phantom primary+scatter+cross_scatter image displayed at the same window/level settings. c) 10-

in phantom primary+scatter image and d) 10-in phantom primary+scatter+cross_scatter image displayed at the same window/level settings.

Figure 11 plots the CSF measured at a range of tube settings for all phantom diameters. The CSF increased with phantom diameter, ranging from 0.15 for the 4-in-phantom to 0.89 for the 10-in phantom, when averaged across kV. The CSF decreased with increasing kV. Cross-scatter reduced the CNR by 5% ($\pm 5\%$) for the 4-in phantom, 15% ($\pm 5\%$) for the 6-in phantom, 26% ($\pm 7\%$) for the 8-in phantom, and 36% ($\pm 9\%$) for the 10-in phantom, when averaged across kV. The percent change in CNR did not correlate with kV for any of the phantoms ($p > 0.1$).

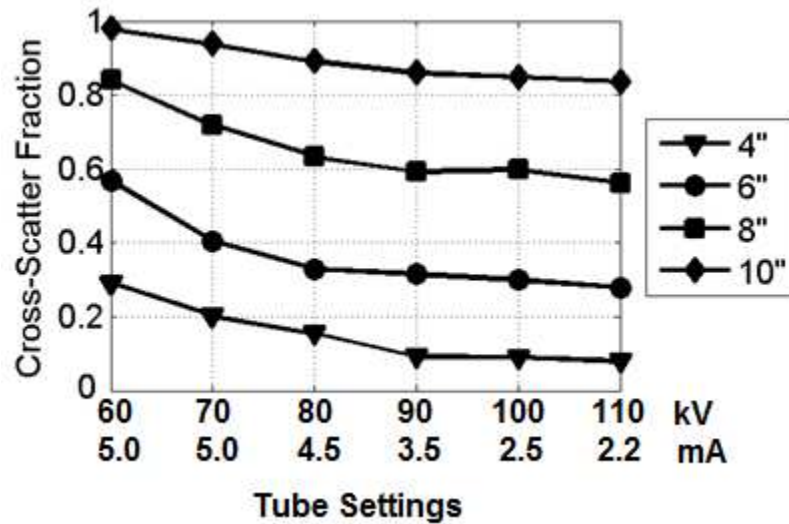


Figure 11: Measured cross-scatter fraction for all phantoms across a range of tube settings. Error bars, representing standard deviation, are smaller than the markers and thus are not visible.

Prior to quantifying the effects of gantry angle on cross-scatter, the simulation methods were validated against the experimental results at the 60 degree gantry angle. Figure 12 presents the results of the validation study. The experimental and simulation results demonstrated good agreement at 80 kV and 100 kV (error<10%). The 60 kV

simulations demonstrated larger discrepancies, with errors ranging from 13% to 60% compared to the experimental measurements. This discrepancy may be due to errors in modeling beam filtration. The purpose of the simulation study was to quantify the effect of gantry angle on cross-scatter magnitude, which can be investigated despite discrepancies in the 60 kV spectrum model.

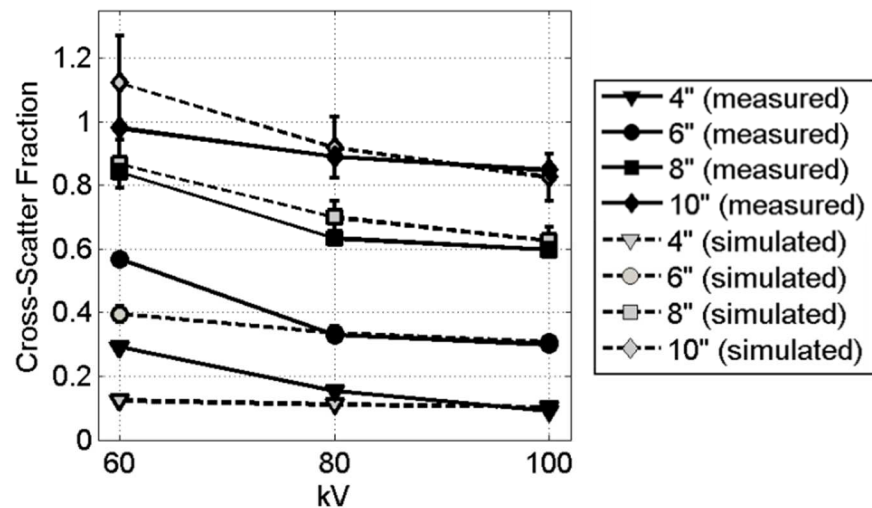


Figure 12: Comparison of CSF measured experimentally and estimated through simulations for a gantry angle of 60 degrees. Error bars represent one standard deviation.

Figure 13 plots the CSF at 60, 75, and 90-degree gantry angles, as estimated by the Monte Carlo simulations, for the 8-in and 10-in phantom at range of tube levels. The results demonstrate increased CSF with increasing gantry angle, with greater increases for the 10-in phantom and at lower tube settings. Gantry angle did not measurably affect the CSF for the 4-in and 6-in phantoms.

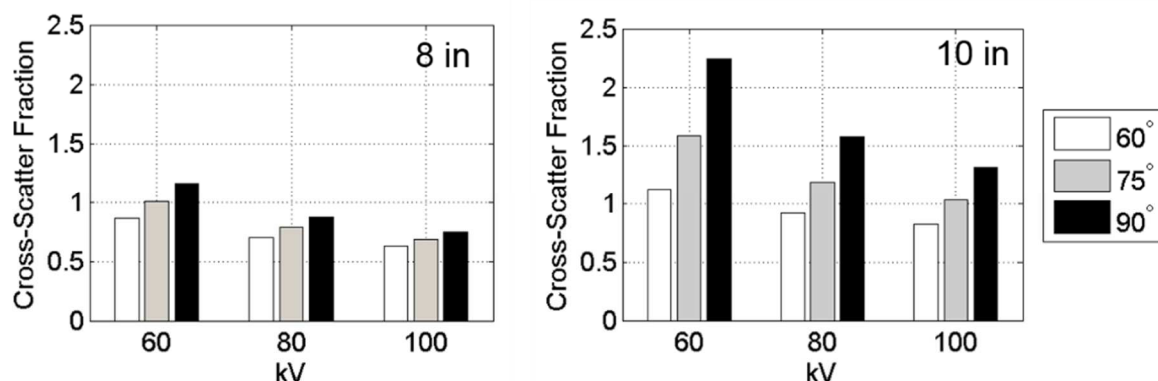


Figure 13: Cross-scatter fractions plotted for gantry angles of 60, 75, and 90-degrees for the 8-in and 10-in phantoms at a range of tube settings, as estimated through simulations. Gantry angle did not measurably affect the cross-scatter fractions for the 4-in and 6-in phantoms.

The absolute tracking error for the static marker trials is compared in Figure 14 for images with and without cross scatter. As seen in Figure 10, images acquired with cross scatter demonstrated significantly increased tracking error ($p < 0.01$) for the 6-in, 8-in, and 10-in phantoms. The error increased with phantom diameter.

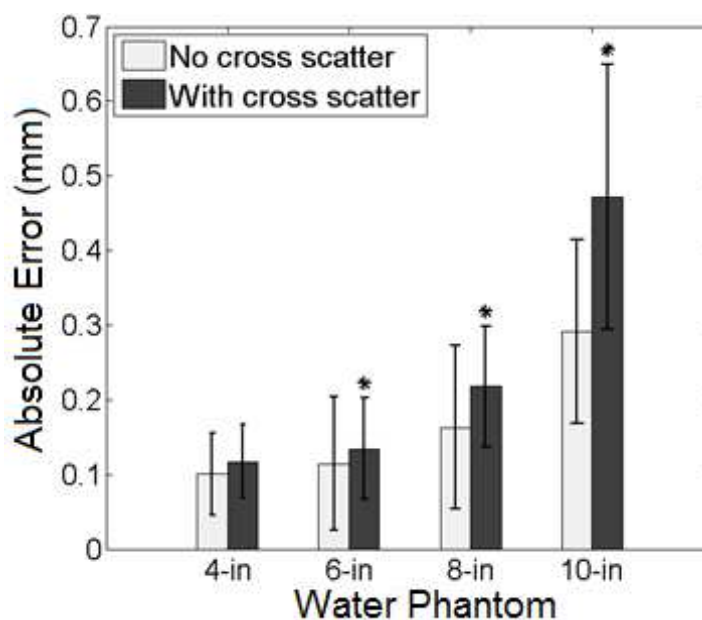


Figure 14: Static tracking error (in mm) between no cross scatter and with cross scatter. Note: * signifies statistical significance ($P < 0.01$)

Dynamic tracking was performed on images acquired with cross-scatter for all four water phantoms. Dynamic tracking without cross scatter was not possible, as synchronized acquisition is required to track a moving object. Table 2 displays the mean error (in mm) and standard deviation (SD) of the static and dynamic trials. The dynamic error was larger or had less precision than the static error for each phantom. As the phantom size increased, the error increased in both static and dynamic tracking.

Table 2: Static and dynamic tracking mean error and SD for images acquired with cross scatter.

Water Phantom	Static Error (mm)		Dynamic Error (mm)	
Object 1 (4")	0.12	(0.05)	0.15	(0.11)
Object 2 (6")	0.13	(0.07)	0.16	(0.10)
Object 3 (8")	0.22	(0.08)	0.23	(0.15)
Object 4 (10")	0.47	(0.18)	0.57	(0.49)

3.4 Discussion

Biplane fluoroscopy is currently being used for motion analysis of various joints. This study measured the magnitude and effects of cross-scatter for a biplane fluoroscopic motion analysis system across a range of object sizes and tube settings. Marker-based tracking was performed to analyze the effects of cross-scatter contamination on tracking accuracy. The sizes of the cylindrical water phantoms were selected to simulate joints studied using biplane fluoroscopy: the 4-in cylinder represented the ankle, the 6-in cylinder the knee, the 8-in cylinder the shoulder, and the 10-in cylinder simulated the spine.

The results demonstrated that the CSF increased with phantom size and decreased with kV. Cross scatter caused a greater reduction in CNR as the phantom size increased. For the smaller phantoms (4 in and 6 in), the CSF was unaffected by gantry angle. For the larger phantoms (8 in and 10 in), the CSF increased with gantry angle, despite the fact that photons are less likely to scatter at larger angles. One possible explanation of this result is that at larger gantry angles, scattered photons that travel towards the second detector are emitted closer to the phantom edge and have less attenuation within the phantom. The results of the simulation study suggest that a gantry angle of 60-degrees may be advantageous for larger objects, although these results should be verified experimentally with anthropomorphic phantoms.

Cross-scatter contamination did not significantly increase the tracking error in the 4-in phantom. Cross-scatter significantly increased the tracking error by 15%, 25% and 38% for the 6-in, 8-in, and 10 inch phantoms, respectively. The static tracking error with cross-scatter ranged from 0.12 mm (SD \pm 0.05) for the 4-in phantom to 0.47 mm (SD \pm 0.18) for the 10-in phantom. A previous study used XROMM software to track 12 markers embedded into two cylindrical polycarbonate posts and found a static tracking error of 0.12 mm (SD \pm 0.08), which is similar to the results in the current study (131). The dynamic tracking error with cross-scatter ranged from 0.15 mm (SD \pm 0.11) for the 4-in phantom to 0.57 mm (SD \pm 0.49) for the 10-in phantom. In previous studies, XROMM software dynamically tracked two steel markers of known separation embedded in a wand through a biplane fluoroscopy system with a mean absolute error of 0.037 mm (SD \pm 0.046) (106). Tashman and Anderst measured the tracking error of two beads implanted in acrylic to be 0.02 mm (SD \pm 0.10) using a different tracking

algorithm (1). In the current study, the highest tracking error of 0.57 mm ($SD \pm 0.49$) for the 10-in phantom with cross scatter is smaller than the estimated 2.7 to 14.9 mm error due to skin movement artifacts of skin-mounted markers (40).

The results suggest that marker-based tracking is possible on the sub-millimeter level for a range of phantom sizes, even in the presence of cross-scatter contamination. The reduction in CNR due to cross-scatter may affect the accuracy of model-based tracking techniques. Model-based tracking methods optimize the bone positions and orientations by comparing projections of a 3D bone model, generated from CT or MR data, to the fluoroscopic images (2, 131). The reduced CNR due to cross-scatter may decrease the accuracy of this 2D-3D registration algorithm. An area of future work is to quantify the effects of cross-scatter contamination on the accuracy of model-based tracking in biplane systems.

This study did not consider the effects of varying the distance between the object and the detector. As in conventional x-ray imaging, a larger air-gap is expected to reduce scatter. In motion tracking biplane fluoroscopy systems, the object is generally placed as close to the detectors as possible, in order to maximize the field of view. Therefore, larger air gaps are unlikely to be utilized for scatter rejection.

The biplane fluoroscopy system used in this study was designed for tracking the foot/ankle. Therefore, the walkway and force plate are in the beam path, as can be seen in Figure 7. These objects contribute to the cross-scatter, although the results from the 4-inch phantom suggest that this contribution is small. The significant increase in tracking error due to cross-scatter suggests that biplane fluoroscopy systems may benefit from the development of scatter rejection techniques for high-speed motion tracking applications.

Synchronous acquisition is currently required for motion estimation algorithms. Anti-scatter grids are expected to be effective at removing cross-scatter, due to the large scattering angles. Therefore, it may be beneficial to design grid mechanisms that enable accurate motion tracking at high frame rates.

3.5 Conclusion

The results demonstrated negligible cross-scatter effects for biplane fluoroscopy imaging of the 4-in phantom, suggesting negligible motion-tracking error due to cross scatter for distal extremities. This may change when a shoe or orthosis is present at the foot. Based on the 6 inch phantom results, with a shoe or orthoses added to the foot, the scatter and the tracking error may both increase. In human testing, when going from barefoot to shod analysis, the voltage may need to be increased to better penetrate the added material to reduce the scatter and produce the best tracking results. The cross-scatter fraction ranged from 0.4 to 0.9 for the 6 inch through 10 inch phantoms, with CNR decreasing by 15% to 36%. Cross scatter significantly increased the marker tracking error for the 6, 8, and 10-inch phantoms. These results suggest that the accuracy of motion analysis of larger anatomical regions, such as the shoulder or spine may be degraded due to cross scatter. Sub-millimeter tracking accuracy was attained in this study for all phantoms, despite increasing cross-scatter effects with phantom size. The results from this aim indicated which tube settings will produce images with the least amount of cross-scatter degradation and enable the best tracking results in future studies involving biplane fluoroscopic testing of the hindfoot.

4. **MARKER AND MODEL-BASED VALIDATION OF A BIPLANE FLUOROSCOPIC SYSTEM FOR HINDFOOT ANALYSIS**

The purpose of this aim was to quantify the accuracy and precision of a biplane fluoroscopy system for model-based (markerless) tracking of *in vivo* hindfoot motion. Due to the absence of an appropriate location for skin markers on the talus, optical motion analysis assumes the calcaneus and talus to be one segment. This aim used a cadaver foot specimen to evaluate motion tracking performance with a realistic field of view that included multiple bones and soft tissue.

4.2 Methods

The biplane system (Section 2.1), synchronization (Section 2.2), distortion correction algorithm (Section 2.4) and geometric calibration (Section 2.5) methods previously described were used in this study.

4.2.1 *Cadaver Specimen*

To provide a realistic simulation of the *in vivo* condition, a fresh frozen trans-tibial cadaver foot from a 34 year old male was obtained (Figure 15). Prior to bead implantation in the cadaver specimen, a skeletal model of the foot was used to determine the placement of the beads markers to avoid marker overlap and maximize spacing within the bones. Three 1.6-mm diameter steel beads were implanted into each of the three hindfoot bones (calcaneus, talus, and tibia) with minimal dissection of the surrounding soft tissues. A minimum of three beads per bone segment are required for 3D analysis (106), and all three beads must be simultaneously visible in both fluoroscopy images to

calculate the 3D positions. A 2-mm hole was drilled into the cortical bone so that the beads could be manually pressed into the hole until flush with the bone. The beads were then secured into place using cyanoacrylate adhesive. A 16-mm diameter steel rod was attached to the specimen using a bone plate attached to the proximal end of the tibia for manual manipulation through the capture volume.



Figure 15: Cadaver specimen with steel rod attached to tibia via bone plate

4.2.2 CT Scan

A CT scan of the cadaver foot was obtained consisting of 956, 0.625-mm thick transverse-plane slices (512 x 512 pixels) (LightSpeed VCT, GE Healthcare, Milwaukee, WI) to generate volumetric models of the calcaneus, talus, and tibia. An image processing algorithm was implemented in MATLAB (MathWorks, Natick, MA) to determine the

sub-pixel bead centroids, which represented the gold-standard bead locations. For model-based tracking, 3D bone models were generated by manual segmentation of the CT scan performed using 32-bit OsiriX software, version 3.8.1 (Pixmeo, Geneva, Switzerland). The radiopaque bead signatures were identified manually in the segmented bone images and replaced with the mean values from surrounding voxels to eliminate influences of the beads on the model-based tracking. This process is similar to previous methods used by You et al. for bead removal (2).

4.2.3 Static and Dynamic Trials

Static trials were obtained by both rotating and translating the foot through the capture volume. In the center of the volume, the foot was rotated through 11 foot progression angles ($\pm 25^\circ$, Figure 16A). It was then placed in 22 locations within the capture volume in a neutral position for translational measurements (Figure 16B). Ten dynamic trials were collected by manually simulating gait through the volume via the attached tibial rod. Accuracy of the dynamic trials was assessed by both marker-based and model-based tracking methods, therefore variation in motion between dynamic trials was acceptable. The force plate was used for event detection of heel strike and toe off. Quantifying the effects of cross-scatter contamination in the system determined that a higher voltage and lower current setting had the least amount of degradation in the images. Based on those results, all trials were collected with the x-ray tubes set at 100 kV and 2.0 mA.

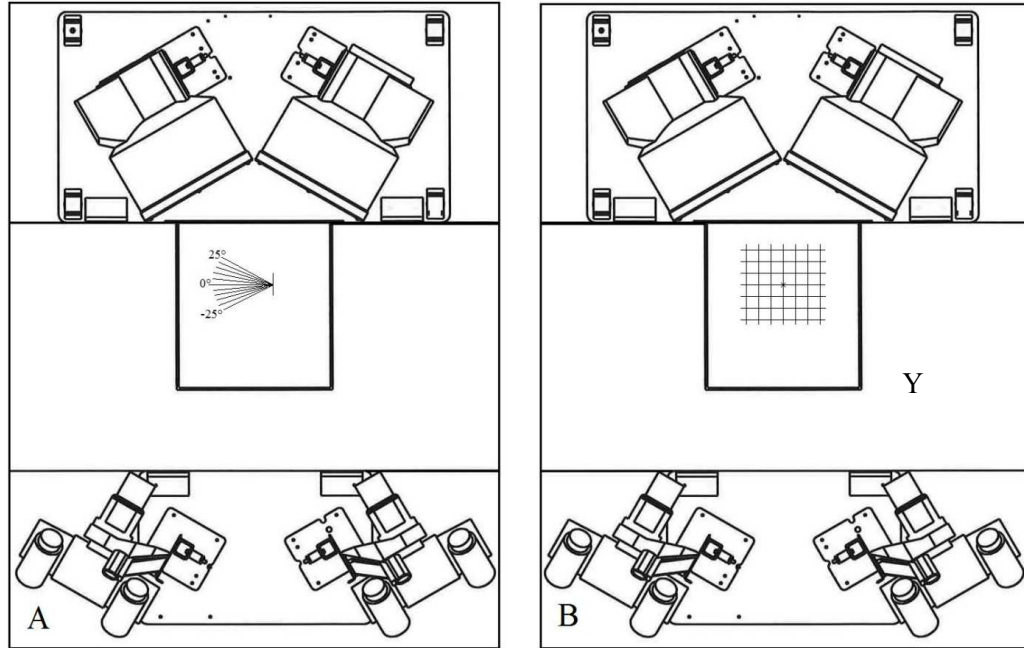


Figure 16: A) 11 static foot progression angles. B) Grid used for translational measurements.

4.2.4 Marker-based Tracking

After image distortion correction and geometry calibration, marker-based tracking was performed using standard DLT techniques (135). In each image sequence, the beads were first manually selected to start the automated tracking algorithm. If the algorithm failed to locate a bead while tracking the sequence, the bead was relocated manually, and then the automated tracking was resumed. The Euclidean distance between two beads within the same bone was found in both the CT and fluoroscopic images. The CT inter-bead distances were considered as the true distance. The marker-based tracking error was then calculated as the absolute value of the true distance minus the estimated distance. The error was calculated within each image, with the mean and standard deviation determined for the entire sequence, for all of the trials. It was assumed that the beads were rigidly fixed in the bone and that there was no motion of the beads relative to the

bone during the trial. The bead xyz coordinates were not filtered for tracking error calculations.

4.2.5 Model-based Tracking

The acquired static and dynamic fluoroscopic imaging sequences were also used to quantify the accuracy and precision of model-based tracking. Prior to model-based tracking, an automated image processing algorithm located the beads in all fluoroscopy images and replaced the bead pixels by selecting intensity values from the distribution of pixel values in the region surrounding each bead. Model-based tracking was performed using the previously validated software, Autoscooper (Brown University, Providence, RI) (131). The Autoscooper algorithm follows the description of auto-registration algorithms previously developed by You et al. (2) and Bey et al. (107) that use digitally reconstructed radiographs (DRRs) generated by ray-traced projections through a 3D bone model. The software uses a downhill simplex optimization algorithm to find the bone positions for which the DRRs best match the acquired x-ray images. In the current study, the calcaneus, tibia, and talus were tracked separately using 3D bones models, generated from the CT data. A trained user first manually aligned the bone models with the biplane x-ray images to obtain the best visual fit every two to five frames throughout the image sequence. Sobel edge detection and contrast enhancement filters were applied to the bone models and biplane image sequences to improve alignment. These parameters were selected by the user to provide the best visual match. The Autoscooper optimization algorithm was then performed on the manually aligned frames, with the Autoscooper software interpolating between the frames. Once the tracking was complete, the 6 degrees

of freedom (DOF) were output (x, y, z position, yaw, pitch, roll orientation). The rotation matrices were defined using the traditional dynamics definitions, with the Euler sequence XYZ designation. The differences between the manual and the automated method of model-based tracking were compared.

All bone DOF from Autoscooper were recorded in the lab coordinate system. To enable a direct comparison between the marker-based and model-based tracking results, a transformation matrix was used to determine the position of the beads in the bone models and expressing their 3D positions relative to the laboratory coordinate system. Agreement between the marker-based and model-based tracking results was quantified by bias in each xyz bead coordinate (the average difference in bead positions between the two methods, averaged across the three beads in each bone and across all trials) and precision (standard deviation of the difference in bead positions between the two methods, averaged across the three beads in each bone and across all trials). The root-mean-squared (RMS) error of the bead xyz coordinates estimated through model-based tracking relative to the marker-based bead positions across all trials was also calculated to assess the overall accuracy of the model-based tracking method. To assess the intra-observer user error associated with model-based tracking, the tibia was tracked repeatedly ten times in one dynamic trial.

4.3 Results

The marker-based tracking method resulted in an average of 0.1% error across the three bones in both the static and dynamic trials, with the CT-derived bead positions serving as the gold standard. The absolute error was lower in the static trials than the

dynamic trials for all three bones (Table 3). Each bone had 3 bead pair distances calculated, averaged across 100 frames in the static trials and 150-200 frames in the dynamic trials. The bone averages were then calculated across all trials for the given motion (11 rotations, 22 translations, 10 dynamic). Marker-based static tracking error results for all trials are in Appendix C.

Table 3: Marker-based absolute mean tracking error and standard deviation (SD) in mm.

	Calcaneus	Talus	Tibia	Overall
	mm (SD)	mm (SD)	mm (SD)	mm (SD)
Static: Rotation	0.12 (0.06)	0.16 (0.09)	0.15 (0.06)	0.15 (0.07)
Static: Translation	0.16 (0.04)	0.14 (0.05)	0.14 (0.04)	0.15 (0.04)
Dynamic	0.22 (0.12)	0.19 (0.15)	0.23 (0.18)	0.21 (0.15)

The model-based tracking bias for static trials was less than 0.35 mm across all three bones in both rotation and translation trials (Tables 4A and 4B). The rotational bias ranged from -0.28 mm to 0.34 mm (Table 4A), and the translational bias ranged from -0.25 mm to 0.25 mm (Table 4B). Rotational precision ranged from 0.04 mm to 0.15 mm (Table 4A), and the translation precision ranged from 0.04 mm to 0.13 mm (Table 4B). Across all static trials, the y-axis measurements were less precise than the x-axis and z-axis measurements. The static tracking precision values were similar between all three bones, with the tibia demonstrating slightly higher precision than the calcaneus and talus. Complete bias, precision and RMS error results for static trials are in Appendix D.

Model-based tracking bias for dynamic trials was less than 0.30 mm for all three bones, ranging from -0.30 mm to 0.05 mm (Table 4C). Model-based tracking precision for dynamic trials ranged from 0.37 mm to 1.19 mm, with the precision along the y-axis

lower than the x-axis and z-axis precision. Complete bias, precision and RMS error results for dynamic trials are in Appendix E.

Table 4: Model-based tracking accuracy for individual bones (bias and precision reported in mm and SD).

Table 4A. Static Rotation Trials

Axis	Bias			Precision		
	Calcaneus	Talus	Tibia	Calcaneus	Talus	Tibia
X	-0.20 (0.37)	0.19 (0.58)	0.04 (0.20)	0.06 (0.03)	0.09 (0.03)	0.04 (0.02)
Y	-0.02 (0.29)	-0.28 (0.71)	0.03 (0.25)	0.09 (0.04)	0.15 (0.07)	0.07 (0.03)
Z	-0.26 (0.29)	0.34 (0.77)	-0.08 (0.32)	0.06 (0.03)	0.08 (0.03)	0.05 (0.04)

Table 4B. Static Translation Trials

Axis	Bias			Precision		
	Calcaneus	Talus	Tibia	Calcaneus	Talus	Tibia
X	-0.03 (0.18)	-0.05 (0.38)	0.09 (0.11)	0.07 (0.06)	0.05 (0.03)	0.04 (0.03)
Y	-0.03 (0.44)	0.25 (0.72)	0.01 (0.26)	0.13 (0.13)	0.09 (0.04)	0.06 (0.03)
Z	-0.25 (0.23)	0.07 (0.50)	0.04 (0.28)	0.07 (0.04)	0.05 (0.02)	0.04 (0.02)

Table 4C. Dynamic Trials

Axis	Bias			Precision		
	Calcaneus	Talus	Tibia	Calcaneus	Talus	Tibia
X	0.05 (0.11)	-0.06 (0.16)	0.03 (0.13)	0.70 (0.22)	0.37 (0.06)	0.38 (0.08)
Y	-0.23 (0.21)	-0.05 (0.21)	-0.09 (0.23)	1.19 (0.33)	0.75 (0.13)	0.42 (0.07)
Z	-0.30 (0.18)	0.02 (0.29)	-0.22 (0.09)	0.69 (0.17)	0.40 (0.06)	0.39 (0.07)

The RMS error was lower in the static trials (Tables 5A and 5B) than the dynamic trials (Table 5C), with the smallest RMS error in the tibia across all trials. The overall RMS error between methods, calculated across all three bones and trials, was 0.56 mm in static rotation, 0.45 mm in static translation, and 0.59 mm in the dynamic trials. Similar to the precision measurements, the y-axis RMS error was higher than x-axis and z-axis error. Across all three bones and trials, the manual model-based tracking method had an

overall dynamic error of 0.64 mm, compared to the automated method of 0.59 mm (Figure 17).

Table 5: Model-based tracking accuracy for individual bones (RMS error reported in mm and SD).

Table 5A. Static Rotation Trials

Axis	RMS Error							
	Calcaneus		Talus		Tibia		Overall	
X	0.72	(0.44)	0.67	(0.32)	0.28	(0.17)	0.56	(0.31)
Y	0.87	(0.35)	0.84	(0.15)	0.27	(0.13)	0.66	(0.21)
Z	0.54	(0.19)	0.57	(0.27)	0.27	(0.21)	0.46	(0.22)
Overall	0.71	(0.33)	0.69	(0.25)	0.27	(0.17)	0.56	(0.25)

Table 5B. Static Translation Trials

Axis	RMS Error							
	Calcaneus		Talus		Tibia		Overall	
X	0.39	(0.24)	0.40	(0.24)	0.25	(0.16)	0.35	(0.21)
Y	0.83	(0.38)	0.79	(0.45)	0.31	(0.18)	0.64	(0.34)
Z	0.48	(0.20)	0.36	(0.25)	0.24	(0.13)	0.36	(0.19)
Overall	0.57	(0.27)	0.52	(0.31)	0.26	(0.16)	0.45	(0.25)

Table 5C. Dynamic Trials

Axis	RMS Error							
	Calcaneus		Talus		Tibia		Overall	
X	0.70	(0.13)	0.37	(0.05)	0.37	(0.06)	0.48	(0.08)
Y	1.11	(0.21)	0.73	(0.14)	0.47	(0.06)	0.77	(0.13)
Z	0.71	(0.14)	0.46	(0.09)	0.42	(0.05)	0.53	(0.09)
Overall	0.84	(0.16)	0.52	(0.09)	0.42	(0.06)	0.59	(0.10)

* all values in mm

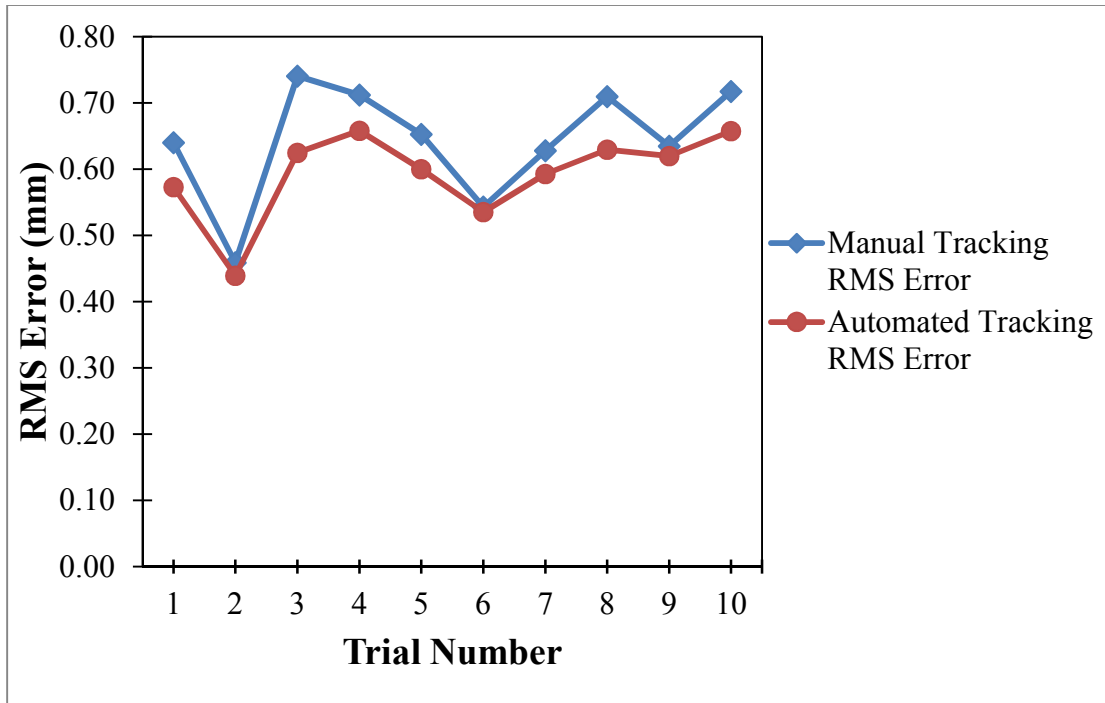


Figure 17: Manual versus automated model-based tracking across 10 dynamic trials.

The intra-observer user error of the model-based tracking was extremely low across all three measures (Figure 18). The bias ranged from -0.02 to 0.09 mm, the precision ranged from 0.51 to 0.63 mm, and the RMS error ranged from 0.52 to 0.60 mm across all ten repeated trials of tracking the tibia. Complete bias, precision and RMS error results for the user error are in Appendix F.

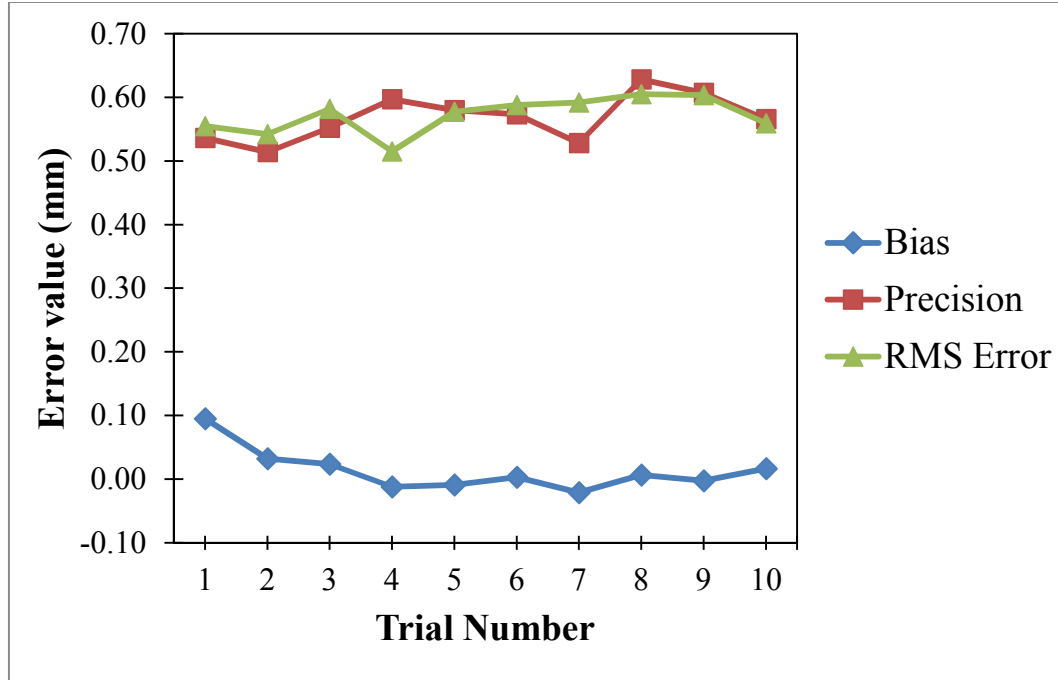


Figure 18: Intra-observer user error of model-based tracking ten times for one dynamic trial.

4.4 Discussion

This study evaluated the static and dynamic error of the biplane system using both marker-based and model-based algorithms. The results indicated that the system is accurate to within approximately 0.2 mm for marker-based tracking. For marker-based trials, the current system's average absolute error across all three bones was 0.15 mm (± 0.070), 0.15 mm (± 0.04), and 0.21 mm (± 0.15) for rotation, translation and dynamic trials, respectively. These numbers compare well with marker-based validation in other systems. Miranda et al. tracked 12 markers embedded into two cylindrical polycarbonate posts and found a static tracking error of 0.09° (± 0.08) and 0.12 mm (± 0.08) for rotation and translation, respectively (131). Iaquinto et al. used a wand with beads implanted to determine their systems error of 0.094 mm (± 0.081), 0.083° (± 0.068), and 0.126 mm (± 0.122) for translation, rotation and dynamic trails, respectively (132). Tashman and

Anderst found the dynamic bias (mean difference between measured and actual) of two beads implanted in acrylic to be -0.02 mm (1). Brainerd et al. dynamically tracked two steel markers embedded in a wand with a mean absolute error of 0.037 mm (± 0.046) (106). It is important to note that these previous marker-based studies validated their systems using phantom objects with implanted metal beads that do not duplicate complex bone geometries. The current aim used beads implanted in bones in a cadaver specimen with all the soft tissue intact. This allowed for a realistic validation of our system for the use of analyzing foot kinematics.

For model-based tracking, the results indicated that the system had a bias range of -0.30 mm to 0.34 mm, precision range of 0.04 mm to 1.19 mm, and an overall dynamic RMS average error of 0.59 mm. Across all three conditions (static rotation, static translation, and dynamic), the tibia had the lowest error, followed by the talus, then the calcaneus. Wang et al. had similar results across the bias and precision measures when tracking the same three bones (144). This is likely due to the long bone shape of the tibia is easier to track than the irregular shape of the talus and calcaneus. Model-based tracking has been previously validated for various anatomical regions. You et al. found the RMS error of canine knee kinematics averaged 0.5 mm in translation and 2.6° in rotation compared to the gold standard measurements performed with implanted bony markers (2). A cadaver study of the glenohumeral joint found a static bias ranged from -0.126 mm to 0.199 mm, static precision ranged from 0.06 mm to 0.13 mm, and had an overall dynamic RMS average error of 0.32 mm (107). Another cadaveric study of the patellofemoral joint had a bias range of -0.174 mm to 0.248 mm, precision range of 0.023 mm to 0.062 mm, and overall dynamic RMS average error of 0.24 mm (113). Anderst et

al. implanted beads in human subjects during ACL reconstruction to validate tibio-femoral tracking during running (112). They found the static bias ranged from -0.37 mm to 0.14 mm, static precision ranged from 0.03 mm to 0.08 mm, and had an overall dynamic RMS average error of 0.46 mm (112). In a different foot cadaver study, Wang et al. found a bias range of 0.31 mm to 0.50 mm and a precision range of 0.15 mm to 0.20 mm in their system (144).

The automated tracking method reduced the overall RMS error from 0.64 mm using just manual alignment, to 0.59 mm. Using the optimization algorithm reduces the error and also helps eliminate user bias. The results showed that the model-based tracking method had low intra-observer user error across all three measures (bias, precision, RMS error). Figure 18 also shows how the overall all RMS error, a combination of the precision and bias, is dominated by the precision factor.

It is important to validate each biplane fluoroscopy system for the anatomical joints to which they are intended investigate (130). This is due to the numerous factors that may influence the accuracy of the model-based method, including the shape of a particular bone, CT segmentation of the bone model, radiographic parameters (voltage and current), presence of surrounding soft tissues, overlap from surrounding bones, magnitude of joint motion, and the velocity of joint motion. In the current study, the overall dynamic RMS average error of 0.59 mm is smaller than the estimated 2.7 to 14.9 mm error at the foot due to generated by skin movement artifacts of skin-mounted markers (40).

In the model-based tracking, the precision values in the lab coordinate system y-axis were approximately two times higher than those in the x- and z-axis directions,

indicating less precision in the y-axis across all trials. This was expected due to model-based tracking methods being most imprecise when measuring movement perpendicular to the x-ray image plane, which is the y-axis direction in the current study (77, 89). Image intensifiers are 2D, and therefore lack depth perception and magnify objects farther away from the II. The lack of precision in the y-axis can easily be attributed to the relationship between the imaging planes and the primary direction of movement. This will affect the analysis if a patient walks with a severely internally or externally rotated foot, thus lining up the foot perpendicularly with one of the II's. While this error will impact the kinematic model along the mediolateral axis, it is still well below what is currently accepted for clinical gait assessment with SMA present.

One limitation of fluoroscopy in general is the amount of x-ray exposure associated with the CT scan and the fluoroscopy trials, which can limit the number of motion trials. The exposure can be reduced by using MR to obtain the 3D bone model. Also, the field of view is limited to the biplane x-ray system's 3D imaging volume. While this limitation prevents collection of biplane images during the entire gait cycle for some adult subjects, it does not restrict capture for pediatric participants.

In summary, the results presented herein indicate that the biplanar fluoroscopic hardware and tracking methods presented can be used to effectively track *in vivo* hindfoot bone motion within 0.59 mm. Model-based tracking was validated under the conditions that match the planned *in vivo* tracking trials. Biplane fluoroscopy is advantageous over traditional motion analysis methods due to the elimination of SMA and rigid-body assumptions. The non-obstructed, walkway-based biplane fluoroscopic system constructed was structured for clinical applications. The next steps will be validating

model-based tracking using a MR scan to create the 3D bone models to reduce the radiation exposure to patients and incorporating kinetic modeling by utilizing the force plate already embedded in the system. Future work will also include developing a kinematic model of the talocrural and subtalar joints to assess hindfoot joint motion under a variety of testing conditions in normal subjects and subjects with orthopaedic impairments, such as cerebral palsy or spina bifida, or foot deformities, such as equinovarus, pes planovalgus or club foot.

5. KINEMATIC MODEL FOR ASSESSMENT OF IN VIVO HINDFOOT MOTION DURING GAIT

To fully understand what is occurring during gait at the hindfoot, a kinematic analysis should be performed from heel strike to toe off. The purpose of this study was to develop the methodology to collect and analyze *in vivo* hindfoot kinematics using biplane fluoroscopy. The fluoroscopic images were corrected for image distortion before a model-based tracking method was used to determine bone position and orientation. Models were developed to determine talocrural and subtalar joint 3D kinematics. The method used avoided rigid-body assumptions and eliminated SMA by tracking the individual bones of the hindfoot using model-based tracking methods. The fluoroscopic method can also provide dynamic motion measurements within shoes that are otherwise difficult to achieve.

5.2 Methods

The biplane system (Section 2.1), synchronization (Section 2.2), distortion correction algorithm (Section 2.4) and geometric calibration (Section 2.5) methods previously described were used in this study.

5.2.1 ACS Definitions

After obtaining a CT scan, geometric bone models of the calcaneus, talus, and tibia were created from the images using OsiriX (Pixmeo, Geneva, Switzerland). Anatomical coordinate systems (ACSs) were defined for each bone (Figure 19) using Geomagic (Geomagic Wrap, Geomagic, Research Triangle Park, NC) according to the

International Society of Biomechanics (ISB) recommendations (147) and previously published methods (96, 99). The calcaneal origin was placed at the midpoint of the line that connected the most lateral point of the posterior facet and the most medial point of the middle facet. The superoinferior (SI) axis was defined as the line perpendicular to the facet line and the line tangent to the inferior surface of the calcaneus. The mediolateral (ML) axis was defined as the line perpendicular to the SI axis and the lateral wall of the calcaneus, passing through the origin. The anteroposterior (AP) axis was the cross product of the SI and ML axes. The talar origin was placed at the center of a sphere that encompassed the talus body. A line connecting the midpoint of the anteromedial and anterolateral edge and the midpoint of the posteromedial and posterolateral edge of the trochlea tali was defined. The ML axis was defined as the line perpendicular to this line, passing through the origin. The AP axis was defined as the line parallel to the midpoint line, passing through the origin. The SI was formed as a cross product of the AP and ML axes. The tibial origin was placed at the centroid of the tibial plafond. The SI axis was perpendicular to the tibial plafond, running parallel through the center of the shaft. The AP axis was perpendicular to the anterior edge of the tibia, passing through the origin. The ML axis was the cross product of the SI and AP axes. For each bone ACS, the SI axis was defined as the y-axis, the AP axis as the x-axis, and the ML axis as the z-axis. See Appendix B for detailed instructions on defining ACSs using Geomagic.

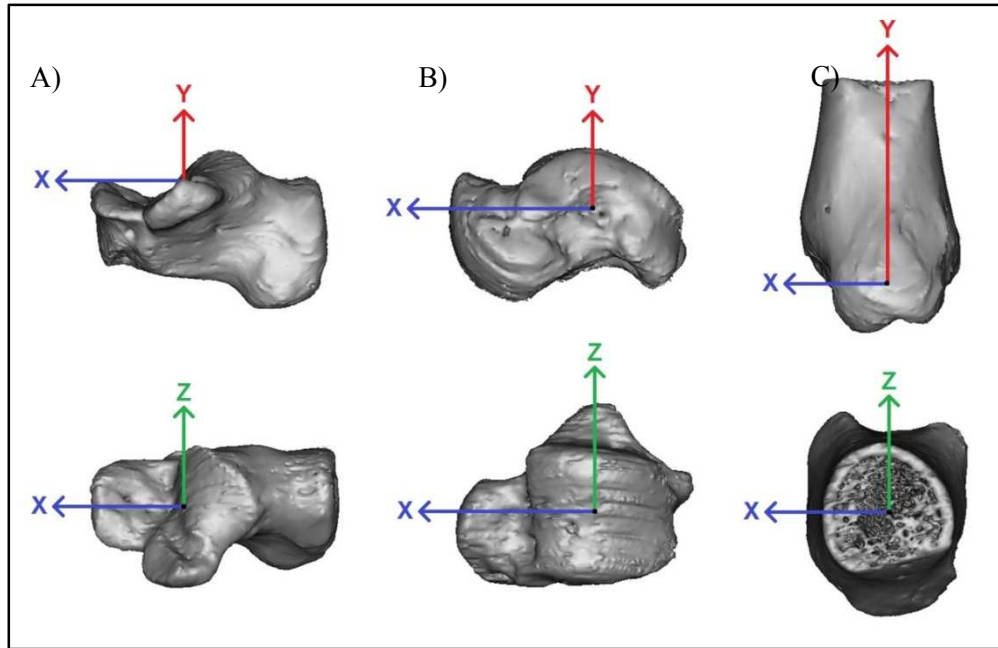


Figure 19: Anatomical coordinate system of the bones. Medial and superior views of the calcaneus (A), talus (B), and tibia (C).

5.2.2 Model Simulation

A fresh frozen trans-tibial cadaver foot from a 34 year old male was used for this study. A steel rod was attached to the specimen using a bone plate attached to the proximal end of the tibia for manual manipulation through the capture volume. A CT scan of the cadaver foot was obtained (LightSpeed VCT, GE Healthcare, Milwaukee, WI) to generate a volumetric model of the calcaneus, talus, and tibia. 3D bone models were generated by manual segmentation of the CT scan performed using OsiriX software. Static fluoroscopic images with the foot in a neutral position were used to quantify the angles of the joints at quiet standing and represent the neutral position of the kinematics. Ten dynamic trials were collected by manually simulating gait through the capture volume via the attached tibial rod. The force plate was used for event detection of heel strike and toe off.

5.2.3 *Model-based Tracking Method*

Model-based tracking was performed using the previously validated software, Autoscopers (Brown University, Providence, RI) (131). The Autoscopers algorithm follows the description of auto-registration algorithms previously developed by You et al. (2) and Bey et al. (107) that uses digitally reconstructed radiographs (DRRs) generated by ray-traced projections through a 3D bone model. The algorithm uses an optimization algorithm to find the bone positions for which the DRRs best match the acquired fluoroscopic images. In the current study, the calcaneus, tibia, and talus were tracked separately using 3D models segmented from the CT data. A trained user manually aligned the bone models with the biplane x-ray images to obtain the best visual fit for every two to five frames (depending on the amount of movement frame to frame) throughout the image sequence. Sobel edge detection and contrast enhancement filters were applied to the bone models and biplane image sequences to improve tracking. These parameters were selected by the user to provide the best visual match. The Autoscopers auto-tracking algorithm was performed for all frames with the Autoscopers software interpolating between the user-selected frames. Once the tracking was complete, the 6 degrees of freedom (DOF) were output (x, y, z position, yaw, pitch, roll orientation).

5.2.4 *Kinematic Models*

After obtaining the Autoscopers results and the ACSs, the data were analyzed using custom written programs (MATLAB, MathWorks, Natick, MA) using the joint coordinate system method described by Grood and Suntay (148). Talocrural joint motion was defined as the motion of the talus relative to the tibia. Subtalar joint motion was

defined as motion of the calcaneus relative to the talus. Using this convention, inversion (–, INV)/eversion (+, EV) occurred about the x-axis, abduction (–, ABD)/adduction (+, ADD) occurred about the y-axis, and dorsiflexion (–, DF)/plantarflexion (+, PF) occurred about the z-axis. All raw data were filtered at 20 Hz using a low-pass Butterworth filter. The kinematic results were reported relative to the neutral position and normalized to 100% of the stance phase of the gait cycle. The intra-observer variation of the methods defining the coordinate systems was determined by one observer performing the procedure three times. The average intra-observer differences were 0.40 mm and 0.78 degrees in translation and rotation, respectively.

5.3 Results

Normal walking was simulated using a cadaver specimen manually manipulated through the capture volume. Figure 20 shows kinematics of both the talocrural and subtalar joints during the stance phase of simulated gait.

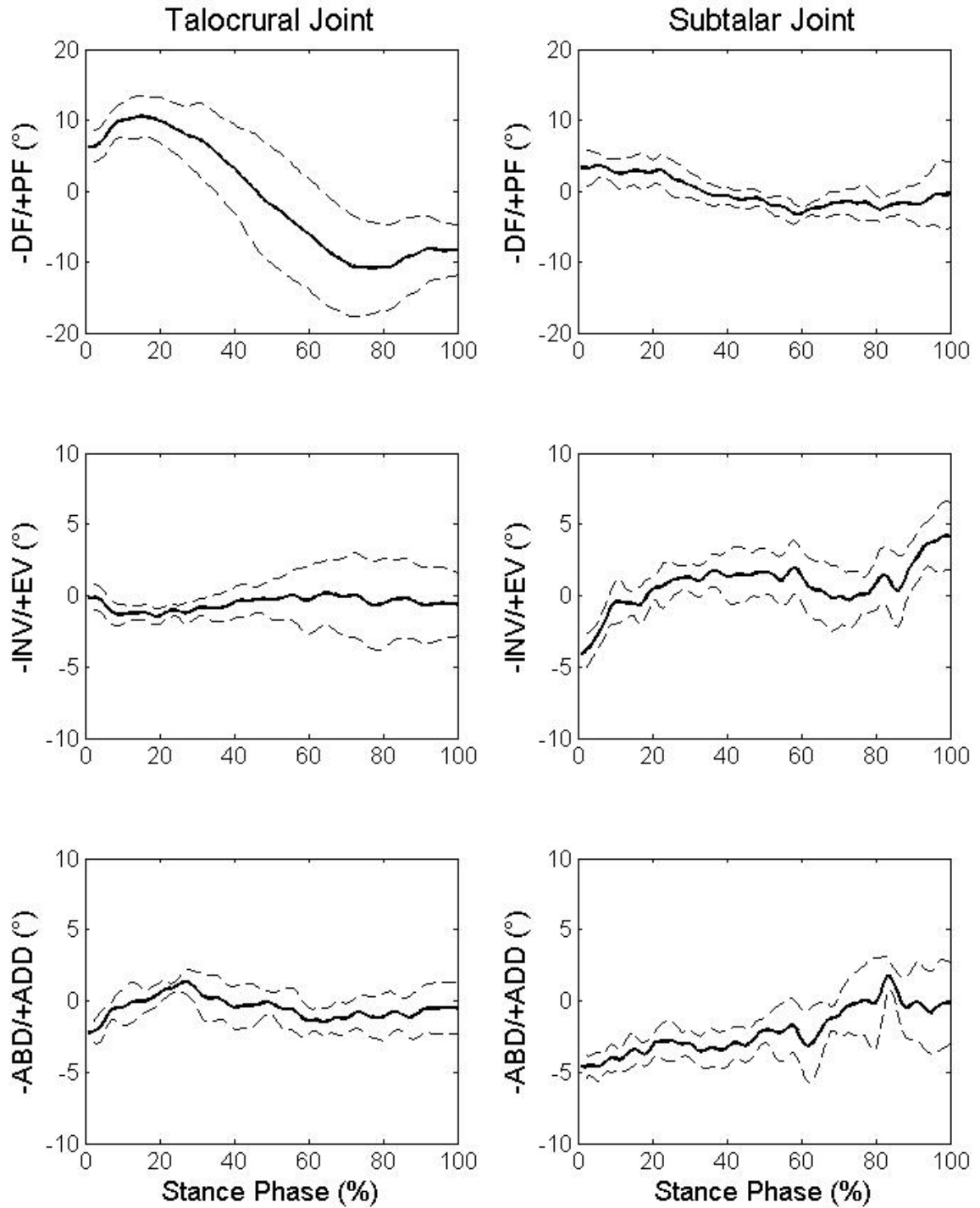


Figure 20: Talocrural and subtalar joint kinematics during stance phase. Solid lines represent mean of all 10 trials. Dashed lines represent mean ± 1 standard deviation. The morphology of the talocrural joint plantar/dorsiflexion curve was similar to results found in a 2D fluoroscopy study with human subjects (102).

For the talocrural joint, the primary motion was in the sagittal plane, with the DF/PF angles ranging from -12.47° to 10.73° , respectively (Table 6). For the subtalar joint, the motion was tri-axial; with the range of motion (ROM) nearly the same across all three planes (Table 6).

Table 6: Talocrural and subtalar joint maximum angles during stance phase ($^{\circ}$).

Joint	PF	DF	EV	INV	ABD	ADD
Talocrural	10.73	-12.47	1.79	-2.74	2.00	-2.96
Subtalar	5.35	-4.86	4.95	-3.99	2.32	-5.82

5.4 Discussion

The foot has two major functions during the gait cycle for normal ambulation: support and propulsion. The subtalar joint helps the foot level out gait, interfaces with uneven walking surfaces, acts as a shock absorber at heel strike, extends the extremes of motion of the ankle, and converts the foot to a rigid structure at toe off (17, 21). While gait analysis is a valuable tool to determine lower extremity kinematics for both research and clinical purposes, it has limitations when assessing foot kinematics. The absence of external landmarks on the talus restricts the ability of skin-mounted markers to measure the subtalar joint motion accurately (72). A unique biplane fluoroscopy system was built and rigorously validated for dynamic *in vivo* hindfoot analysis. Our system uses a combination of open source software packages: image distortion correction using X-ray Reconstruction of Moving Morphology (XROMM) software (106), DLTdv5 marker-based tracking software (135), and Autoscooper model-based tracking software (131) and was previously validated for hindfoot model-based tracking (Section 4.3).

The ROM at the talocrural joint showed the expected predominance of PF/DF motion (23.19°) compared to EV/INV (4.53°) and ABD/ADD (4.95°) (Figure 20, Table 6). The talocrural joint sagittal plane ROM is similar with previously presented studies, showing ROM values between 15.3 and 18.1 degrees (62, 64, 102). The subtalar joint is generally considered to demonstrate primarily EV/INV and ABD/ADD movements. Although this study did not confirm to this notion, the PF/DF ROM decreased dramatically (10.21°) and the EV/INV (8.94°) and ABD/ADD (8.14°) both increased, compared to the talocrural joint. This triaxial motion was also demonstrated in a bone pin study that found subtalar joint ROM to be 6.8 degrees, 9.8 degrees, and 7.5 degrees in the sagittal, frontal and transverse planes, respectively (64). The complex interlocking orientation of the three subtalar joint facets and the short sinus tarsi ligament provides a higher degree of constraint on its joint kinematics, compared to the talocrural joint and its inherent anatomy (64).

The current fluoroscopy talocrural and subtalar joint models are promising and offer a viable, noninvasive, method suitable for quantifying hindfoot kinematics in the bare and shod foot. The use of fluoroscopy overcomes the errors associated with optical motion analysis, such as SMA error and rigid-body assumptions. SMA produce the most significant source of error in gait (3, 11), with a study involving the foot and ankle showing the artifact between skin markers and bones varied from 2.7 to 14.9 mm (40). A single rigid segment is a gross assumption of the foot anatomy and function that may violate the rigid-body assumption in other foot models. Violation of the rigid-body assumption may lead to overestimated inter-segmental motion, unreported intra-segmental motion, or attributing motion to one joint when in fact it occurs at another

(46). Although bone pin studies allow for more direct analyze of hindfoot kinematics during walking, they are limited due to their invasive nature, possible pain and discomfort for the subjects, influences on the natural gait pattern, and have a risk of infection at the insertion site (33, 62).

This aim developed the methodology to collect and analyze *in vivo* hindfoot kinematics using biplane fluoroscopy. The next step will be applying the joint models to human testing and comparing the joint kinematics to previous bone pin and fluoroscopy studies. There are limitations of biplane fluoroscopy. Currently, it is limited to a small field of view, has extensive image data processing, and exposes the subjects to radiation. An average testing procedure of 20 seconds (10 trials, 2 seconds each) has a total radiation exposure of 100 μ Sv from the fluoroscopy units, plus 0.07 mSv of radiation from the CT scan, Future work should involve validating the use of a MR scan instead of relying on CT for creating the 3D models. This will greatly reduce the radiation exposure to patients and allow for pediatric testing. In addition to the kinematic model presented here, a kinetic model of the joints will be added in a future study, utilizing the force plate already embedded in the system. Future studies comparing barefoot verses shod or other braces/orthoses will be performed to describe foot movement within footwear.

6. CONCLUSION

Biplane fluoroscopy is used for dynamic, *in vivo* three-dimensional motion analysis of various joints of the body. The overall goal of this project was to develop and validate a biplane fluoroscopic system and integrated software to assess hindfoot kinematics. An aim quantified the cross-scatter contamination in a biplane fluoroscopic system and its effects on the accuracy of marker-based tracking. A cadaver foot specimen was used to determine the static and dynamic error of the biplane fluoroscopic system using both marker-based and model-based tracking algorithms. Lastly, *in vivo* 3D kinematic models of the talocrural and subtalar joints were developed during the stance phase of gait.

6.1 Summary of Findings

Based on the results of this dissertation, all specific aims in Section 1.9 were completed. A hardware system was developed (Section 2.1) with two gantries connected to a walkway to allow for biplane fluoroscopic analysis. The system collected data synchronously via a trigger circuit (Section 2.2). A suite of software programs were integrated into the system to analyze motion. First, the distortion introduced from the image intensifiers was corrected in all the images (Section 2.4). Second, a calibration cube allowed for the direct linear transformation method to define the linear transformation between the 3D object space and the 2D image planes, thus calibrating the 3D space of the capture volume (Section 2.5). Third, a model-based tracking algorithm was used to track the bones in the captured image sequences (Section 2.8).

The effect of cross-scatter contamination in the biplane system was quantified using water phantoms of varying diameters (Section 3.3). The results showed an increase in the cross-scatter fraction and average change in CNR with increase in phantom size. The cross-scatter also significantly increased the static tracking error in the three larger phantoms. Despite the cross-scatter degradation, the system still demonstrated that sub-millimeter marker-based tracking was possible for a range of phantom sizes. This aim demonstrated that a higher voltage and a lower current tube setting results in less cross-scatter degradation of the images and produce better tracking results, which will be important when selecting tube settings during human trials. It also indicated that the presence of a shoe or orthosis may increase the scatter and tracking error at the foot, thus needing the voltage to be increased.

The static and dynamic error of the biplane system was determined by performing a cadaver study (Section 4.3). Both marker-based and model-based tracking algorithms were validated for our system. The marker-based tracking method was precise for the three bones in both static and dynamic trials, with an average of 0.1% error across all trials. The overall dynamic absolute mean tracking error of the system was 0.21 mm. There was good agreement between the results from model-based tracking method with the marker-based tracking method, with the largest error being 0.59 mm. The model-based tracking bias for static trials was less than 0.35 mm, while dynamic trials were less than 0.30 mm for all three bones. Static precision ranged from 0.04 mm to 0.15 mm and dynamic ranged from 0.37 mm to 1.19 mm. The overall RMS error between methods averaged 0.56 mm in static rotation, 0.45 mm in static translation, and 0.59 mm in the dynamic trials.

Using the biplane system and anatomical coordinate systems for each bone, kinematic models of the talocrural and subtalar joints were developed following the joint coordinate system method (Section 5) (148). The models were simulated using the cadaver study. The ROM at the talocrural joint showed the expected predominance of PF/DF motion (23.19°) compared to EV/INV (4.53°) and ABD/ADD (4.95°). The results showed correlations of the gait patterns with previously published studies (62, 64, 102). The subtalar joint is generally considered to demonstrate primarily EV/INV and ABD/ADD movements. Although the results did not conform to this notion, the PF/DF ROM decreased (10.21°) and the EV/INV (8.94°) and ABD/ADD (8.14°) both increased, compared to the talocrural joint.

6.2 Limitations and Future Work

This study validates a biplane fluoroscopic system for analyzing 3D hindfoot kinematics *in vivo* during the stance phase of gait. This noninvasive process allows for evaluation of the subtalar joint that was previously unattainable with conventional motion analysis systems. Understanding the biomechanics of the foot during gait is critical to the proper care of patients with a variety of orthopaedic impairments or foot deformities, such as cerebral palsy, spina bifida, club foot, or pes planovalgus. Future work will use kinematic models of the talocrural and subtalar joints to assess hindfoot joint motion under a variety of testing conditions in normal subjects and subjects with pathological gait and foot deformities. Biplane fluoroscopy enables motion analysis of the shod foot, for which optical tracking methods are limited. Future studies will be performed using the system to analyze kinematics while wearing shoes, orthoses and various braces.

A current limiting factor of the system is the need for a CT scan to make the 3D models. To enable use of the system for pediatric clinical applications, the use of a MRI scan to generate the bone models needs to be validated to lower the radiation exposure. The issue with using a MRI scan is that the images produced have different intensity levels and lower spatial resolution. The effects of this on model-based tracking are unknown and need to be understood. The use of a MRI scan may require a transformation and additional image processing for the 3D models to be compatible with the model-based tracking technique. Once the use of MRI is validated, the system will be ready for clinical testing. Knowing how the kinematics of the hindfoot are altered by orthoses, shoe modifications or post-operatively may lead to better non-operative interventions and improved surgical techniques for patients with pathological gait. The system is already equipped with an embedded force plate, thus incorporating a kinetic model may advance the current analysis. The kinetic model would require defining the joint location, ground reaction force magnitude and location, segment masses, mass moments of inertia, and mass location. Previous work has found that the body segment parameters of the talus and calcaneus play an incidental role in the talocrural and subtalar kinetics (149). Due to these findings, a quasi-static kinetic model at selected points throughout stance phase may be more beneficial than performing a full kinetic analysis. The current force plate also limits the accuracy of a hindfoot kinetic model past foot flat during stance phase, with forces then traveling through more joints than just the subtalar and talocrural joints. Future work using F-Scan plantar pressure inserts (Tekscan, Inc, South Boston, MA) during fluoroscopic analysis would enable dynamic pressure, force and timing information of the foot during gait. A pilot fluoroscopic image of the sensor within a shoe

(Figure 21) demonstrates how radiolucent the sensor is due to its extremely thin design. The effects on the accuracy of tracking the bones with the sensor present should be verified in future work.



Figure 21: Pilot fluoroscopic image of foot with F-Scan plantar pressure. Markers present in image would not be used in a biplane fluoroscopic study.

To improve the current system, larger image intensifiers would increase the field of view and allow for full stance phase evaluation, with less trial loss due to missing the radiation area. Another way to reduce trial loss and radiation exposure is to implement a prediction algorithm using the Vicon system to determine whether a subject will step into the capture volume, thus turning on the fluoroscopy units. The scatter study found a

significant increase in tracking error due to cross-scatter, suggesting that biplane fluoroscopy systems may benefit from the development of scatter rejection techniques for high-speed motion tracking applications. Anti-scatter grids are expected to be effective at removing cross-scatter, due to the large scattering angles. It may be beneficial to design grid mechanisms that enable accurate motion tracking at high frame rates. Another area of future work is to quantify the effects of cross-scatter contamination on the accuracy of model-based tracking and the effects of shod and orthoses present at the foot. Lastly, a drawback of the current system is the time consuming process of manually tracking each bone individually in Autoscooper. A fully automated, multi-bone tracking algorithm would greatly reduce the processing time, allowing for faster analyses and quicker turnaround time in getting patients results.

BIBLIOGRAPHY

1. Tashman S, Anderst W. In-vivo measurement of dynamic joint motion using high speed biplane radiography and CT: application to canine ACL deficiency. *J Biomech Eng.* 2003;125(2):238-45.
2. You BM, Siy P, Anderst W, Tashman S. In vivo measurement of 3-D skeletal kinematics from sequences of biplane radiographs: Application to knee kinematics. *Medical Imaging, IEEE Transactions on.* 2001;20(6):514-25.
3. Cappozzo A, Catani F, Leardini A, Benedetti M, Della Croce U. Position and orientation in space of bones during movement: experimental artefacts. *Clin Biomech.* 1996 3;11(2):90-100.
4. Carson MC, Harrington ME, Thompson N, O'Connor JJ, Theologis TN. Kinematic analysis of a multi-segment foot model for research and clinical applications: a repeatability analysis. *J Biomech.* 2001 10;34(10):1299-307.
5. Kidder SM, Abuzzahab FS, Jr., Harris GF, Johnson JE. A system for the analysis of foot and ankle kinematics during gait. *Rehabilitation Engineering, IEEE Transactions on.* 1996;4(1):25-32.
6. Apkarian J, Naumann S, Cairns B. A three-dimensional kinematic and dynamic model of the lower limb. *J Biomech.* 1989;22(2):143-55.
7. Kadaba MP, Ramakrishnan HK, Wootten ME. Measurement of lower extremity kinematics during level walking. *Journal of Orthopaedic Research.* 1990;8(3):383-92.
8. Cappozzo A, Leo T, Pedotti A. A general computing method for the analysis of human locomotion. *J Biomech.* 1975 9;8(5):307-20.
9. Davis RB, Jameson EG, Davids JR, Christopher LM, Rogozinski BM, Anderson JP. The design, development, and initial evaluation of a multisegment foot model for routine clinical gait analysis. In: Harris GF, Smith P, Marks RM, editors. *Foot and Ankle Motion Analysis: Clinical Treatment and Technology.* Boca Raton, FL: CRC Press; 2008. p. 425-44.
10. Harris GF. Analysis of Ankle and Subtalar Motion during Human Locomotion. In: Stiehl JB, editor. *Inman's Joints of the Ankle.* Second Edition ed. Baltimore, MD: Williams & Wilkins; 1991. p. 75-84.
11. Leardini A, Chiari L, Croce UD, Cappozzo A. Human movement analysis using stereophotogrammetry: Part 3. Soft tissue artifact assessment and compensation. *Gait Posture.* 2005 2;21(2):212-25.

12. Ioppolo J, Börlin N, Bragdon C, Li M, Price R, Wood D, et al. Validation of a low-dose hybrid RSA and fluoroscopy technique: Determination of accuracy, bias and precision. *J Biomech.* 2007;40(3):686-92.
13. France DL. Human and nonhuman bone identification: a color atlas. CRC Press; 2008.
14. Pick TP, Howden R, editors. *Gray's Anatomy*. Unabridged ed. Philadelphia, PA: Running Press; 1974.
15. Sangeorzan BJ. Subtalar Joint: Morphology and Functional Anatomy. In: Stiehl JB, editor. *Inman's Joints of the Ankle*. Second Edition ed. Baltimore, MD: Williams & Wilkins; 1991. p. 31-8.
16. Hicks JH. The mechanics of the foot: I. The joints. *Journal of Anatomy.* 1953;87(345):357.
17. Wright DG, Desai SM, Henderson WH. Action of the subtalar and ankle-joint complex during the stance phase of walking. *Journal of Bone and Joint Surgery.* 1964;46(2):361-464.
18. Close JR, Inman VT, Poor PM, Todd FN. The Function of the Subtalar Joint. *Clinical Orthopaedics and Related Research.* 1967;50:159-79.
19. Inman VT. *The joints of the ankle*. Baltimore, MD: Williams & Wilkins; 1976.
20. Root ML, Weed JH, Sgarlato TE, Bluth DR. Axis of motion of the subtalar joint. *J Am Podiatry Assoc.* 1966;56(4):149-55.
21. Sangeorzan BJ. Biomechanics of the Subtalar Joint. In: Stiehl JB, editor. *Inman's Joints of the Ankle*. Second Edition ed. Baltimore, MD: Williams & Wilkins; 1991. p. 65-73.
22. Rodgers MM. Dynamic Biomechanics of the Normal Foot and Ankle During Walking and Running. *Physical Therapy.* 1988 December 01;68(12):1822-30.
23. Tiberio D. Pathomechanics of structural foot deformities. *Physical Therapy.* 1988;68:1840-9.
24. Siegler S, Chen J, Schneck CD. The three-dimensional kinematics and flexibility characteristics of the human ankle and subtalar joints - Part I: kinematics. *Journal of Biomechanical Engineering.* 1988;110(364):373.
25. Sharkey NA, Hamel AJ. A dynamic cadaver model of the stance phase of gait: performance characteristics and kinetic validation. *Clin Biomech.* 1998 9;13(6):420-33.

26. Parenteau CS, Viano DC, Petit PY. Biomechanical Properties of Human Cadaveric Ankle-Subtalar Joints in Quasi-Static Loading. *Journal of Biomechanical Engineering*. 1998;120(1):105-11.
27. Leardini A, Stagni R, O'Connor JJ. Mobility of the subtalar joint in the intact ankle complex. *J Biomech*. 2001 6;34(6):805-9.
28. Hamel AJ, Sharkey NA, Buczek FL, Michelson J. Relative motions of the tibia, talus, and calcaneus during the stance phase of gait: a cadaver study. *Gait Posture*. 2004 10;20(2):147-53.
29. Nester C, Jones RK, Liu A, Howard D, Lundberg A, Arndt A, et al. Foot kinematics during walking measured using bone and surface mounted markers. *J Biomech*. 2007;40(15):3412-23.
30. Nester CJ, Liu AM, Ward E, Howard D, Cocheba J, Derrick T, et al. In vitro study of foot kinematics using a dynamic walking cadaver model. *J Biomech*. 2007;40(9):1927-37.
31. Reinschmidt C, van den Bogert A, Murphy N, Lundberg A, Nigg B. Tibiocalcaneal motion during running, measured with external and bone markers. *Clin Biomech*. 1997 1;12(1):8-16.
32. Benoit DL, Ramsey DK, Lamontagne M, Xu L, Wretenberg P, Renström P. Effect of skin movement artifact on knee kinematics during gait and cutting motions measured in vivo. *Gait Posture*. 2006 10;24(2):152-64.
33. Fuller J, Liu LJ, Murphy MC, Mann RW. A comparison of lower-extremity skeletal kinematics measured using skin- and pin-mounted markers. *Human Movement Science*. 1997 4;16(2-3):219-42.
34. Shultz R, Kedgley AE, Jenkyn TR. Quantifying skin motion artifact error of the hindfoot and forefoot marker clusters with the optical tracking of a multi-segment foot model using single-plane fluoroscopy. *Gait Posture*. 2011 5;34(1):44-8.
35. Reinschmidt C, van den Bogert AJ, Nigg BM, Lundberg A, Murphy N. Effect of skin movement on the analysis of skeletal knee joint motion during running. *J Biomech*. 1997 7;30(7):729-32.
36. Reinschmidt C, van den Bogert AJ, Lundberg A, Nigg BM, Murphy N, Stacoff A, et al. Tibiofemoral and tibiocalcaneal motion during walking: external vs. skeletal markers. *Gait Posture*. 1997 10;6(2):98-109.
37. Holden JP, Orsini JA, Siegel KL, Kepple TM, Gerber LH, Stanhope SJ. Surface movement errors in shank kinematics and knee kinetics during gait. *Gait Posture*. 1997 6;5(3):217-27.

38. Akbarshahi M, Schache AG, Fernandez JW, Baker R, Banks S, Pandy MG. Non-invasive assessment of soft-tissue artifact and its effect on knee joint kinematics during functional activity. *J Biomech.* 2010 5/7;43(7):1292-301.
39. Tranberg R, Karlsson D. The relative skin movement of the foot: a 2-D roentgen photogrammetry study. *Clin Biomech.* 1998 1;13(1):71-6.
40. Maslen BA, Ackland TR. Radiographic study of skin displacement errors in the foot and ankle during standing. *Clin Biomech.* 1994 9;9(5):291-6.
41. Della Croce U, Leardini A, Chiari L, Cappozzo A. Human movement analysis using stereophotogrammetry: Part 4: assessment of anatomical landmark misplacement and its effects on joint kinematics. *Gait Posture.* 2005 2;21(2):226-37.
42. Henley J, Richards J, Hudson D, Church C, Coleman S, Kersetter L, et al. Reliability of a clinically practical multisegment foot marker set/model. In: Harris GF, Smith P, Marks RM, editors. *Foot and ankle motion analysis: clinical treatment and technology.* Boca Raton, FL: CRC Press; 2008. p. 445-64.
43. Kadaba MP, Ramakrishnan HK, Wootten ME, Gainey J, Gorton G, Cochran GVB. Repeatability of kinematic, kinetic, and electromyographic data in normal adult gait. *Journal of Orthopaedic Research.* 1989;7(6):849-60.
44. Leardini A, Benedetti MG, Catani F, Simoncini L, Giannini S. An anatomically based protocol for the description of foot segment kinematics during gait. *Clin Biomech.* 1999 10;14(8):528-36.
45. Long JT, Eastwood DC, Graf AR, Smith PA, Harris GF. Repeatability and sources of variability in multi-center assessment of segmental foot kinematics in normal adults. *Gait Posture.* 2010 1;31(1):32-6.
46. Nester CJ, Liu AM, Ward E, Howard D, Cocheba J, Derrick T. Error in the description of foot kinematics due to violation of rigid body assumptions. *J Biomech.* 2010 3/3;43(4):666-72.
47. Okita N, Meyers SA, Challis JH, Sharkey NA. An objective evaluation of a segmented foot model. *Gait Posture.* 2009 7;30(1):27-34.
48. Hunt AE, M. Smith R, Torode M, Keenan A. Inter-segment foot motion and ground reaction forces over the stance phase of walking. *Clin Biomech.* 2001 8;16(7):592-600.
49. Legault-Moore D, Chester VL, de Vries D. Multisegment foot kinematics during walking in younger and older adults. *Journal of Clinical Medicine Research.* 2012;4(4):259-66.

50. Jenkyn TR, Nicol AC. A multi-segment kinematic model of the foot with a novel definition of forefoot motion for use in clinical gait analysis during walking. *Journal of Biomechanics*. 2007;40(14):3271-8.
51. Leardini A, Benedetti MG, Berti L, Bettinelli D, Nativio R, Giannini S. Rear-foot, mid-foot and fore-foot motion during the stance phase of gait. *Gait Posture*. 2007 3;25(3):453-62.
52. MacWilliams BA, Cowley M, Nicholson DE. Foot kinematics and kinetics during adolescent gait. *Gait and Posture*. 2003;17:214-24.
53. Hwang SJ, Choi HS, Kim YH. Motion analysis based on a multi-segment foot model in normal walking. *Annual International Engineering in Medicine and Biology Society Conference of the IEEE*; ; 2004.
54. Rouhani H, Favre J, Crevoisier X, Aminian K. Measurement of multi-segment foot joint angles during gait using a wearable system. *Journal of Biomechanical Engineering*. 2012;134:061106-1,061106-8.
55. Kaufman KR, Kitaoka HP, Hansen DK, Morrow DA, Kotajarvi BR. A Multisegment, 3D Kinematic Model of the Foot and Ankle. In: Harris GF, Smith PA, Marks RM, editors. *Foot and ankle motion analysis: clinical treatment and technology*. Boca Raton, FL: CRC Press; 2008. p. 465-70.
56. Öunpuu S, Davis RB, DeLuca PA. Joint kinetics: methods, interpretation and treatment decision-making in children with cerebral palsy and myelomeningocele. *Gait Posture*. 1996 1;4(1):62-78.
57. Janisse DJ, Janisse E. Shoe Modification and the Use of Orthoses in the Treatment of Foot and Ankle Pathology. *Journal of the American Academy of Orthopaedic Surgeons*. 2008 March 01;16(3):152-8.
58. Hutchins S, Bowker P, Geary N, Richards J. The biomechanics and clinical efficacy of footwear adapted with rocker profiles - Evidence in the literature. *The Foot*. 2009 9;19(3):165-70.
59. Long JT, Sirota N, Klein JP, Wertsch JJ, Janisse D, Harris GF. Biomechanics of the double rocker sole shoe: gait kinematics and kinetics. *Annual International Engineering in Medicine and Biology Society Conference of the IEEE*; ; 2004.
60. Brown D, Wertsch JJ, Harris GF, Klein J, Janisse D. Effect of rocker soles on plantar pressures. *Arch Phys Med Rehabil*. 2004 1;85(1):81-6.
61. Arnold JB, Bishop C. Quantifying foot kinematics inside athletic footwear: a review. *Footwear Science*. 2013 03/01; 2015/02;5(1):55-62.

62. Arndt A, Westblan P, Winson I, Hashimoto T, Lundberg A. Ankle and Subtalar Kinematics Measured with Intracortical Pins During the Stance Phase of Walking. *Foot and Ankle International*. 2004;25(5):357-64.
63. Arndt A, Wolf P, Liu A, Nester C, Stacoff A, Jones R, et al. Intrinsic foot kinematics measured in vivo during the stance phase of slow running. *J Biomech*. 2007;40(12):2672-8.
64. Lundgren P, Nester C, Liu A, Arndt A, Jones R, Stacoff A, et al. Invasive in vivo measurement of rear-, mid- and forefoot motion during walking. *Gait Posture*. 2008 7;28(1):93-100.
65. Arnold AS, Salinas S, Asakawa DJ, Delp SL. Accuracy of muscle moment arms estimated from MRI-based musculoskeletal models of the lower extremity. *Computer Aided Surgery*. 2000;5(2):108-19.
66. Siegler S, Udupa JK, Ringleb SI, Imhauser CW, Hirsch BE, Odhner D, et al. Mechanics of the ankle and subtalar joints revealed through a 3D quasi-static stress MRI technique. *J Biomech*. 2005 3;38(3):567-78.
67. Ringleb SI, Udupa JK, Siegler S, Imhauser CW, Hirsch BE, Liu J, et al. The effect of ankle ligament damage and surgical reconstructions on the mechanics of the ankle and subtalar joints revealed by three-dimensional stress MRI. *Journal of Orthopaedic Research*. 2005;23(4):743-9.
68. Li G, DeFrate LE, Park SE, Gill TJ, Rubash HE. In Vivo Articular Cartilage Contact Kinematics of the Knee: An Investigation Using Dual-Orthogonal Fluoroscopy and Magnetic Resonance Image-Based Computer Models. *The American Journal of Sports Medicine*. 2005 January 01;33(1):102-7.
69. Sheehan FT, Seisler AR, Siegel KL. Exploring the Frontiers of In Vivo Multibody Ankle Dynamics Using Fast-Phase Contrast Magnetic Resonance Imaging. In: Harris GF, Smith PA, Marks RM, editors. *Foot and Ankle Motion Analysis: Clinical Treatment and Technology*. Boca Raton, FL: CRC Press; 2008. p. 557-71.
70. Beimers L, Maria Tuijthof GJ, Blankevoort L, Jonges R, Maas M, van Dijk CN. In-vivo range of motion of the subtalar joint using computed tomography. *J Biomech*. 2008;41(7):1390-7.
71. Sheehan FT. The instantaneous helical axis of the subtalar and talocrural joints: a non-invasive in vivo dynamic study. *Journal of Foot and Ankle Research*. 2010;3(13):13.
72. Yamaguchi S, Tanaka Y, Kosugi S, Takaura Y, Sasho T, Banks SA. In vivo kinematics of two-component total ankle arthroplasty during non-weightbearing and weightbearing dorsiflexion/plantarflexion. *J Biomech*. 2011;44:995-1000.

73. Fassbind MJ, Rohr ES, Hu Y, Haynor DR, Siegler S, Sangeorzan BJ, et al. Evaluating Foot Kinematics Using Magnetic Resonance Imaging: From Maximum Plantar Flexion, Inversion, and Internal Rotation to Maximum Dorsiflexion, Eversion, and External Rotation. *Journal of Biomechanical Engineering*. 2011 November 3;133(10):104502-.
74. Gutekunst DJ, Liu L, Tao Ju T, Prior FW, Sinacore DR. Reliability of clinically relevant 3D foot bone angles from quantitative computed tomography. *Journal of Foot and Ankle Research*. September 2013;6(38).
75. AAPM Task Group 23. The measurement, reporting and management of radiation dose in CT. College Park, MD: American Association of Physicists in Medicine; 2008.
76. Biswas D, Bible JE, Bohan M, Simpson AK, Whang PG, Grauer JN. Radiation exposure from musculoskeletal computerized tomographic scans. *Journal of Bone and Joint Surgery*. 2009;91:1882-9.
77. Banks SA, Hodge WA. Accurate measurement of three-dimensional knee replacement kinematics using single-plane fluoroscopy. *Biomedical Engineering, IEEE Transactions on*. 1996;43(6):638-49.
78. Kedgley AE, Birmingham T, Jenkyn TR. Comparative accuracy of radiostereometric and optical tracking systems. *J Biomech*. 2009 6/19;42(9):1350-4.
79. Kaptein BL, Valstar ER, Stoel BC, Rozing PM, Reiber JHC. A new model-based RSA method validation using CAD models and models from reversed engineering. *Journal of Biomechanics*. 2003;36:873-82.
80. Kaptein BL, Valstar ER, Stoel BC, Reiber HC, Nelissen RG. Clinical validation of model-based RSA for a total knee prosthesis. *Clinical Orthopaedics & Related Research*. 2007;464:205-9.
81. Yuan X, Ryd L, Tanner KE, Lidgren L. Roentgen single-plane photogrammetric analysis (RSPA): A new approach to the study of musculoskeletal movement. *J Bone Joint Surg Br*. 2002 August 1;84-B(6):908-14.
82. Short A, Gill HS, Marks B, Waite JC, Kellett CF, Price AJ, et al. A novel method for in vivo knee prosthesis wear measurement. *J Biomech*. 2005 2;38(2):315-22.
83. Bingham JT, Li G. An optimized image matching method for determining in-vivo TKA kinematics with a dual-orthogonal fluoroscopic imaging system. *J Biomech E*. 2006;128(4):588-95.
84. Ackland DC, Keynejad F, Pandy MG. Future trends in the use of x-ray fluoroscopy for the measurement and modeling of joint motion. *Proc IMechE*. 2011;225:1-13.

85. Bauman JM, Chang Y. High-speed X-ray video demonstrates significant skin movement errors with standard optical kinematics during rat locomotion. *J Neurosci Methods*. 2010 1/30;186(1):18-24.
86. Matsuki KO, Matsuki K, Mu S, Sasho T, Nakagawa K, Ochiai N, et al. In vivo 3D kinematics of normal forearms: Analysis of dynamic forearm rotation. *Clin Biomech*. 2010 12;25(10):979-83.
87. Rash GS, Belliappa PP, Wachowiak MP, Somia NN, Gupta A. A demonstration of the validity of a 3-D video motion analysis method for measuring finger flexion and extension. *J Biomech*. 1999 12;32(12):1337-41.
88. Auerbach JD, Wills BP, McIntosh TC, Balderston RA. Evaluation of Spinal Kinematics Following Lumbar Total Disc Replacement and Circumferential Fusion Using In Vivo Fluoroscopy. *Spine*. 2007;32(5):527-36.
89. Mahfouz MR, Hoff WA, Komistek RD, Dennis DA. A robust method for registration of three-dimensional knee implant models to two-dimensional fluoroscopy images. *Medical Imaging, IEEE Transactions on*. 2003;22(12):1561-74.
90. Hoff WA, Komistek RD, Dennis DA, Gabriel SM, Walker SA. Three-dimensional determination of femoral-tibial contact positions under in vivo conditions using fluoroscopy. *Clin Biomech*. 1998 10;13(7):455-72.
91. Fregly BJ, Rahman HA, Banks SA. Theoretical accuracy of model-based shape matching for measuring natural knee kinematics with single-plane fluoroscopy. *Journal of Biomechanical Engineering*. 2005;127(4):692-9.
92. Zuffi S, Leardini A, Catani F, Fantozzi S, Cappello A. A model-based method for the reconstruction of total knee replacement kinematics. *Medical Imaging, IEEE Transactions on*. 1999;18(10):981-91.
93. Yamazaki T, Watanabe T, Nakajima Y, Sugamoto K, Tomita T, Yoshikawa H, et al. Improvement of depth position in 2-D/3-D registration of knee implants using single-plane fluoroscopy. *Medical Imaging, IEEE Transactions on*. 2004;23(5):602-12.
94. Zihlmann MS, Gerber H, Stacoff A, Burckhardt K, Székely G, Stüssi E. Three-dimensional kinematics and kinetics of total knee arthroplasty during level walking using single plane video-fluoroscopy and force plates: A pilot study. *Gait Posture*. 2006 12;24(4):475-81.
95. Wearing SC, Urry S, Perlman P, Smeathers J, Dubois P. Sagittal plane motion of the human arch during gait: a videofluoroscopic analysis. *Foot Ankle Int*. 1998 Nov;19(11):738-42.

96. Yamaguchi S, Sasho T, Kato H, Kuroyanagi Y, Banks SA. Ankle and Subtalar Kinematics during Dorsiflexion-Plantarflexion Activities. *Foot & Ankle International*. 2009 April 01;30(4):361-6.
97. McHenry B, Long J, Harris GF. Foot and ankle motion analysis using dynamic radiographic (fluoroscopic) imaging. *Proceedings of GCMAS*; Grand Rapids, MI. ; 2012.
98. Kobayashi T, No Y, Yoneta K, Sadakiyo M, Gamada K. In Vivo Kinematics of the Talocrural and Subtalar Joints With Functional Ankle Instability During Weight-Bearing Ankle Internal Rotation: A Pilot Study. *Foot & Ankle Specialist*. 2013 June 01;6(3):178-84.
99. Fukano M, Kuroyanagi Y, Fukubayashi T, Banks SA. Three-dimensional kinematics of the talocrural and subtalar joints during drop landing. *Journal of Applied Biomechanics*. 2014;30(1):160-5.
100. Fukano M, Fukubayashi T. Changes in talocrural and subtalar joint kinematics of barefoot versus shod forefoot landing. *Journal of Foot and Ankle Research*. 2014;7(1):42.
101. Kobayashi T, Saka M, Suzuki E, Yamazaki N, Suzukawa M, Akaike A, et al. In Vivo Kinematics of the Talocrural and Subtalar Joints During Weightbearing Ankle Rotation in Chronic Ankle Instability. *Foot & Ankle Specialist*. 2014 February 01;7(1):13-9.
102. McHenry BD, Exten EL, Long J, Law B, Marks RM, Harris G. Sagittal Subtalar and Talocrural Joint Assessment With Weight-Bearing Fluoroscopy During Barefoot Ambulation. *Foot & Ankle International*. 2014 November 07.
103. Bottollier-Depois J, Chau Q, Bouisset P, Kerlau G, Plawinski L, Lebaron-Jacobs L. Assessing Exposure to Cosmic Radiation during Long-Haul Flights. *Radiat Res*. 2000 May;153(5, Part 1):pp. 526-532.
104. Anderst WJ, Baillargeon E, Donaldson III WF, Lee JY, Kang JD. Validation of a Noninvasive Technique to Precisely Measure In Vivo Three-Dimensional Cervical Spine Movement. *Spine*. 2011;36(6):E393-400.
105. Penney GP, Weese J, Little JA, Desmedt P, Hill DLG, Hawkes DJ. A comparison of similarity measures for use in 2-D-3-D medical image registration. *Medical Imaging, IEEE Transactions on*. 1998;17(4):586-95.
106. Brainerd EL, Baier DB, Gatesy SM, Hedrick TL, Metzger KA, Gilbert SL, et al. X-ray reconstruction of moving morphology (XROMM): precision, accuracy and applications in comparative biomechanics research. *Journal of Experimental Zoology Part A: Ecological Genetics and Physiology*. 2010;313A(5):262-79.

107. Bey MJ, Zauel R, Brock SK, Tashman S. Validation of a new model-based tracking technique for measuring three-dimensional, in vivo glenohumeral joint kinematics. *J Biomech E*. 2006;128(4):10.1115/1.2206199.
108. Bey MJ, Kline SK, Zauel R, Lock TR, Kolowich PA. Measuring dynamic in-vivo glenohumeral joint kinematics: Technique and preliminary results. *J Biomech*. 2008;41(3):711-4.
109. Anderst WJ, Vaidya R, Tashman S. A technique to measure three-dimensional in vivo rotation of fused and adjacent lumbar vertebrae. *The Spine Journal*. 2008 12;8(6):991-7.
110. Xia Q, Wang S, Kozanek M, Passias P, Wood K, Li G. In-vivo motion characteristics of lumbar vertebrae in sagittal and transverse planes. *J Biomech*. 2010 7/20;43(10):1905-9.
111. Martin DE, Greco NJ, Klatt BA, Wright VJ, Anderst WJ, Tashman S. Model-Based Tracking of the Hip: Implications for Novel Analyses of Hip Pathology. *J Arthroplasty*. 2011 1;26(1):88-97.
112. Anderst WJ, Zauel R, Bishop J, Demps E, Tashman S. Validation of three-dimensional model-based tibio-femoral tracking during running. *Med Eng Phys*. 2009 1;31(1):10-6.
113. Bey MJ, Kline SK, Tashman S, Zauel R. Accuracy of biplane x-ray imaging combined with model-based tracking for measuring in-vivo patellofemoral joint motion. *Journal of Orthopaedic Surgery and Research*. 2008;3(38):10.1186/1749-799X-3-38.
114. Abebe ES, Utturkar GM, Taylor DC, Spritzer CE, Kim JP, Moorman III CT, et al. The effects of femoral graft placement on in vivo knee kinematics after anterior cruciate ligament reconstruction. *J Biomech*. 2011 3/15;44(5):924-9.
115. Hanson GR, Suggs JF, Freiberg AA, Durbhakula S, Li G. Investigation of in vivo 6 DOF total knee arthroplasty kinematics using a dual orthogonal fluoroscopic system. *Journal of Orthopaedic Research*. 2006;24(5):974-81.
116. Myers CA, Torry MR, Peterson DS, Shelburne KB, Giphart JE, Krong JP, et al. Measurements of Tibiofemoral Kinematics During Soft and Stiff Drop Landings Using Biplane Fluoroscopy. *The American Journal of Sports Medicine*. 2011 August 01;39(8):1714-22.
117. de Asla RJ, Wan L, Rubash HE, Li G. Six DOF in vivo kinematics of the ankle joint complex: Application of a combined dual-orthogonal fluoroscopic and magnetic resonance imaging technique. *Journal of Orthopaedic Research*. 2006;24(5):1019-27.

118. Li G, Wan L, Kozanek M. Determination of real-time in-vivo cartilage contact deformation in the ankle joint. *J Biomech.* 2008;41(1):128-36.
119. Wan L, de Asla RJ, Rubash HE, Li G. In vivo cartilage contact deformation of human ankle joints under full body weight. *Journal of Orthopaedic Research.* 2008;26(8):1081-9.
120. de Asla R, Kozanek M, Wan L, Rubash H, Li G. Function of anterior talofibular and calcaneofibular ligaments during in-vivo motion of the ankle joint complex. *Journal of Orthopaedic Surgery and Research.* 2009;4(1):7.
121. Caputo AM, Lee JY, Spritzer CE, Easley ME, DeOrio JK, Nunley JA, et al. In Vivo Kinematics of the Tibiotalar Joint After Lateral Ankle Instability. *The American Journal of Sports Medicine.* 2009 November 01;37(11):2241-8.
122. Campbell KJ, Wilson KJ, LaPrade RF, Clanton TO. Normative rearfoot motion during barefoot and shod walking using biplane fluoroscopy. *Knee Surgery, Sports Traumatology, Arthroscopy.* 2014;June.
123. Peltz CD, Haladik JA, Hoffman SE, McDonald M, Ramo NL, Divine G, et al. Effects of footwear on three-dimensional tibiotalar and subtalar joint motion during running. *J Biomech.* 2014;47(11):2647-53.
124. Fernandez JW, Pandy MG. Integrating modeling and experiments to assess dynamic musculoskeletal function in humans. *Experimental Physiology.* 2006 March 01;91(2):371-82.
125. The Essential Physics of Medical Imaging. 2nd ed. Bushberg JT, Seibert JA, Leidholdt Jr EM, Boone JM, editors. Philadelphia, PA: Lippincott Williams & Wilkins; 2002.
126. Geise RA. Fluoroscopy: Recording of Fluoroscopic Images and Automatic Exposure Control. *Radiographics.* 2001 January 01;21(1):227-36.
127. Chen L, Armstrong CW, Raftopoulos DD. An investigation on the accuracy of three-dimensional space reconstruction using the direct linear transformation technique. *J Biomech.* 1994 4;27(4):493-500.
128. Tersì L, Fantozzi S, Stagni R. 3D Elbow Kinematics with Monoplanar Fluoroscopy: *In Silico* Evaluation. *EURASIP Journal on Advances in Signal Processing.* 2010;2010:doi:10.1155/2010/142989.
129. Bifulco P, Sansone M, Cesarelli M, Allen R, Bracale M. Estimation of out-of-plane vertebra rotations on radiographic projections using CT data: a simulation study. *Med Eng Phys.* 2002 5;24(4):295-300.

130. Tashman S. Comments on “validation of a non-invasive fluoroscopic imaging technique for the measurement of dynamic knee joint motion”. *J Biomech.* 2008 11/14;41(15):3290-1.
131. Miranda DL, Schwartz JB, Loomis AC, Brainerd EL, Fleming BC, Crisco JJ. Static and Dynamic Error of a Biplanar Videoradiography System Using Marker-Based and Markerless Tracking Techniques. *Journal of Biomechanical Engineering.* 2011;133(12):121002.
132. Iaquineto JM, Tsai R, Haynor DR, Fassbind MJ, Sangeorzan BJ, Ledoux WR. Marker-based validation of a biplane fluoroscopy system for quantifying foot kinematics. *Med Eng Phys.* 2014 3;36(3):391-6.
133. Kaptein BL, Shelburne KB, Torry MR, Erik Giphart J. A comparison of calibration methods for stereo fluoroscopic imaging systems. *J Biomech.* 2011 9/2;44(13):2511-5.
134. Li G, Van de Velde SK, Bingham JT. Validation of a non-invasive fluoroscopic imaging technique for the measurement of dynamic knee joint motion. *J Biomech.* 2008;41(7):1616-22.
135. Hedrick TL. Software techniques for two- and three-dimensional kinematic measurements of biological and biomimetic systems. *Bioinspiration & Biomimetics.* 2008;3.
136. Green DR, Sgarlato TE, Wittenberg M. Clinical biomechanical evaluation of the foot: a preliminary radiocinematographic study. *J Am Podiatry Assoc.* 1975 Aug;65(8):732-55.
137. Gefen A, Megido-Ravid M, Itzhak Y, Arcan M. Biomechanical analysis of the three-dimensional foot structure during gait: a basic tool for clinical applications. *Journal of Biomechanical Engineering.* 2000;122(6):630-9.
138. Giddings VL, Beaupre GS, Whalen RT, Carter DR. Calcaneal loading during walking and running. *Med Sci Sports Exerc.* 2000;32(3):627-34.
139. Gefen A. The in vivo elastic properties of the plantar fascia during the contact phase of walking. *Foot and Ankle International.* 2003;24(3):238-44.
140. Komistek RD, Stiehl JB, Buechel FF, Northcut EJ, Hajner ME. A Determination of Ankle Kinematics Using Fluoroscopy. *Foot & Ankle International.* 2000 April 01;21(4):343-50.
141. Wearing SC, Smeathers JE, Yates B, Sullivan PM, Urry SR, Dubois P. Errors in measuring sagittal arch kinematics of the human foot with digital fluoroscopy. *Gait Posture.* 2005 4;21(3):326-32.

142. Wearing SC, Smeathers JE, Yates B, Urry SR, Dubois P. Bulk compressive properties of the heel fat pad during walking: A pilot investigation in plantar heel pain. *Clin Biomech.* 2009 5;24(4):397-402.
143. Wainright WB, Spritzer CE, Lee JY, Easley ME, DeOrion JK, Nunley JA, et al. The Effect of Modified Broström-Gould Repair for Lateral Ankle Instability on In Vivo Tibiotalar Kinematics. *The American Journal of Sports Medicine.* 2012 September 01;40(9):2099-104.
144. Wang B, Roach KE, Kapron AL, Fiorentino NM, Saltzman CL, Singer M, et al. Accuracy and feasibility of high-speed dual fluoroscopy and model-based tracking to measure in vivo ankle arthrokinematics. *Gait Posture.* 2015;41(4):888-93.
145. Agostinelli S, Allison J, Amako K, Apostolakis J, Araujo H, Arce P, et al. Geant4 - A simulation toolkit. *Nuclear Instruments and Methods in Physics Research Section A: Accelerators, Spectrometers, Detectors and Associated Equipment.* 2003 /7/1;506(3):250-303.
146. Cranley K, Gilmore BJ, Fogarty GWA, Deponds L. Catalogue of diagnostic x-ray spectra and other data. *IPEM Report No. 78.* 1997.
147. Wu G, Siegler S, Allard P, Kirtley C, Leardini A, Rosenbaum D, et al. ISB recommendation on definitions of joint coordinate system of various joints for the reporting of human joint motion—part I: ankle, hip, and spine. *J Biomech.* 2002 4;35(4):543-8.
148. Grood ES, Suntay WJ. A Joint Coordinate System for the Clinical Description of Three-Dimensional Motions: Application to the Knee. *Journal of Biomechanical Engineering.* 1983 May 1;105(2):136-44.
149. McHenry B. Foot and ankle motion analysis using dynamic radiographic imaging.[dissertation]. Milwaukee, WI: Marquette University; 2013.

Appendix A. Steps for Model-Based Biplane Fluoroscopy

Collect image sequences at 200 fsp synchronously with Master and Slave cameras

1. Set up system: walkway, sources, II's, cameras, trigger, pulse
2. Attach white plastic sheets to II's to align x-ray sources
3. Open Motion Studio software and connect cameras
4. Mark the Master camera as the master camera in software
5. Attach metal sheets to collect grid images with system at level 1, save images
6. Lower system and check alignment
7. Place calibration cube in center of radiation area, record cube images and save
8. Instruct subject to stand in center of radiation area, lift opposite foot, and stand quietly. Record static images and save
9. Proceed with walking trials, saving sequences after each one

Use XROMM Undistortion for undistorting video sequences

10. Run XROMM Undistortion program
 - a. Open undistortion tool
 - b. Load a grid image (Master), grid points will automatically be selected
 - c. Compute the undistortion (Edit menu > Computer undistortion)
 - d. Save the parameters (File menu > Save LookUpTable and Points
 - i. Creates MasterGrid Look Up Table (Master001_UNDSTFORM file)
 - e. Repeat process for Slave camera
 - i. Creates SlaveGrid Look Up Table (Slave001_UNDSTFORM file)
11. Undistort images for Master camera (grid, cube, image sequences)
 - a. Load MasterGrid look up table
 - b. Undistort Master Cube image (File menu > Undistort single image)
 - c. Undistort master image sequences (File menu > Undistort image sequence)
 - i. Select input folder (distorted images) and output folder (undistorted)
12. Undistort images for Slave camera (grid, cube, image sequences)
 - a. Load SlaveGrid look up table
 - b. Undistort Slave Cube image (File menu > Undistort single image)
 - c. Undistort slave image sequences (File menu > Undistort image sequence)
 - i. Select input folder (distorted images) and output folder (undistorted)

Image Preprocessing in MATLAB

13. Event Detection
 - a. Get c3d pulse data from Vicon
 - b. Use m-file EventDetection to determine heel strike and toe off in dynamic trials
 - c. Crop the image sequences to stance phase
14. Flip images for Autoscoper

- a. For single image:
 - i. Cube=imread('Cube_MasterUND.tif');
 - ii. Temp=flipplr(Cube);
 - iii. imwrite(temp,'Cube_Flip_MasterUND.tif')
- b. For image sequences of Master images, use m-file MasterFlip
- c. For image sequences of Slave images, use m-file SlaveFlip

Use Hedrick Software for Generating DLT Coefficients

15. Run DLTcal5.m
 - a. Use modified 11 parameter DLT (select in drop down)
 - b. Load framespec_mm_EDIT file for calibration points (xyz locations of beads in cube)
 - c. Digitize points in image in same order as the locations defined in framespec file
 - i. Use Calibration_Cube_sheet for identifying correct bead numbers
 - d. Make sure calibration residual is less than 1 (smaller the better $\sim < .3$)
 - e. Calculate DLT coefficients from calibration cube for Master camera
 - i. Saves Master_DLTcoefs.csv file and xypts.csv file
 - f. Calculate DLT coefficients from calibration cube for Slave camera
 - i. Saves Slave_DLTcoefs.csv file and xypts.csv file
16. Merge DLT coefficients file from Calibration Cube
 - a. Save Master and Slave DLT files into 1 file: Master DLTs in 1st column, Slave DLTs in 2nd column – Merged_DLTcoefs.csv file

Use OsiriX to Segment Bones of Interest (protocol for CT scan)

17. Open OxiriX, Import CT image files: File > Import files..
18. Select study of interest in Database window
19. Open 2D view window by clicking its icon on top toolbar
20. Create a Region of Interest for a single bone
 - a. Set default ROI name: ROI > Set Default ROI Name > (One for each bone)
 - b. Select Closed Polygon Tool: Under tool bar, in row of buttons, Text drop down menu
 - c. Create ROI on each slice that contains the bone of interest, skip a few slices between ROI's and interpolate ROIs at end: ROI > ROI Volume > Generate missing ROIs
 - d. Go through and make sure each slice the ROIs are correctly sized
 - e. Save ROI to file: ROI > Save All ROIs of this Series
 - f. Repeat for each bone
21. Isolate Bones within Each ROI
 - a. Select ROI to isolate
 - b. Set all pixel values outside of ROI to black: ROI > Set Pixel Values to..
 - i. Make sure ROIs with same name as selected ROI is selected
 - ii. Make sure Outside ROIs button is selected
 - iii. Make sure To this new value button is selected (should be -3024)
 - c. Export new images containing only bone of interest as DICOM

- d. Repeat for each bone
- 22. Export .tif image stacks for each isolated bone
 - a. Select all of the series' to export to .tif image stacks
 - b. Export: File > Export > Export to TIFF
- 23. Create surface model of bone (needed for Geomagic)
 - a. In DICOM series of a bone, select 2D/3D button > 3D Surface Rendering
 - b. Select amount of decimation you want, try different amounts of smoothing
 - c. Select CT-Bone from predefined values drop down, or try other pixel values until model looks like you want
 - d. Save the model: Select 3D-SR button > Save as object file (.obj)
- 24. After segmentation, use ImageJ to create a stack of tif for each bone (save as 16-bit image)

Use Autoscooper for Model-based Tracking

- 25. Create MayaCam Files in MATLAB (specifies camera position and orientation; and dimension and location of image plane in lab space from DLT's)
 - a. Define variable coefs
 - i. `coefs= xlsread('Merged_DLTcoefs.csv');`
 - b. Run DLT2Maya function
 - i. `DLT2Maya(coefs, [1024,1024], 'StudyName_')`
 - ii. Saves MayaCamMaster.csv and MayaCamSlave.csv files
- 26. Create text files for trials using Notepad
 - a. Create text file for each trial with mayacam files, image sequences, bone model, and voxel size of model
 - i. Voxel Dimensions: depend on CT/MRI scan, check pixel spacing/slice thickness

Text File:

mayaCam_csv *complete path including file name to mayacam file for camera 1*
 CameraRootDir *complete path to undistorted video frames for camera 1*
 mayaCam_csv *complete path including file name to mayacam file for camera 2*
 CameraRootDir *complete path to undistorted video frames for camera 2*
 VolumeFile *complete path including file name to tif file containing bone volume*
 VoxelSize *in plane x in mm in plane y in mm slice thickness in mm*
 VolumeFlip *x y z*

- 27. Run Autoscooper
 - a. Open trial in Autoscooper (Open Trial button)
 - i. Add directory of where files are located by clicking on Add button once in the directory to locate files quicker
 - b. Add contrast and edge detection to both DRR and image sequence
 - i. Right click on *DrRender* or *RadRender* under a View1 or View2, select New Filter, select *Sobel* or *Contrast*
 - ii. *Sobel* filter allows for control of edge detection, *Contrast* filter controls for object/image contrast
 - iii. Filter properties can be adjusted by right clicking on created filter and selecting **Properties**

- iv. To save filter, right click on View and select **Export** (saves filter for both Drr and Rad for the view)
- v. To import filters previously saved, right click on View and select **Import**
- c. Move the pivot point to the middle of the bone
 - i. Click the **Move Pivot** button or hold the D key (solid lines turn to dotted lines)
 - ii. Rotate the volume so that you are looking down one axis, move coordinate system to middle of bone
 - iii. Rotate the volume to another axis and repeat
- d. Switch to camera views (Camera 1 and Camera 2)
- e. Manually manipulate DRR to best match 2 image sequences
 - i. Use bony landmarks to align bone in both camera views
 - ii. Use **Translate** (W key) and **Rotate** (E key) to move DRR
 - iii. Once aligned, lock the bone in position by pressing the **S key** (save point)
- f. Click on **Save Tracking** button to save initial pose. Include the study name, trial number, bone, tracking and initials in the file name
 - i. File name: **cad_dyn_trial_1_calc_tracking_JC_initialpose**
 - ii. Save type: xzypr, column, comma, none, mm, degrees; *don't interpolate until finished*
- g. Move ahead 5 to 10 frames using the slider on bottom panel, align bones again (depending on movement of bone)
- h. Click on **Save Tracking** button to save tracking after every few points (**remove _initialpose from file name**) (save type: xzypr, column, comma, none, mm, degrees; *don't interpolate until finished*)
- i. Once finished tracking
 - i. Save trial once (**Save Tracking** button, save over previous tracking)
 - ii. Save trial again as interpolated (**Save Tracking** button, add **_int** in file name), select **Spline**
 - iii. Load the interpolated tracking file by clicking the **Load Tracking** button and selecting the interpolated file
 - iv. Scroll through the image sequences to check if DRR follows the images. Write down frames where they are not aligned
 - v. Reload the original tracking file (**Load Tracking** button, select original non-interpolated file) and adjust DRR as necessary at frames
 - 1. To move a saved point, create a new one over the old one
 - vi. Save **original tracking** again (over previous tracking file, *don't interpolate*)
 - vii. Save **new interpolation** tracking (over previous interpolation file)
 - viii. Check interpolation again
- j. Once manual tracking is completed to the best visual match, load the final original tracking file (not interpolated)
 - i. Go to the first save point and click the Track button

- ii. Input in the Range: From Frame: current frame number; To Frame: current frame number (i.e. 70 to 70). Initial Guess: Current Frame. Then press ok
- iii. The bone model should move slightly to the optimal match
 - 1. If model moves out of alignment and looks worse than manual match, press Ctrl+Z to undo, and move on to next save point
- iv. Perform automated tracking on each save point in the sequence
- v. When finished save tracking with _AUTO in file name (don't interpolate)
- vi. Save again with interpolation

Autoscooper Shortcuts and keys:

Ctrl + scroll – Zoom in/out of camera view

Ctrl + LMB – Pan camera view

D (press and hold) – Move pivot point

W – Translation

E – Rotation

S – Create keyframe (save point)

T – Track

R – Retrack (don't use)

H – Hide DRR

=/- – increase/decrease size of axes

+/- – advance/go back one frame (keypad)

Use Geomagic to Define ACS (Geomagic Wrap Version 2014.4.0)

28. Open and Clean up Model:

- a. Import/Open: bone_model.obj file; Select units in millimeters; Select no for Mesh Doctor
- b. Clean up model in Polygons Tab: fill holes, remove spikes
- c. Save as: bone_model_cleaned.obj

29. Calcaneus: Need Origin, SI Point, ML Point

- a. Origin: At midpoint of facet line
- b. SI axis: line perpendicular to facet line and tangent to inferior surface, passing through origin
- c. ML axis: line perpendicular to SI axis and lateral wall, passing through origin
- d. AP axis: cross product of SI and ML axes
 - Create LINE connecting most lateral point of posterior facet and most medial point of middle facet (Facet Line)
 - Create POINT at midpoint of Facet Line (Origin)
 - Create PLANE on inferior surface of calcaneus (Inferior Plane)
 - Create LINE perpendicular to Inferior Plane through the Origin (SI Line)
 - Create POINT at end of SI Line (SI Point)
 - Create PLANE on lateral wall of calcaneus (Lateral Plane)

- Create PLANE parallel to Inferior Plane through the Origin (Horizontal Plane)
 - Create PLANE perpendicular to Horizontal and Lateral Planes through the Origin (ML Plane)
 - Create POINT at intersection of 3 planes (ML Point)
 - Extract Points: Origin, SI Point, ML Point
30. Talus: Need Origin, AP Point, ML Point
- a. Origin: At center of sphere encompassing body of talus
 - b. ML axis: line perpendicular to sphere, passing through origin
 - c. AP axis: line parallel to line connecting anterior/posterior edge of trochlea, passing through origin
 - d. SI axis: cross product of ML and AP axes
 - Create POINT at center of sphere encompassing body of talus (Origin)
 - Create PLANE on superior surface of talus (Superior Plane)
 - Create PLANE parallel to Superior Plane through the Origin (Horizontal Plane)
 - Create LINE defining anterior edge of trochlea tali (AntML Line)
 - Create LINE defining posterior edge of trochlea tali (PostML Line)
 - Create LINE connecting midpoints of AntML and PostML Lines (Midpt Line)
 - Create PLANE perpendicular to Midpt Line (ML Plane)
 - Create LINE at intersection of Horizontal Plane and ML Plane (ML Line)
 - Create POINT at end of ML Line (ML Point)
 - Create PLANE perpendicular to ML Line (AP Plane)
 - Create LINE at intersection of Horizontal Plane and AP Plane (AP Line)
 - Create POINT at end of AP Line (AP Point)
 - Extract Points: Origin, AP Point, ML Point
31. Tibia: Need Origin, SI Point, AP Point
- a. Origin: At center of tibial plafond
 - b. SI axis: line perpendicular to tibial plafond going superiorly through midpoint of tibial shaft, passing through origin
 - c. AP axis: line perpendicular to anterior surface of tibia and SI axis, passing through origin
 - d. ML axis: cross product of AP and SI axes
 - Create LINE at proximal end of tibial shaft in the anterior/posterior direction (APprox Line)
 - Create LINE at proximal end of tibial shaft in the medial/lateral direction (MLprox Line)
 - Create POINT at intersection of 2 lines (SI Point)
 - Create PLANE at tibial plafond (Tibial Plafond)
 - Create LINE between Tibial Plafond plane and SI Point (SI Line)
 - Create POINT at intersection of Tibial Plafond and SI Line (Origin)
 - Create PLANE on anterior surface of tibia (Anterior Plane)
 - Create PLANE perpendicular to MLprox Line (AP Plane)

- Create POINT at intersection of 3 planes (AP Point)
 - Extract Points: Origin, SI Point, AP Point
- Geomagic Features:**
 Zoom: roll middle mouse button
 Pan: Alt + middle mouse button
 Rotation: click and hold middle mouse button
 Use Axes Indicator in bottom right of screen for quick rotations about axes
 In Features tab, use Feature Visibility to toggle features on/off

Run Kinematic Model to determine Joint Motion

32. Create folder of Autoscooper output files in Kinematic Model directory
 - a. In directory, have Autoscooper file folder and Geomagic points file
 - b. Run m-file MODEL to calculate Talocrural and Subtalar kinematics
 - i. Use static pose to determine neutral position

Filter Kinematic Output

33. Open kinematic output files
 - a. Delete extra sheets and crop to stance phase if not already
 - b. Save as CSV file: Trial#_Kinematics.csv
34. Put all cropped kinematics .csv files in Filter director, within Kinematic Model
35. Type butterBatch into the MATLAB command line
36. Select a csv data file
 - a. Enter the cutoff frequency: 20 Hz
 - b. Recording frequency (i.e. frame rate): 200 Hz
 - c. Filter type: low
 - i. Files are saved in the original directory with BUTTER## appended to the end of the original file name (## specifies the cutoff frequency)

Analyze Results

37. Create folder of filtered results in Kinematic Model Directory
 - a. Run m-file FINAL_RESULTS to normalize to the static pose and plot talocrural and subtalar kinematics to 100% stance phase
 - b. Variables AVG_TALOCRURAL_JT and AVG_SUBTALAR_JT have max ROM values of each joint
 - i. Plantarflexion, Dorsiflexion, Eversion, Inversion, Abduction, Adduction

Software Needed:

- MATLAB for image processing, DLT, Filtering and Kinematic Model
- Motion Studio 64 for high speed camera data collection (Motion Studio 64 Version 2.10.05)
- XROMM Undistorter for image distortion correction (XROMM Undistorter v1.0.0 for Windows)

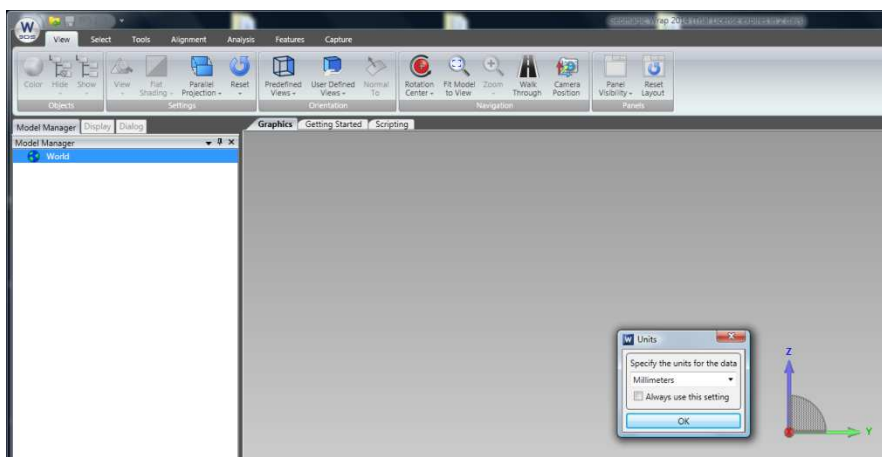
<https://wiki.brown.edu/confluence/display/ctx/Recent+Changes+and+DOWNLOADS>

- *Hedrick Digitizing Software for DLT coefficients* ([DigitizingTools_20141017.zip](http://www.unc.edu/~thedrick/software1.html))
<http://www.unc.edu/~thedrick/software1.html>
- *XROMM Autoscopers for Model-based Tracking* ([AutoScoper 1.13 install package](https://wiki.brown.edu/confluence/display/ctx/XROMM+AutoScoper))
<https://wiki.brown.edu/confluence/display/ctx/XROMM+AutoScoper>
- *OxiriX for Bone Segmentation* (OsiriX software Version 3.8.1, 32-bit)
- *ImageJ for making stack of .tifs* (ImageJ version 1.42q)
- *Geomagic for Defining ACS* (Geomagic Wrap Version 2014.4.0)

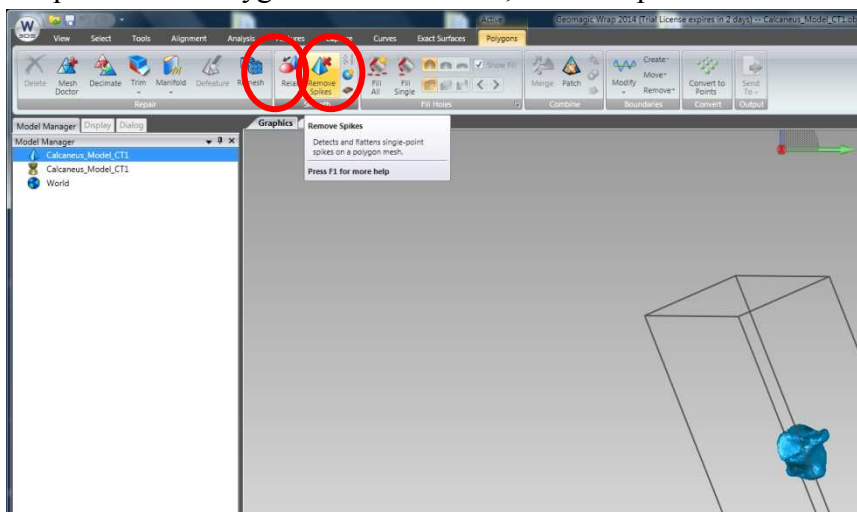
Appendix B. Using Geomagic to Define Anatomical Coordinate Systems

Open and Clean up Model:

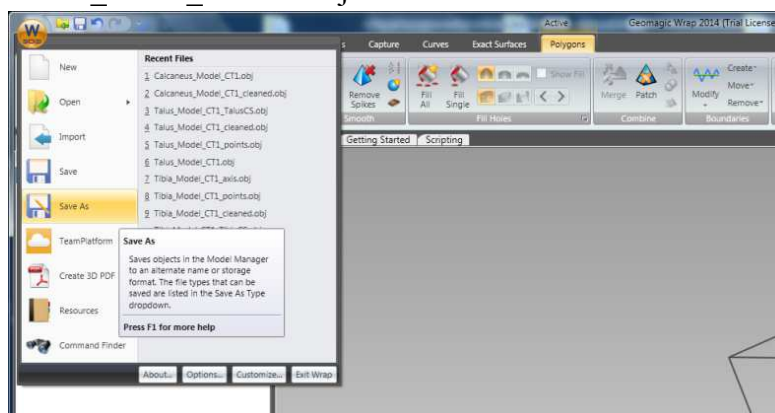
1. Import/Open: bone_model.obj file; Select units in millimeters; Select no Mesh Doctor



2. Clean up model in Polygons Tab: fill holes, remove spikes



3. Save as: bone_model_cleaned.obj



Calcaneus: Need Origin, SI Point, ML Point

Origin: At midpoint of facet line

SI axis: line perpendicular to facet line and tangent to inferior surface, passing through origin

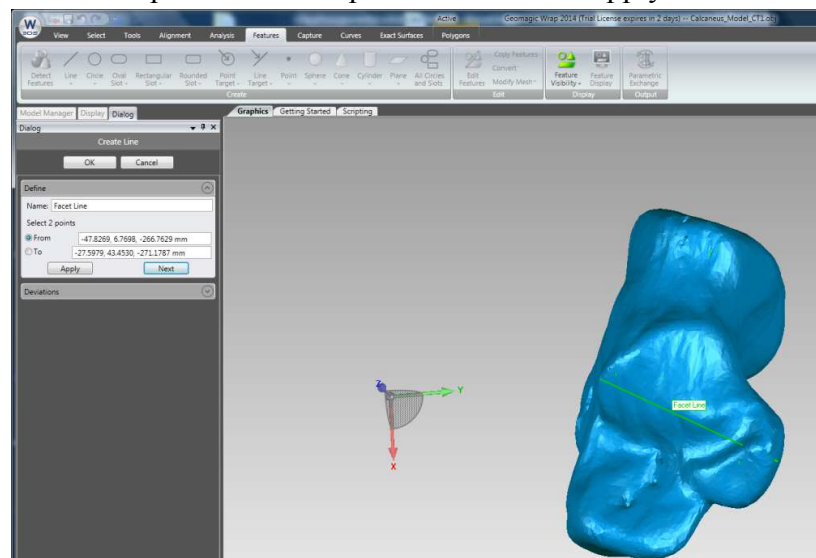
ML axis: line perpendicular to SI axis and lateral wall, passing through origin

AP axis: cross product of SI and ML axes

In Features Tab:

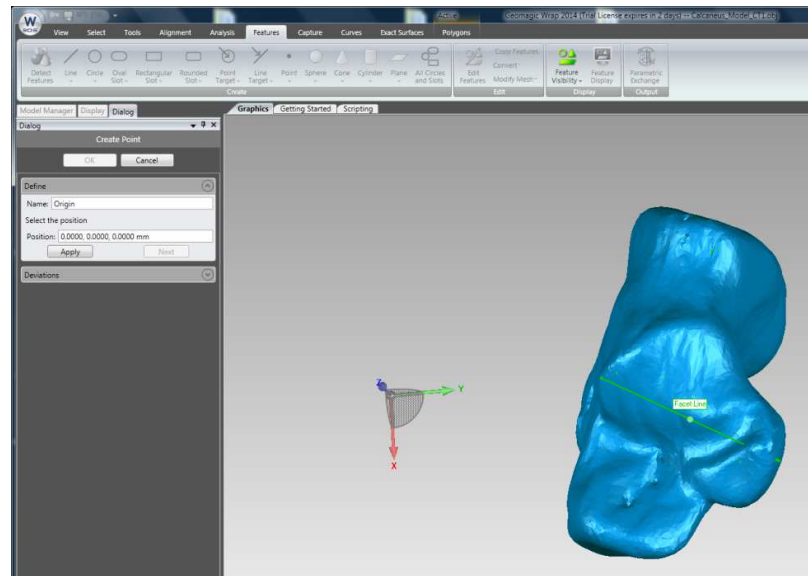
1. Create LINE connecting most lateral point of posterior facet and most medial point of middle facet (Facet Line)

- Line > 2 points > Select points on facets > Apply > Ok

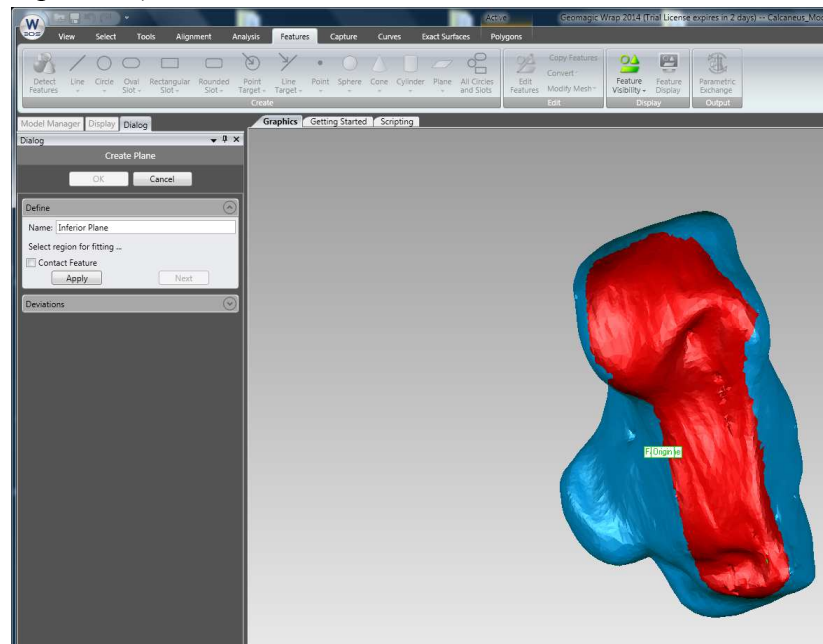


2. Create POINT at midpoint of Facet Line (Origin)

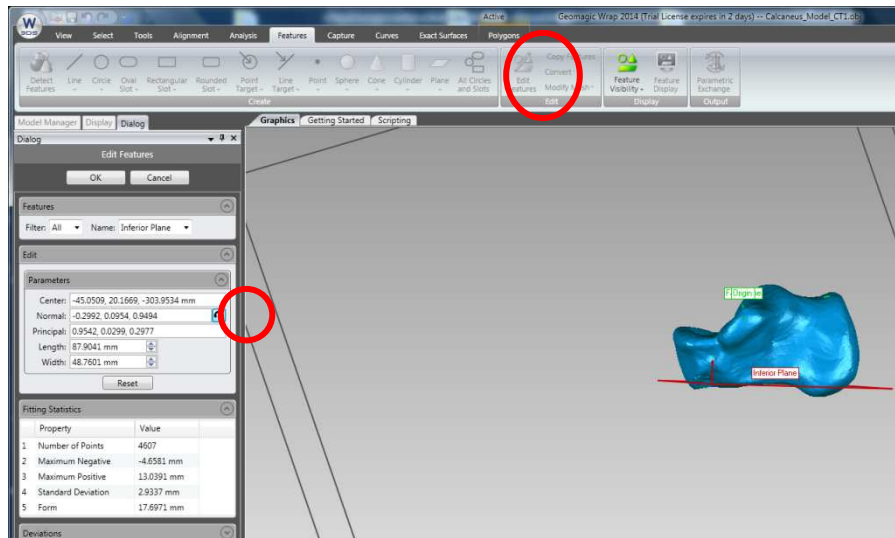
- Point > Parameters > Move cursor along middle of line until green, select point > Apply > Ok



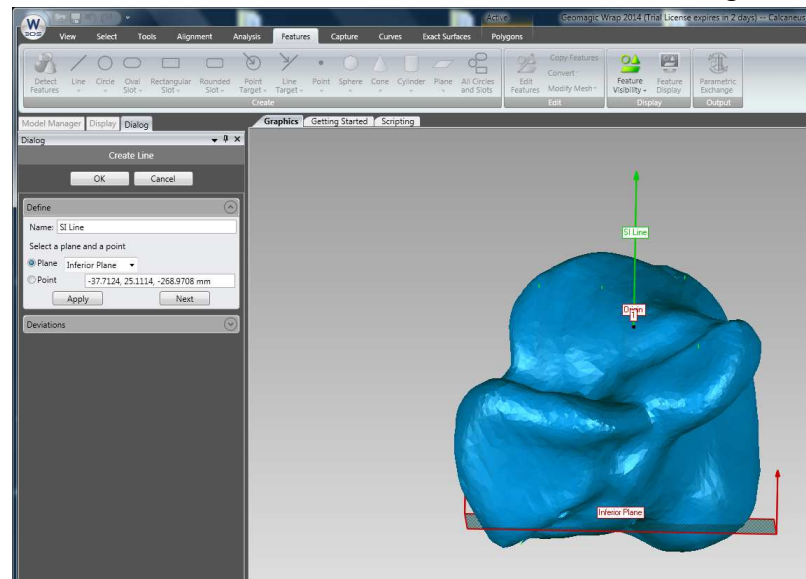
3. Create PLANE on inferior surface of calcaneus (Inferior Plane)
 - Plane > Best Fit > Select inferior surface of bone > Apply (check plane position) > Ok



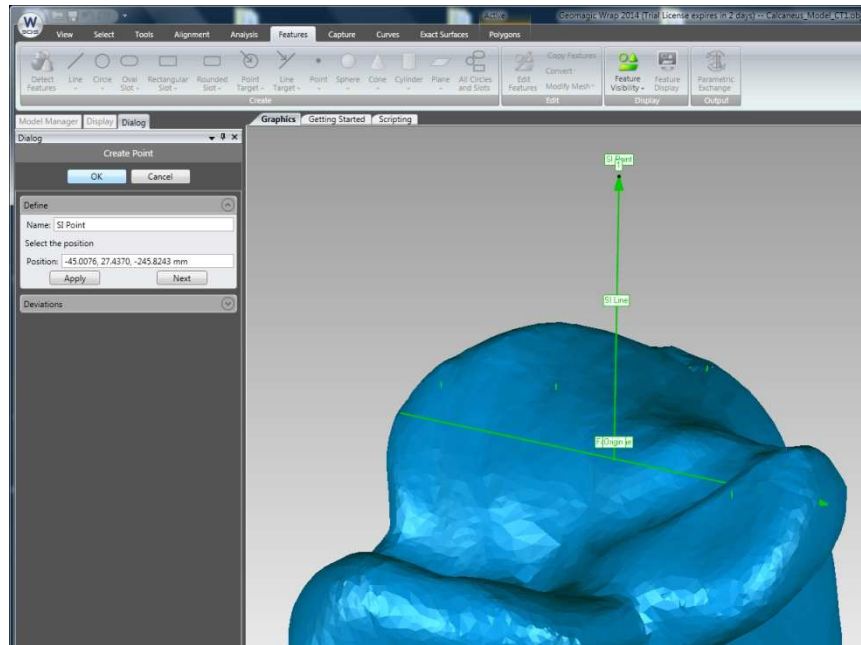
- Make sure plane normal is pointed superiorly: Edit Features > Select plane > reverse direction > Ok



4. Create LINE perpendicular to Inferior Plane through the Origin (SI Line)
 - Line > Plane and Point > Select Inferior Plane and Origin > Apply > Ok

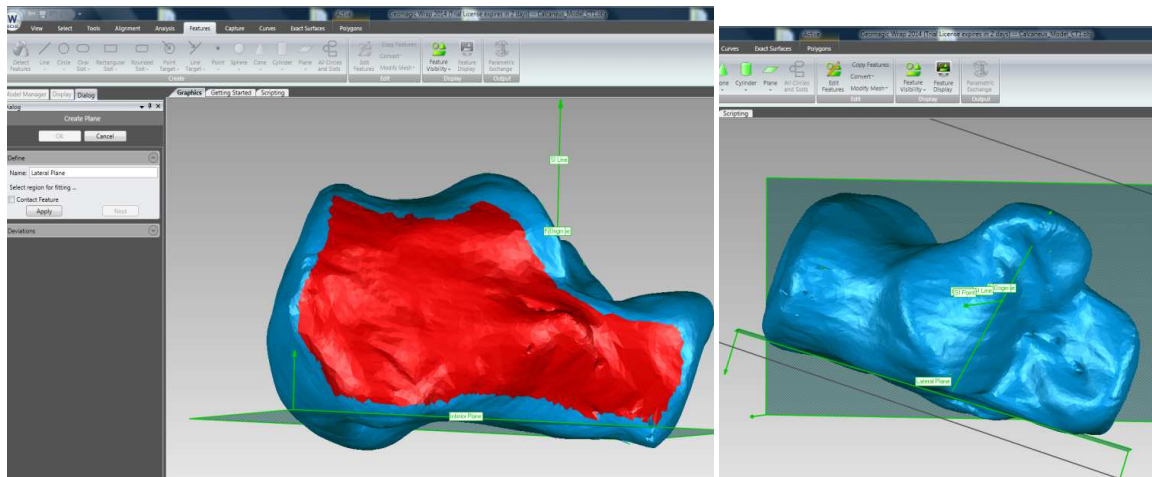


- Line should be pointing superiorly
5. Create POINT at end of SI Line (SI Point)
 - Point > Parameters > Move cursor to end of line until green, select point > Apply > Ok



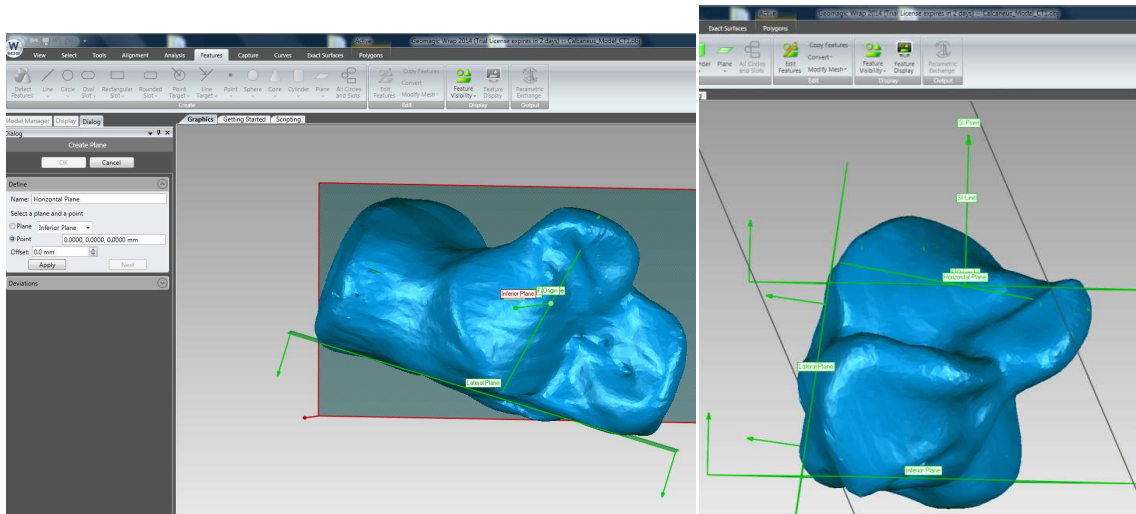
6. Create PLANE on lateral wall of calcaneus (Lateral Plane)

- Plane > Best Fit > Select lateral side of bone > Apply (check position) > Ok



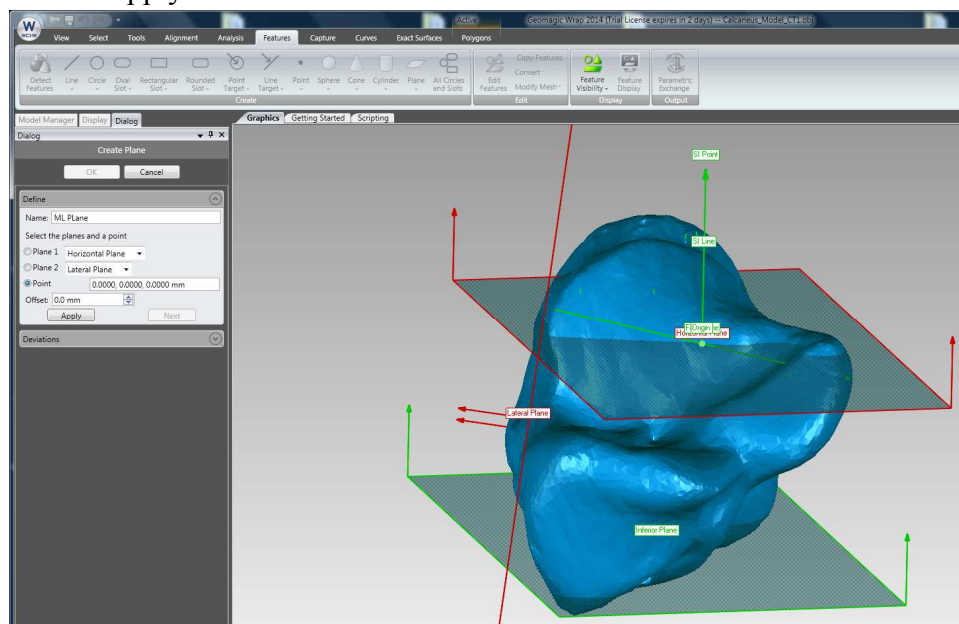
7. Create PLANE parallel to Inferior Plane through the Origin (Horizontal Plane)

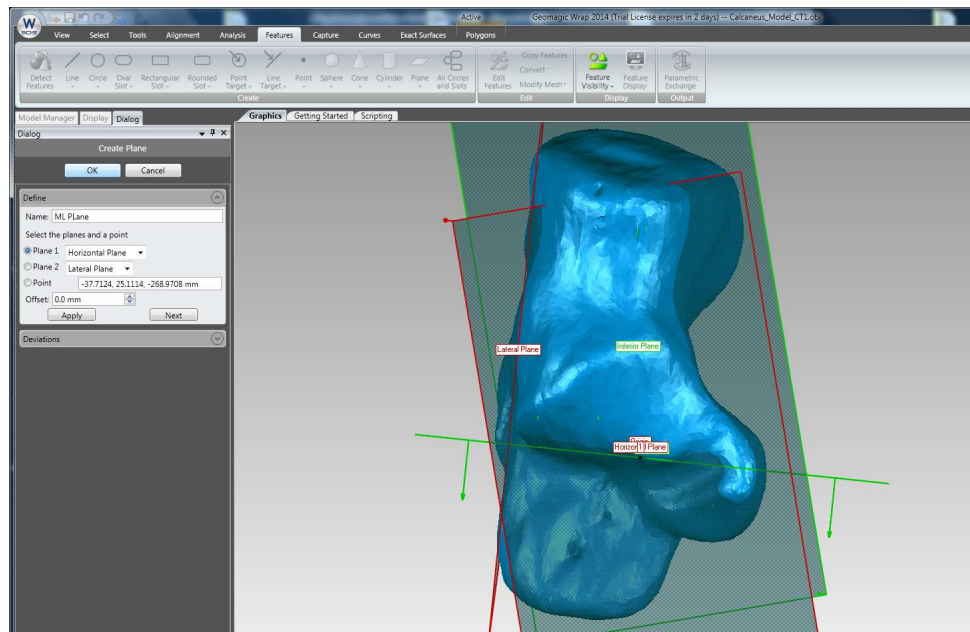
- Plane > Parallel through point > Select Inferior Plane and Origin > Apply > Ok



8. Create PLANE perpendicular to Horizontal and Lateral Planes through the Origin (ML Plane)

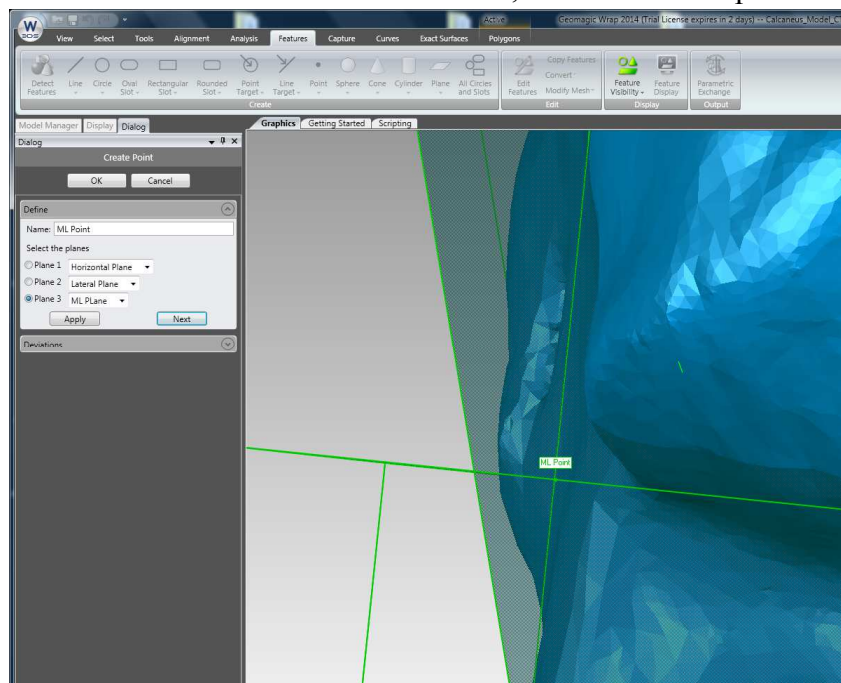
- Plane > Perpendicular through point > Select Horizontal, Lateral, Origin > Apply > OK





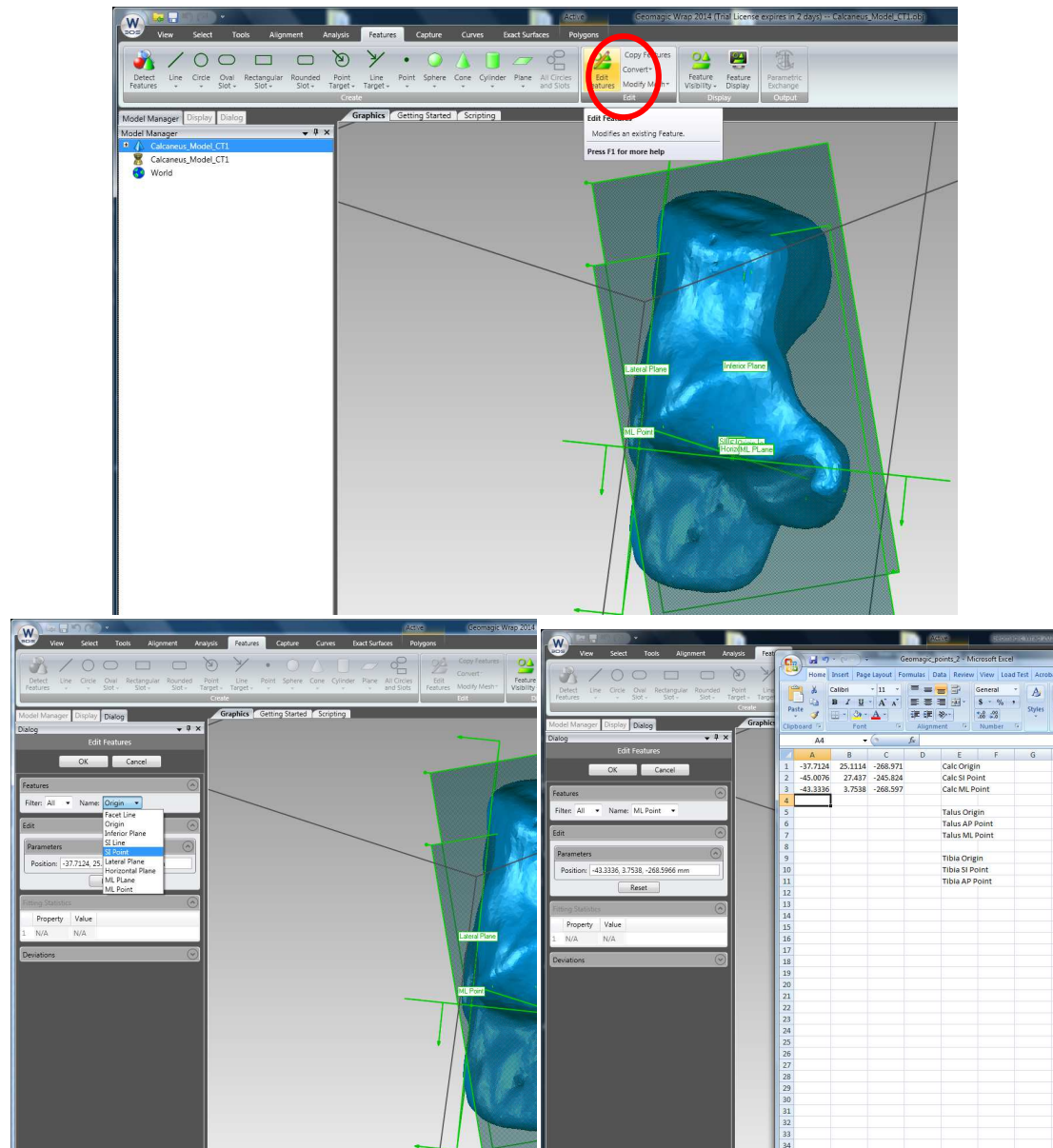
9. Create POINT at intersection of 3 planes (ML Point)

- Point > 3 Planes > Select Horizontal, Lateral and ML planes > Apply > Ok



10. Extract Points: Origin, SI Point, ML Point

- Edit Features > Select Point > Copy XYZ positions to excel file



Talus: Need Origin, AP Point, ML Point

Origin: At center of sphere encompassing body of talus

ML axis: line perpendicular to sphere, passing through origin

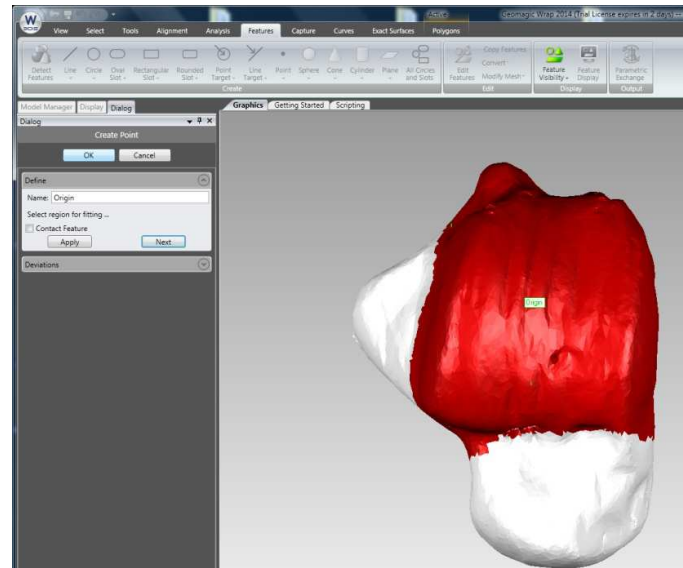
AP axis: line parallel to line connecting anterior/posterior edge of trochlea, passing through origin

SI axis: cross product of ML and AP axes

In Features Tab:

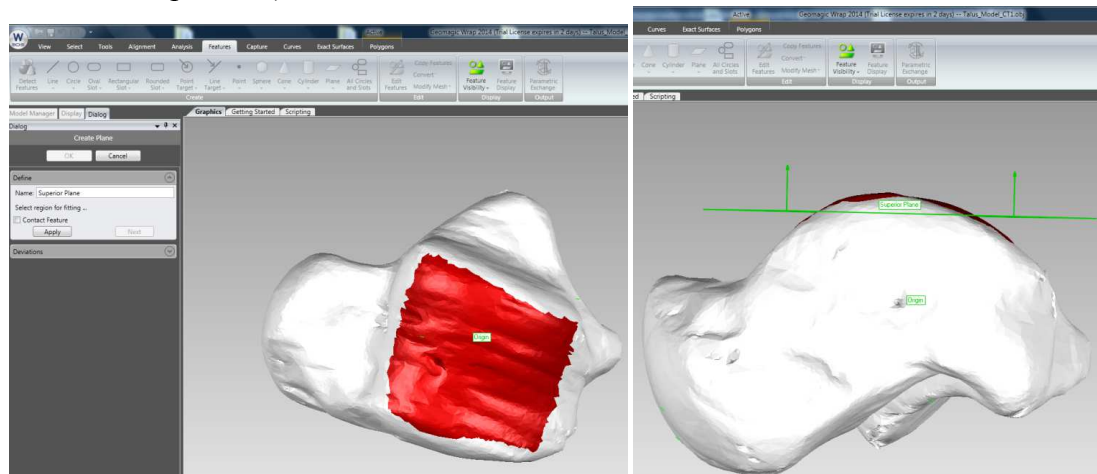
1. Create POINT at center of sphere encompassing body of talus (Origin)
 - Point > Sphere > Select body of talus > Apply > Ok

- Go to Edit Features > Select Origin > Copy points to use in following steps



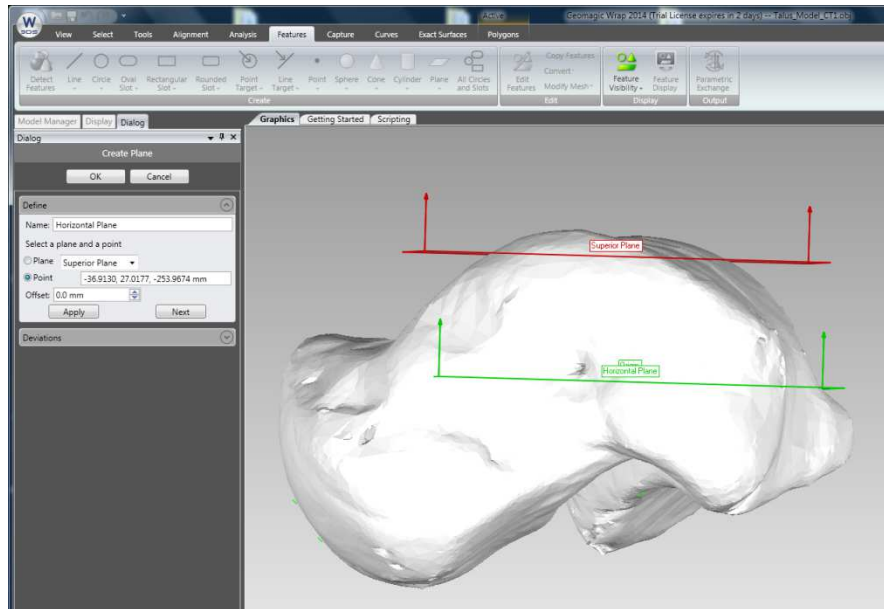
2. Create PLANE on superior surface of talus (Superior Plane)

- Plane > Best Fit > Select superior surface of talus > Apply (check position) > Ok

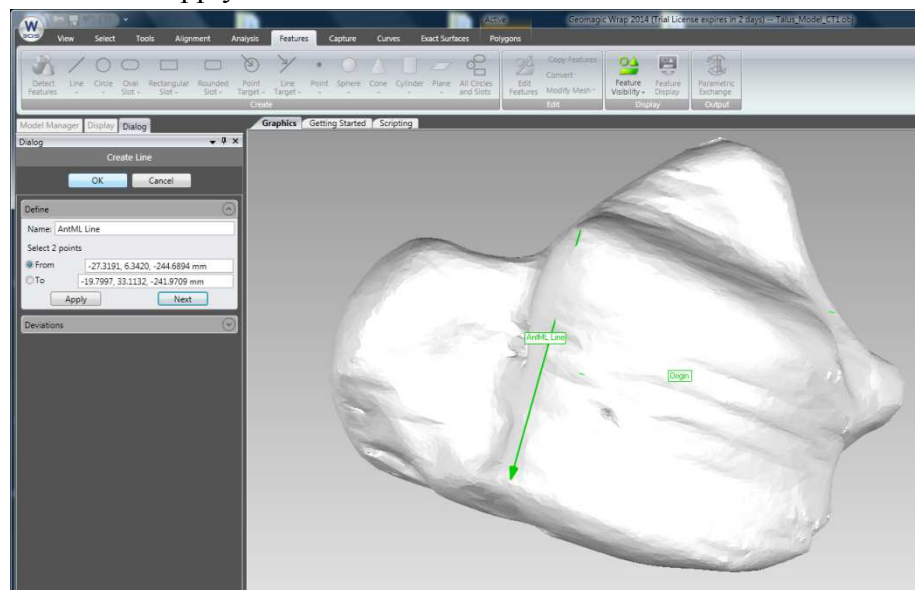


3. Create PLANE parallel to Superior Plane through the Origin (Horizontal Plane)

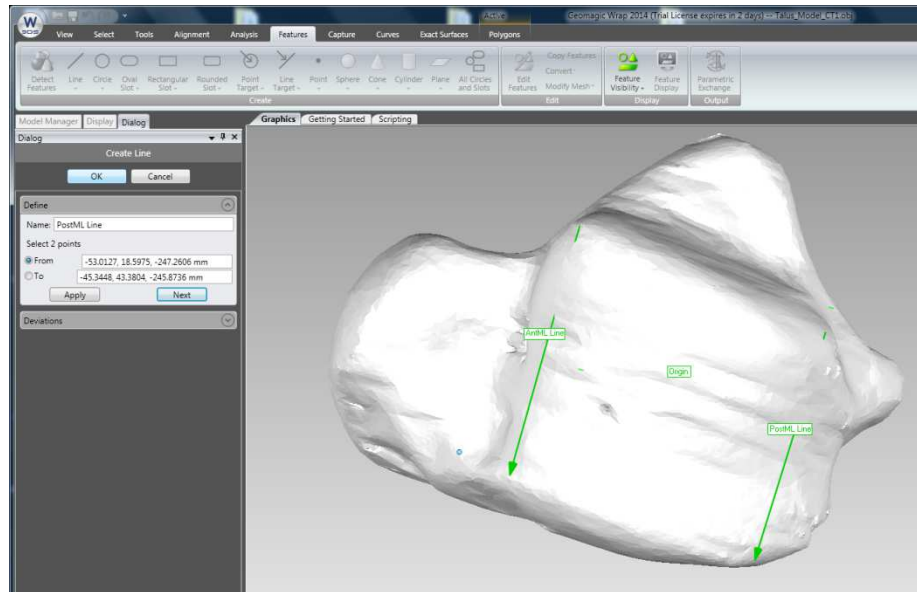
- Plane > Parallel through point > Select Superior Plane and Origin > Apply > Ok



4. Create LINE defining anterior edge of trochlea tali (AntML Line)
 - Line > 2 points > Select anteriomedial and anteriolateral points of trochlea tali > Apply > Ok

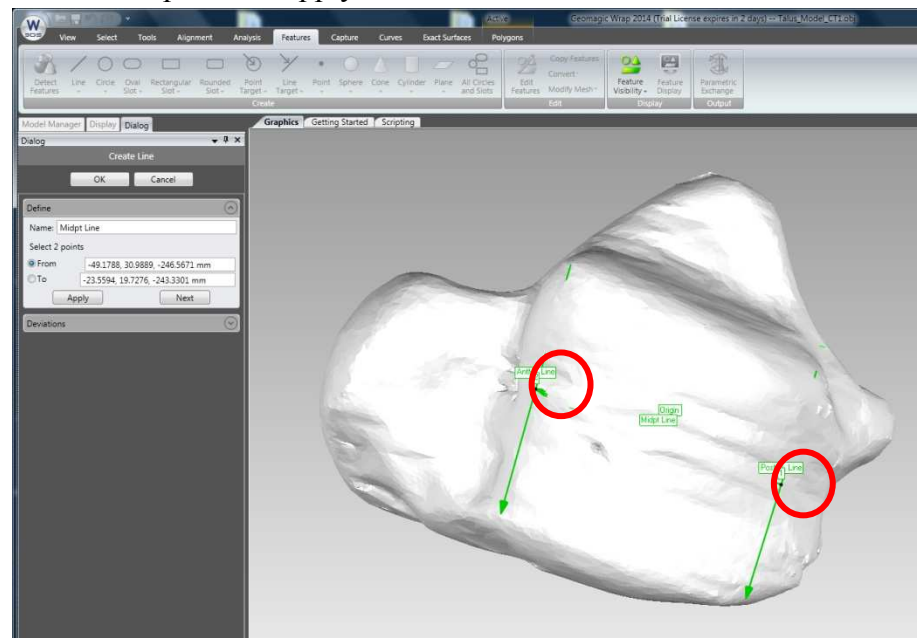


5. Create LINE defining posterior edge of trochlea tali (PostML Line)
 - Line > 2 points > Select posteriomedial and posteriolateral points of trochlea tali > Apply > Ok



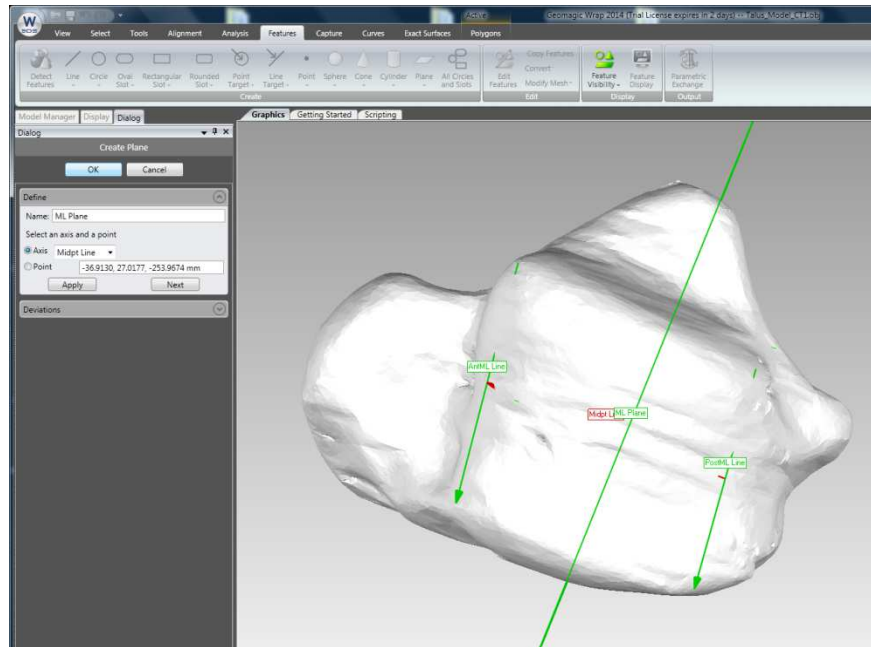
6. Create LINE connecting midpoints of AntML and PostML Lines (Midpt Line)

- Line > 2 Points > Move cursor to middle of Ant/Post ML line until green, select points > Apply > Ok

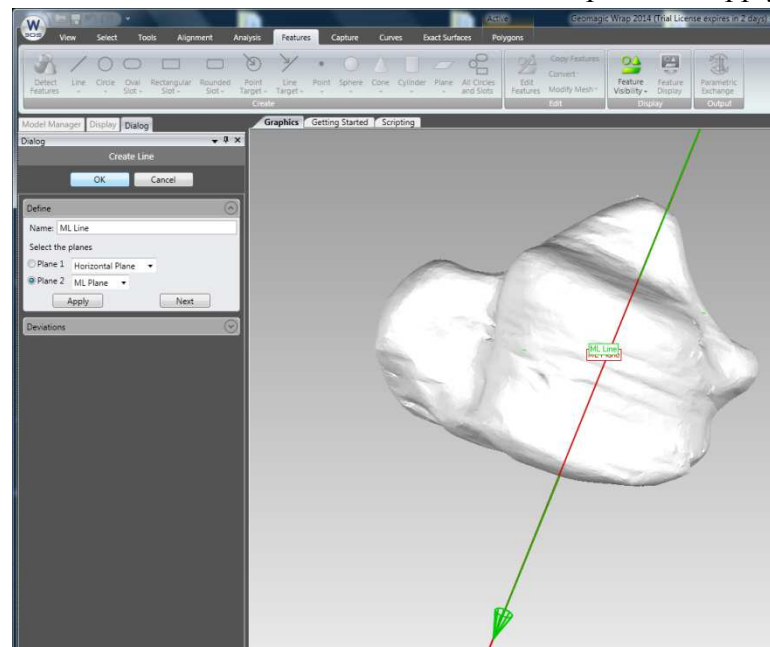


7. Create PLANE perpendicular to Midpt Line (ML Plane)

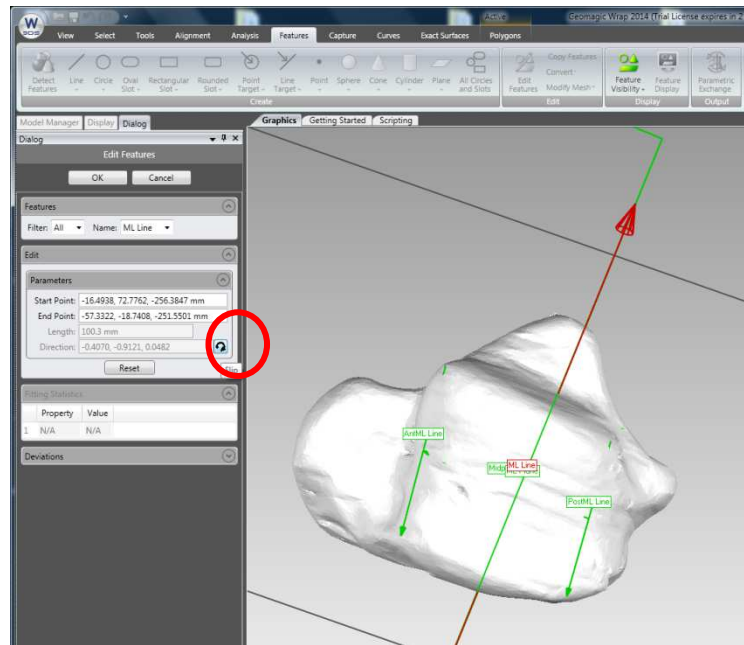
- Plane > Perpendicular to Axis > Select Midpt Line and Origin > Apply > Ok



8. Create LINE at intersection of Horizontal Plane and ML Plane (ML Line)
 - Line > 2 Planes > Select Horizontal and ML planes > Apply > Ok

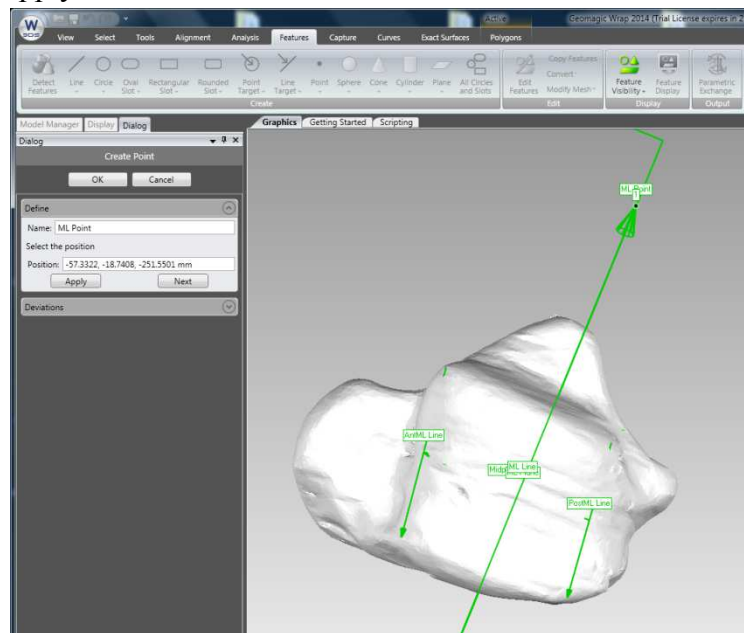


- Make sure line points laterally: Edit Features > Select line > reverse direction > Ok



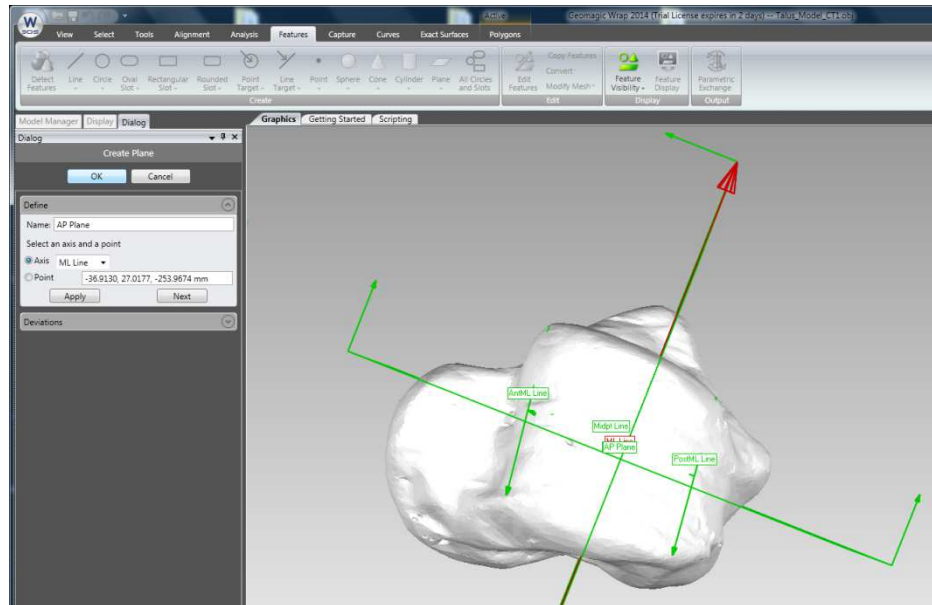
9. Create POINT at end of ML Line (ML Point)

- Point > Parameters > Move cursor to end of line until green, select point > Apply > Ok



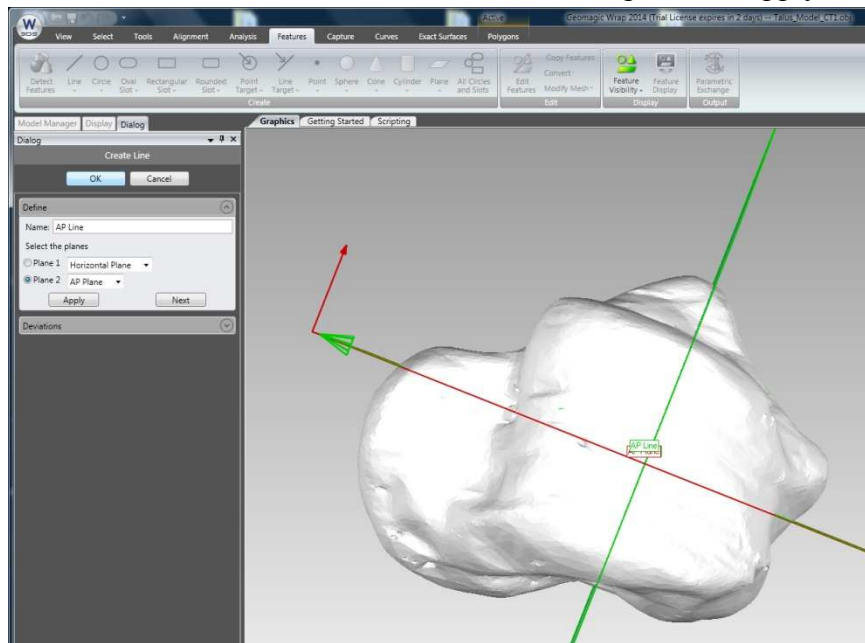
10. Create PLANE perpendicular to ML Line (AP Plane)

- Plane > Perpendicular to Axis > Select ML Line and Origin > Apply > Ok



11. Create LINE at intersection of Horizontal Plane and AP Plane (AP Line)

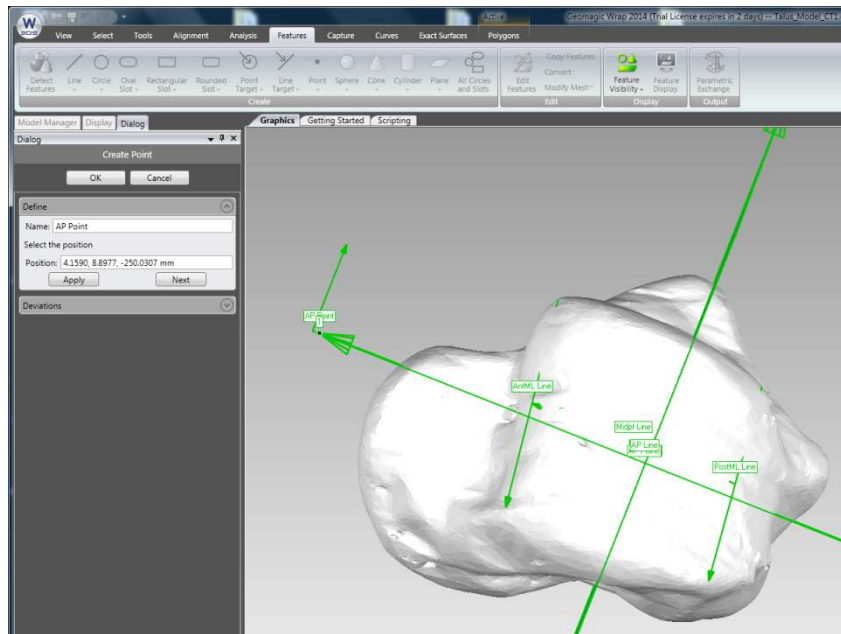
- Line > 2 Planes > Select Horizontal and AP planes > Apply > Ok



- Make sure line points anteriorly: Edit Features > Select line > reverse direction > Ok

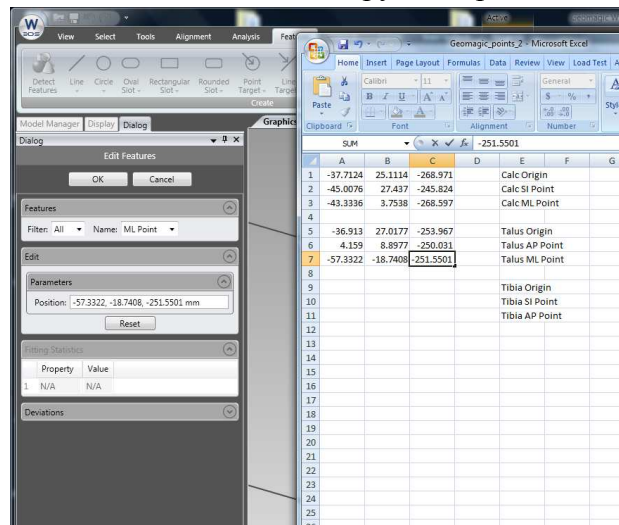
12. Create POINT at end of AP Line (AP Point)

- Point > Parameters > Move cursor to end of line until green, select point > Apply > Ok



13. Extract Points: Origin, AP Point, ML Point

- Edit Features > Select Point > Copy XYZ positions to excel file



Tibia: Need Origin, SI Point, AP Point

Origin: At center of tibial plafond

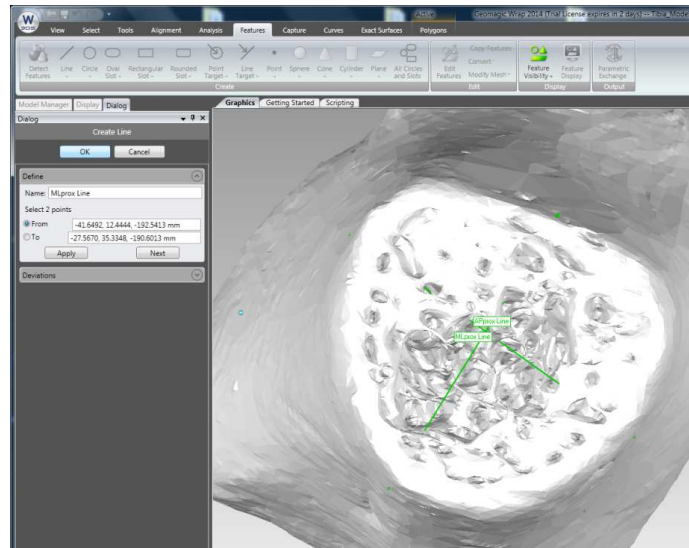
SI axis: line perpendicular to tibial plafond going superiorly through midpoint of tibial shaft, passing through origin

AP axis: line perpendicular to anterior surface of tibia and SI axis, passing through origin

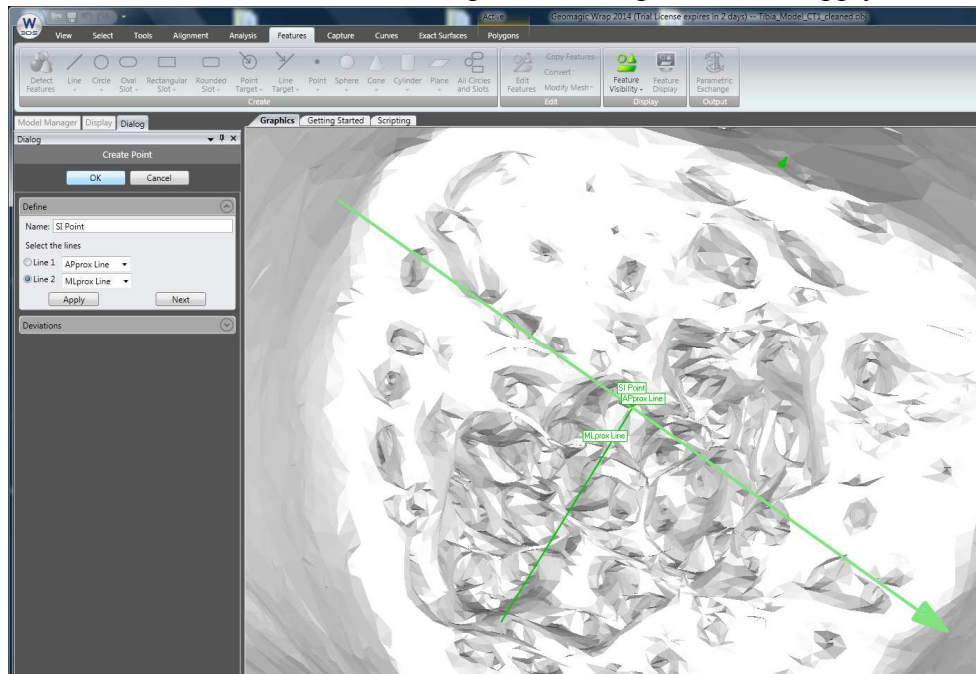
ML axis: cross product of AP and SI axes

In Features Tab:

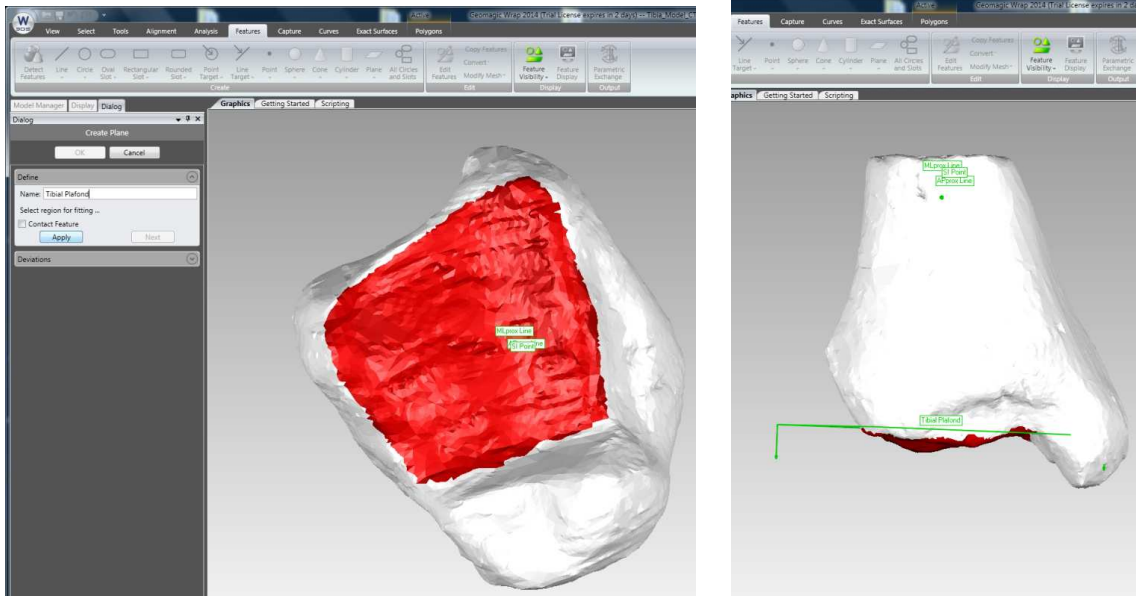
1. Create LINE at proximal end of tibial shaft in the anterior/posterior direction (APprox Line)
 - Line > 2 Points > Select anterior and posterior points > Apply > Ok
2. Create LINE at proximal end of tibial shaft in the medial/lateral direction (MLprox Line)
 - Line > 2 Points > Select medial and lateral points > Apply > Ok



3. Create POINT at intersection of 2 lines (SI Point)
 - Point > 2 Lines > Select APprox and MLprox lines > Apply > Ok

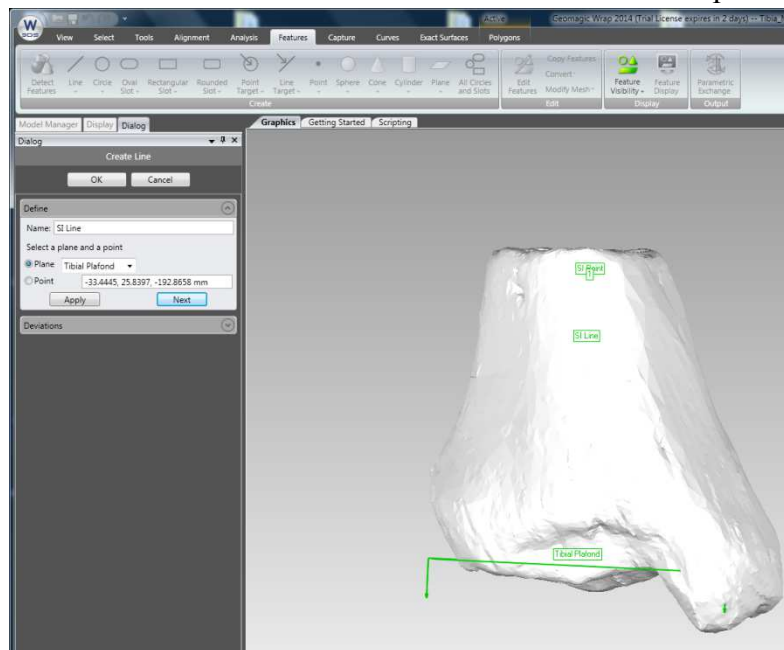


4. Create PLANE at tibial plafond (Tibial Plafond)
 - Plane > Best Fit > Select area of tibial plafond > Apply > Ok



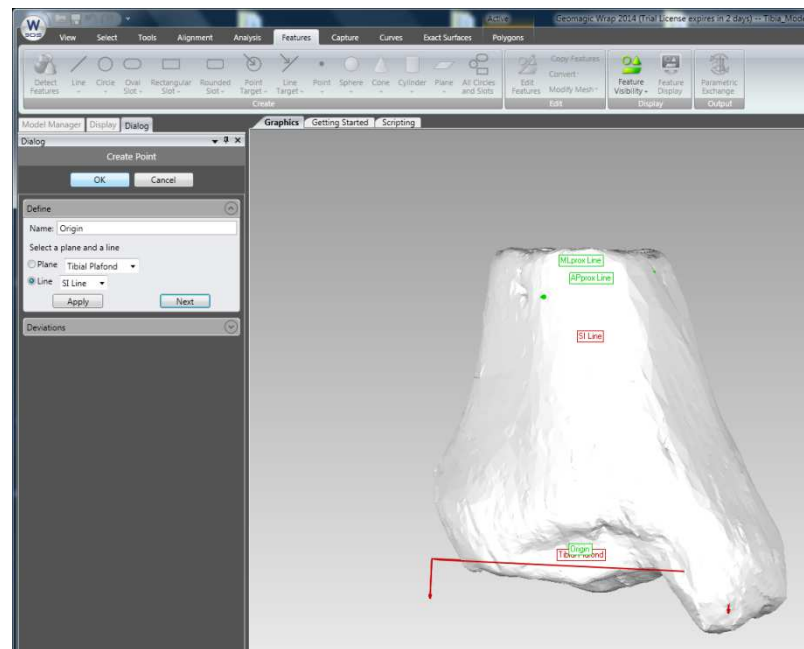
5. Create LINE between Tibial Plafond plane and SI Point (SI Line)

- Line > Plane and Point > Select Tibial Plafond and SI point > Apply > Ok



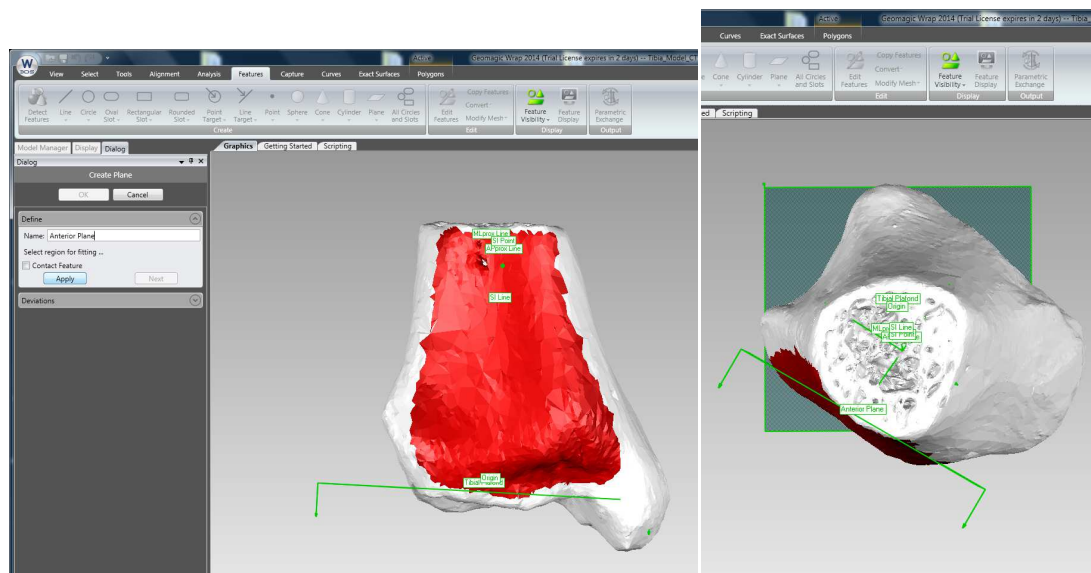
6. Create POINT at intersection of Tibial Plafond and SI Line (Origin)

- Point > Plane and Line > Select Tibial Plafond and SI Line > Apply > Ok



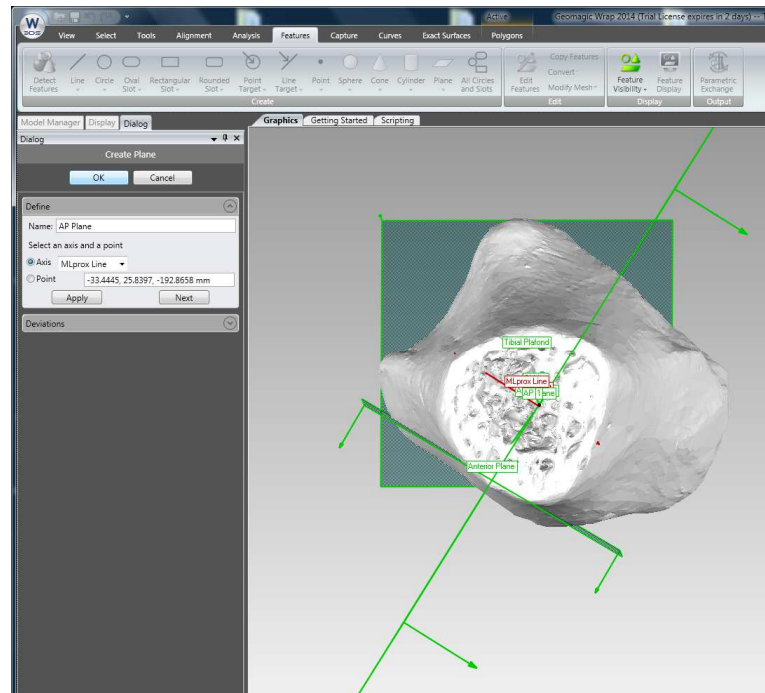
7. Create PLANE on anterior surface of tibia (Anterior Plane)

- Plane > Best Fit > Select anterior surface of bone > Apply (check position) > Ok



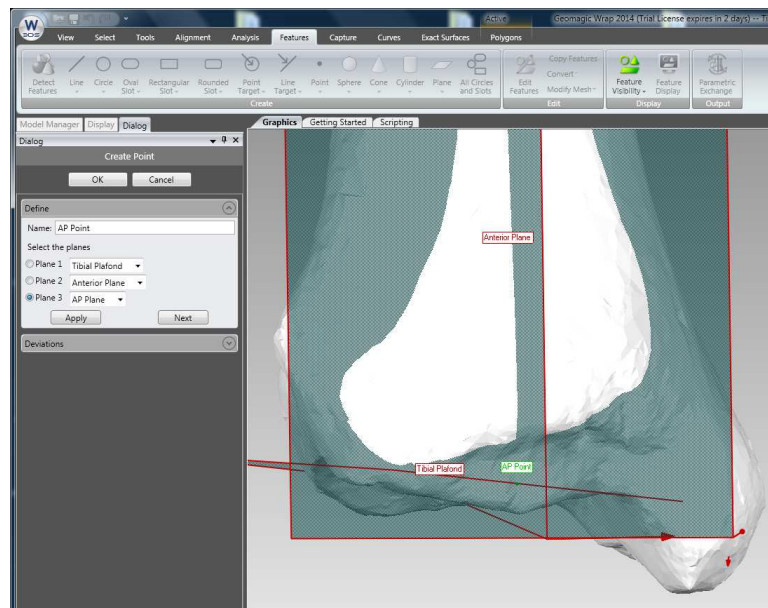
8. Create PLANE perpendicular to MLprox Line (AP Plane)

- Plane > Perpendicular to Axis > Select MLprox Line and SI Point > Apply > Ok



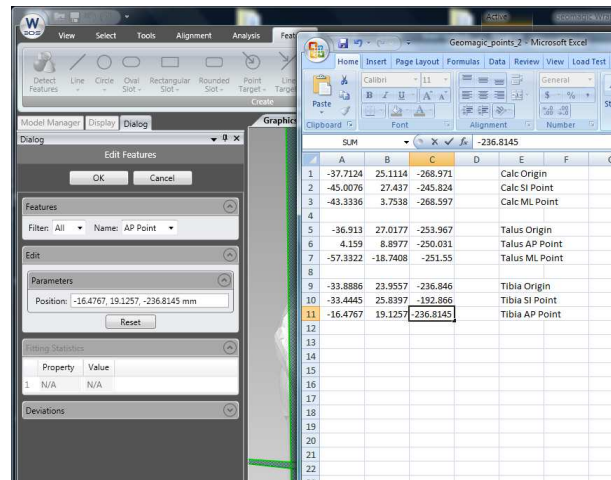
9. Create POINT at intersection of 3 planes (AP Point)

- Point > 3 Planes > Select Tibial Plafond, Anterior and AP planes > Apply > Ok



10. Extract Points: Origin, SI Point, AP Point

- Edit Features > Select Point > Copy XYZ positions to excel file



Geomagic Features:

- Zoom: roll middle mouse button
- Pan: Alt + middle mouse button
- Rotation: click and hold middle mouse button
- Use Axes Indicator in bottom right of screen for quick rotations about axes
- In Features tab, use Feature Visibility to toggle features on/off

Appendix C. Marker-based Static Tracking Error Results

Marker-based Static Rotational Tracking Error

	Calcaneus											
	Beads 1-2			Beads 2-3			Beads 1-3			Bone Average		
	Avg	±	SD	Avg	±	SD	Avg	±	SD	Avg	±	SD
25° Rotation	0.158	±	0.141	0.154	±	0.094	0.215	±	0.055	0.176	±	0.097
20° Rotation	0.062	±	0.039	0.295	±	0.043	0.054	±	0.037	0.137	±	0.040
15° Rotation	0.097	±	0.075	0.068	±	0.063	0.178	±	0.072	0.114	±	0.070
10° Rotation	0.268	±	0.050	0.075	±	0.042	0.049	±	0.035	0.131	±	0.042
5° Rotation	0.309	±	0.220	0.306	±	0.165	0.070	±	0.054	0.228	±	0.146
0° Rotation	0.217	±	0.113	0.182	±	0.098	0.055	±	0.040	0.151	±	0.083
-5° Rotation	0.093	±	0.035	0.132	±	0.032	0.107	±	0.026	0.111	±	0.031
-10° Rotation	0.034	±	0.029	0.036	±	0.026	0.080	±	0.033	0.050	±	0.030
-15° Rotation	0.064	±	0.035	0.026	±	0.022	0.027	±	0.020	0.039	±	0.026
-20° Rotation	0.157	±	0.040	0.079	±	0.047	0.130	±	0.053	0.122	±	0.047
-25° Rotation	0.141	±	0.072	0.082	±	0.061	0.050	±	0.035	0.091	±	0.056
Average	0.145	±	0.077	0.130	±	0.063	0.092	±	0.042	0.123	±	0.061

Marker-based Static Translational Tracking Error

	Calcaneus											
	Beads 1-2			Beads 2-3			Beads 1-3			Bone Average		
	Avg	±	SD	Avg	±	SD	Avg	±	SD	Avg	±	SD
Position 2,2	0.097	±	0.114	0.092	±	0.068	0.179	±	0.091	0.123	±	0.091
Position 3,1	0.142	±	0.077	0.443	±	0.145	0.106	±	0.038	0.231	±	0.087
Position 3,2	0.267	±	0.036	0.167	±	0.034	0.155	±	0.024	0.196	±	0.031
Position 3,3	0.342	±	0.048	0.070	±	0.032	0.096	±	0.019	0.169	±	0.033
Position 4,1	0.026	±	0.020	0.329	±	0.034	0.064	±	0.022	0.139	±	0.026
Position 4,2	0.027	±	0.022	0.022	±	0.017	0.059	±	0.028	0.036	±	0.023
Position 4,3	0.204	±	0.034	0.032	±	0.025	0.053	±	0.029	0.096	±	0.029
Position 4,4	0.035	±	0.036	0.063	±	0.039	0.123	±	0.036	0.074	±	0.037
Position 5,1	0.037	±	0.031	0.223	±	0.035	0.153	±	0.027	0.138	±	0.031
Position 5,2	0.113	±	0.033	0.095	±	0.029	0.166	±	0.026	0.125	±	0.029
Position 5,3	0.042	±	0.028	0.157	±	0.023	0.135	±	0.030	0.111	±	0.027
Position 5,4	0.355	±	0.036	0.231	±	0.027	0.062	±	0.025	0.216	±	0.029
Position 6,1	0.345	±	0.033	0.030	±	0.023	0.083	±	0.035	0.152	±	0.030
Position 6,2	0.331	±	0.057	0.036	±	0.049	0.061	±	0.030	0.143	±	0.045
Position 6,3	0.032	±	0.034	0.311	±	0.037	0.038	±	0.024	0.127	±	0.032
Position 6,4	0.184	±	0.046	0.253	±	0.040	0.069	±	0.036	0.169	±	0.040
Position 7,1	0.112	±	0.044	0.181	±	0.033	0.057	±	0.034	0.117	±	0.037
Position 7,2	0.089	±	0.032	0.227	±	0.027	0.081	±	0.034	0.132	±	0.031
Position 7,3	0.462	±	0.037	0.270	±	0.029	0.049	±	0.028	0.260	±	0.031
Position 7,4	0.043	±	0.034	0.494	±	0.106	0.291	±	0.035	0.276	±	0.058
Position 8,2	0.068	±	0.047	0.345	±	0.038	0.196	±	0.047	0.203	±	0.044

Position 8,3	0.043 ± 0.028	0.380 ± 0.032	0.275 ± 0.038	0.233 ± 0.033
Average	0.154 ± 0.041	0.202 ± 0.042	0.116 ± 0.033	0.157 ± 0.039

Marker-based Static Rotational Tracking Error

	Talus											
	Beads 4-5			Beads 5-6			Beads 4-6			Bone Average		
	Avg	±	SD	Avg	±	SD	Avg	±	SD	Avg	±	SD
25° Rotation	0.316	±	0.311	0.077	±	0.051	0.134	±	0.105	0.175	±	0.156
20° Rotation	0.222	±	0.145	0.195	±	0.101	0.330	±	0.103	0.249	±	0.117
15° Rotation	0.295	±	0.198	0.153	±	0.118	0.096	±	0.071	0.182	±	0.129
10° Rotation	0.142	±	0.133	0.165	±	0.115	0.092	±	0.064	0.133	±	0.104
5° Rotation	0.092	±	0.069	0.130	±	0.081	0.103	±	0.068	0.108	±	0.073
0° Rotation	0.158	±	0.089	0.089	±	0.075	0.085	±	0.061	0.111	±	0.075
-5° Rotation	0.188	±	0.039	0.341	±	0.085	0.381	±	0.087	0.304	±	0.070
-10° Rotation	0.183	±	0.035	0.049	±	0.033	0.050	±	0.040	0.094	±	0.036
-15° Rotation	0.042	±	0.030	0.042	±	0.036	0.055	±	0.035	0.046	±	0.034
-20° Rotation	0.109	±	0.082	0.226	±	0.046	0.165	±	0.072	0.167	±	0.067
-25° Rotation	0.106	±	0.076	0.293	±	0.137	0.210	±	0.128	0.203	±	0.114
Average	0.168	±	0.110	0.160	±	0.080	0.155	±	0.076	0.161 ± 0.088		

Marker-based Static Translational Tracking Error

	Talus											
	Beads 4-5			Beads 5-6			Beads 4-6			Bone Average		
	Avg	±	SD	Avg	±	SD	Avg	±	SD	Avg	±	SD
Position 2,2	0.104	±	0.065	0.071	±	0.060	0.101	±	0.071	0.092	±	0.065
Position 3,1	0.089	±	0.038	0.035	±	0.026	0.047	±	0.037	0.057	±	0.034
Position 3,2	0.134	±	0.033	0.053	±	0.038	0.159	±	0.056	0.115	±	0.042
Position 3,3	0.071	±	0.031	0.031	±	0.023	0.350	±	0.051	0.151	±	0.035
Position 4,1	0.037	±	0.025	0.260	±	0.039	0.063	±	0.038	0.120	±	0.034
Position 4,2	0.051	±	0.032	0.038	±	0.031	0.048	±	0.038	0.046	±	0.034
Position 4,3	0.154	±	0.044	0.121	±	0.048	0.103	±	0.044	0.126	±	0.045
Position 4,4	0.146	±	0.037	0.175	±	0.030	0.111	±	0.045	0.144	±	0.038
Position 5,1	0.047	±	0.030	0.137	±	0.047	0.044	±	0.033	0.076	±	0.037
Position 5,2	0.042	±	0.026	0.129	±	0.037	0.048	±	0.035	0.073	±	0.033
Position 5,3	0.146	±	0.051	0.108	±	0.063	0.106	±	0.047	0.120	±	0.054
Position 5,4	0.045	±	0.030	0.211	±	0.038	0.112	±	0.048	0.123	±	0.038
Position 6,1	0.466	±	0.159	0.168	±	0.041	0.347	±	0.049	0.327	±	0.083
Position 6,2	0.258	±	0.046	0.323	±	0.039	0.330	±	0.056	0.304	±	0.047
Position 6,3	0.338	±	0.045	0.141	±	0.055	0.186	±	0.079	0.222	±	0.060
Position 6,4	0.217	±	0.050	0.072	±	0.035	0.172	±	0.064	0.154	±	0.049
Position 7,1	0.135	±	0.042	0.333	±	0.046	0.058	±	0.043	0.175	±	0.044
Position 7,2	0.204	±	0.043	0.324	±	0.050	0.037	±	0.031	0.189	±	0.041
Position 7,3	0.149	±	0.040	0.207	±	0.045	0.059	±	0.044	0.139	±	0.043

Position 7,4	0.157 ± 0.046	0.154 ± 0.052	0.055 ± 0.040	0.122 ± 0.046
Position 8,2	0.090 ± 0.040	0.100 ± 0.048	0.140 ± 0.060	0.110 ± 0.049
Position 8,3	0.171 ± 0.042	0.099 ± 0.041	0.248 ± 0.061	0.173 ± 0.048
Average	0.148 ± 0.045	0.150 ± 0.042	0.133 ± 0.049	0.143 ± 0.045

Marker-based Static Rotational Tracking Error

	Tibia											
	Beads 7-8			Beads 8-9			Beads 7-9			Bone Average		
	Avg	±	SD	Avg	±	SD	Avg	±	SD	Avg	±	SD
25° Rotation	0.168	±	0.032	0.275	±	0.098	0.186	±	0.045	0.210	±	0.058
20° Rotation	0.167	±	0.052	0.076	±	0.061	0.055	±	0.036	0.099	±	0.050
15° Rotation	0.127	±	0.083	0.097	±	0.080	0.099	±	0.072	0.108	±	0.078
10° Rotation	0.398	±	0.060	0.110	±	0.088	0.091	±	0.074	0.199	±	0.074
5° Rotation	0.133	±	0.075	0.107	±	0.091	0.116	±	0.091	0.119	±	0.085
0° Rotation	0.079	±	0.051	0.106	±	0.072	0.087	±	0.070	0.091	±	0.064
-5° Rotation	0.165	±	0.030	0.050	±	0.037	0.109	±	0.039	0.108	±	0.035
-10° Rotation	0.117	±	0.025	0.312	±	0.045	0.118	±	0.037	0.182	±	0.036
-15° Rotation	0.063	±	0.028	0.260	±	0.045	0.233	±	0.039	0.185	±	0.037
-20° Rotation	0.069	±	0.045	0.267	±	0.084	0.075	±	0.055	0.137	±	0.061
-25° Rotation	0.065	±	0.058	0.393	±	0.097	0.258	±	0.103	0.239	±	0.086
Average	0.141	±	0.049	0.187	±	0.072	0.130	±	0.060	0.152 ± 0.060		

Marker-based Static Translational Tracking Error

	Tibia											
	Beads 7-8			Beads 8-9			Beads 7-9			Bone Average		
	Avg	±	SD	Avg	±	SD	Avg	±	SD	Avg	±	SD
Position 2,2	0.087	±	0.058	0.147	±	0.088	0.082	±	0.053	0.105	±	0.066
Position 3,1	0.253	±	0.029	0.231	±	0.095	0.151	±	0.059	0.212	±	0.061
Position 3,2	0.025	±	0.022	0.202	±	0.049	0.165	±	0.029	0.131	±	0.033
Position 3,3	0.265	±	0.021	0.124	±	0.042	0.277	±	0.033	0.222	±	0.032
Position 4,1	0.142	±	0.026	0.034	±	0.028	0.154	±	0.030	0.110	±	0.028
Position 4,2	0.116	±	0.030	0.232	±	0.065	0.229	±	0.039	0.193	±	0.045
Position 4,3	0.119	±	0.023	0.205	±	0.046	0.067	±	0.030	0.130	±	0.033
Position 4,4	0.068	±	0.027	0.261	±	0.059	0.242	±	0.034	0.190	±	0.040
Position 5,1	0.103	±	0.026	0.341	±	0.061	0.087	±	0.040	0.177	±	0.042
Position 5,2	0.133	±	0.030	0.277	±	0.057	0.066	±	0.033	0.159	±	0.040
Position 5,3	0.106	±	0.027	0.056	±	0.035	0.145	±	0.036	0.102	±	0.033
Position 5,4	0.066	±	0.027	0.191	±	0.051	0.049	±	0.045	0.102	±	0.041
Position 6,1	0.036	±	0.028	0.067	±	0.049	0.034	±	0.026	0.046	±	0.034
Position 6,2	0.048	±	0.027	0.055	±	0.041	0.042	±	0.032	0.048	±	0.033
Position 6,3	0.080	±	0.033	0.088	±	0.060	0.056	±	0.037	0.075	±	0.043
Position 6,4	0.049	±	0.027	0.203	±	0.148	0.129	±	0.115	0.127	±	0.097
Position 7,1	0.170	±	0.032	0.147	±	0.059	0.054	±	0.035	0.124	±	0.042

Position 7,2	0.041 ± 0.022	0.244 ± 0.060	0.177 ± 0.049	0.154 ± 0.044
Position 7,3	0.099 ± 0.038	0.356 ± 0.056	0.062 ± 0.039	0.172 ± 0.044
Position 7,4	0.135 ± 0.030	0.258 ± 0.057	0.091 ± 0.044	0.161 ± 0.044
Position 8,2	0.028 ± 0.023	0.078 ± 0.050	0.240 ± 0.045	0.116 ± 0.040
Position 8,3	0.108 ± 0.034	0.163 ± 0.052	0.056 ± 0.038	0.109 ± 0.041
Average	0.104 ± 0.029	0.180 ± 0.059	0.121 ± 0.042	0.135 ± 0.043

Marker-based Dynamic Tracking Error

	Calcaneus											
	Beads 1-2			Beads 2-3			Beads 1-3			Bone Average		
	Avg	±	SD	Avg	±	SD	Avg	±	SD	Avg	±	SD
Trial 1	0.340	±	0.184	0.234	±	0.133	0.157	±	0.137	0.243	±	0.152
Trial 2	0.221	±	0.147	0.105	±	0.052	0.182	±	0.090	0.169	±	0.096
Trial 3	0.391	±	0.163	0.080	±	0.059	0.107	±	0.082	0.192	±	0.101
Trial 4	0.491	±	0.221	0.093	±	0.076	0.128	±	0.088	0.237	±	0.128
Trial 5	0.164	±	0.168	0.324	±	0.071	0.207	±	0.094	0.232	±	0.111
Trial 6	0.340	±	0.157	0.115	±	0.098	0.154	±	0.127	0.203	±	0.128
Trial 7	0.537	±	0.133	0.214	±	0.093	0.075	±	0.066	0.275	±	0.097
Trial 8	0.269	±	0.200	0.123	±	0.096	0.147	±	0.112	0.180	±	0.136
Trial 9	0.152	±	0.155	0.244	±	0.126	0.294	±	0.128	0.230	±	0.136
Trial 10	0.341	±	0.180	0.099	±	0.105	0.146	±	0.066	0.195	±	0.117
Average	0.324	±	0.171	0.163	±	0.091	0.160	±	0.099	0.216	±	0.120

	Talus											
	Beads 4-5			Beads 5-6			Beads 4-6			Bone Average		
	Avg	±	SD	Avg	±	SD	Avg	±	SD	Avg	±	SD
Trial 1	0.182	±	0.196	0.137	±	0.109	0.154	±	0.094	0.158	±	0.133
Trial 2	0.168	±	0.196	0.149	±	0.138	0.138	±	0.120	0.152	±	0.152
Trial 3	0.215	±	0.159	0.098	±	0.079	0.189	±	0.116	0.167	±	0.118
Trial 4	0.309	±	0.233	0.257	±	0.178	0.308	±	0.166	0.291	±	0.192
Trial 5	0.212	±	0.142	0.148	±	0.092	0.161	±	0.121	0.173	±	0.118
Trial 6	0.137	±	0.111	0.125	±	0.097	0.184	±	0.138	0.149	±	0.115
Trial 7	0.194	±	0.153	0.115	±	0.087	0.150	±	0.111	0.153	±	0.117
Trial 8	0.255	±	0.170	0.125	±	0.100	0.223	±	0.165	0.201	±	0.145
Trial 9	0.215	±	0.167	0.258	±	0.136	0.309	±	0.188	0.260	±	0.164
Trial 10	0.123	±	0.211	0.242	±	0.232	0.206	±	0.178	0.190	±	0.207
Average	0.201	±	0.174	0.165	±	0.125	0.202	±	0.140	0.190	±	0.146

	Tibia											
	Beads 7-8			Beads 8-9			Beads 7-9			Bone Average		
	Avg	±	SD	Avg	±	SD	Avg	±	SD	Avg	±	SD
Trial 1	0.173	±	0.136	0.297	±	0.216	0.384	±	0.174	0.285	±	0.175
Trial 2	0.133	±	0.130	0.239	±	0.162	0.178	±	0.150	0.183	±	0.147
Trial 3	0.161	±	0.145	0.382	±	0.411	0.296	±	0.193	0.280	±	0.250
Trial 4	0.125	±	0.106	0.425	±	0.266	0.307	±	0.162	0.286	±	0.178

Trial 5	0.132 ± 0.091	0.293 ± 0.232	0.235 ± 0.163	0.220 ± 0.162
Trial 6	0.146 ± 0.134	0.329 ± 0.271	0.214 ± 0.172	0.229 ± 0.192
Trial 7	0.090 ± 0.066	0.310 ± 0.192	0.167 ± 0.122	0.189 ± 0.127
Trial 8	0.132 ± 0.104	0.249 ± 0.188	0.238 ± 0.163	0.206 ± 0.152
Trial 9	0.126 ± 0.101	0.285 ± 0.240	0.238 ± 0.281	0.217 ± 0.207
Trial 10	0.164 ± 0.227	0.236 ± 0.161	0.227 ± 0.169	0.209 ± 0.186
Average	0.138 ± 0.124	0.305 ± 0.234	0.248 ± 0.175	0.230 ± 0.178

Appendix D. Static Validation: Bias, Precision, RMS

Static Rotation Validation: Bias, Precision, RMS

Bias	Calcaneus: Beads 1-3			Talus: Beads 4-6			Tibia: Beads 7-9		
	X	Y	Z	X	Y	Z	X	Y	Z
25° Rotation	-0.02	0.02	-0.37	-0.53	-1.09	0.37	-0.24	0.35	0.17
20° Rotation	0.01	-0.25	-0.30	-0.30	-0.90	0.00	-0.06	0.48	0.02
15° Rotation	-0.14	-0.24	0.42	0.44	-0.63	0.30	0.01	-0.01	0.46
10° Rotation	-0.12	-0.11	-0.13	0.30	-0.86	0.33	-0.12	-0.28	0.15
5° Rotation	-0.53	0.75	-0.61	-0.67	-0.54	0.69	0.32	0.00	-0.03
0° Rotation	0.03	0.09	-0.10	0.18	0.08	0.89	-0.26	-0.06	-0.77
-5° Rotation	0.04	-0.31	-0.53	0.82	0.90	-0.11	0.04	-0.21	-0.19
-10° Rotation	0.29	-0.08	-0.37	-0.42	0.38	0.73	0.18	-0.32	-0.39
-15° Rotation	-0.30	-0.16	-0.06	0.10	-0.29	-1.07	0.00	0.21	-0.19
-20° Rotation	-0.07	0.08	-0.35	0.56	-0.21	-0.36	0.19	0.07	-0.14
-25° Rotation	-0.23	-0.02	-0.51	0.18	0.10	0.61	0.34	0.11	0.05
Average	-0.09	-0.02	-0.26	0.06	-0.28	0.22	0.04	0.03	-0.08
SD	0.21	0.29	0.29	0.48	0.61	0.57	0.20	0.25	0.32

Precision	Calcaneus: Beads 1-3			Talus: Beads 4-6			Tibia: Beads 7-9		
	X	Y	Z	X	Y	Z	X	Y	Z
25° Rotation	0.06	0.11	0.06	0.09	0.17	0.10	0.02	0.04	0.02
20° Rotation	0.07	0.14	0.12	0.09	0.16	0.09	0.04	0.06	0.03
15° Rotation	0.07	0.11	0.07	0.10	0.16	0.09	0.05	0.09	0.06
10° Rotation	0.04	0.07	0.03	0.07	0.15	0.08	0.05	0.08	0.05
5° Rotation	0.13	0.14	0.09	0.12	0.20	0.11	0.06	0.10	0.05
0° Rotation	0.05	0.09	0.05	0.07	0.12	0.07	0.05	0.08	0.14
-5° Rotation	0.02	0.04	0.02	0.03	0.06	0.03	0.02	0.04	0.02
-10° Rotation	0.08	0.06	0.09	0.08	0.07	0.08	0.02	0.04	0.02
-15° Rotation	0.02	0.04	0.03	0.12	0.32	0.13	0.02	0.04	0.02
-20° Rotation	0.03	0.06	0.03	0.07	0.10	0.05	0.05	0.07	0.05
-25° Rotation	0.06	0.09	0.05	0.08	0.13	0.06	0.06	0.10	0.05
Average	0.06	0.09	0.06	0.08	0.15	0.08	0.04	0.07	0.05
SD	0.03	0.04	0.03	0.02	0.07	0.03	0.02	0.03	0.04

RMS Error	Calcaneus: Beads 1-3			Talus: Beads 4-6			Tibia: Beads 7-9		
	X	Y	Z	X	Y	Z	X	Y	Z
25° Rotation	0.42	0.30	0.54	0.55	1.11	0.38	0.24	0.36	0.25
20° Rotation	0.62	0.78	0.34	0.32	0.91	0.48	0.13	0.49	0.07
15° Rotation	1.24	1.20	0.56	0.50	0.73	0.34	0.15	0.09	0.46
10° Rotation	0.86	1.00	0.23	0.32	0.88	0.35	0.18	0.30	0.16
5° Rotation	1.57	0.96	0.98	0.82	0.76	0.73	0.58	0.24	0.13
0° Rotation	0.18	0.14	0.49	0.45	0.72	0.89	0.28	0.13	0.79
-5° Rotation	0.58	0.93	0.53	0.82	0.90	0.17	0.38	0.35	0.20
-10° Rotation	1.17	0.91	0.66	0.43	0.62	0.73	0.54	0.44	0.39
-15° Rotation	0.65	1.10	0.43	1.17	0.97	1.08	0.06	0.21	0.19
-20° Rotation	0.41	1.16	0.57	1.24	0.93	0.51	0.20	0.21	0.15

-25° Rotation	0.24	1.11	0.54	0.80	0.68	0.62	0.34	0.17	0.13
Average	0.72	0.87	0.54	0.67	0.84	0.57	0.28	0.27	0.27
SD	0.44	0.35	0.19	0.32	0.15	0.27	0.17	0.13	0.21

Static Translation Validation: Bias, Precision, RMS

Bias	Calcaneus: Beads 1-3			Talus: Beads 4-6			Tibia: Beads 7-9		
	X	Y	Z	X	Y	Z	X	Y	Z
Position 2,2	0.19	0.67	-0.22	0.18	0.22	-0.51	0.17	0.10	0.02
Position 3,1	-0.21	-0.38	-0.51	-0.05	-0.25	-0.81	-0.03	0.08	0.15
Position 3,2	0.08	0.63	-0.31	0.25	0.53	0.10	0.04	0.11	0.35
Position 3,3	-0.14	-0.34	-0.37	0.15	0.67	0.94	0.29	-0.02	-0.16
Position 4,1	-0.25	-0.46	-0.02	-0.86	-1.46	-0.07	-0.02	-0.23	-0.49
Position 4,2	0.17	0.01	-0.24	0.02	0.38	0.19	0.05	-0.41	0.00
Position 4,3	-0.05	0.20	-0.56	-0.28	-0.38	0.63	0.14	0.41	-0.35
Position 4,4	-0.10	0.07	-0.49	0.57	1.02	-0.28	0.22	0.26	0.20
Position 5,1	-0.29	-0.70	0.05	0.11	0.42	0.02	0.06	-0.35	0.08
Position 5,2	0.17	0.25	-0.19	-0.25	0.51	0.07	-0.05	-0.08	0.30
Position 5,3	0.10	-0.25	0.14	-0.36	1.09	0.52	0.10	0.27	0.37
Position 5,4	0.08	0.26	-0.24	0.66	1.13	0.04	0.15	0.68	-0.10
Position 6,1	-0.07	-0.03	-0.04	-0.87	-0.27	0.24	-0.31	-0.60	0.22
Position 6,2	-0.02	0.08	0.01	0.05	-0.01	-0.06	0.06	-0.63	0.01
Position 6,3	0.20	0.12	0.12	0.45	0.12	0.15	0.07	-0.32	0.18
Position 6,4	0.03	0.49	0.04	0.46	0.40	-0.14	-0.19	0.06	-0.08
Position 7,1	0.05	-0.30	-0.02	0.23	0.23	-0.79	-0.11	-0.14	0.45
Position 7,2	-0.30	-0.87	0.01	0.76	1.70	0.18	0.07	-0.12	-0.05
Position 7,3	0.24	0.24	0.21	0.69	0.99	0.26	-0.01	-0.08	-0.34
Position 7,4	-0.27	-0.17	-0.49	0.37	-0.05	-0.27	-0.17	0.55	-0.10
Position 8,2	-0.38	-0.80	0.09	-0.52	-1.71	-0.25	-0.16	-0.25	0.11
Position 8,3	0.23	-0.30	-0.07	-0.05	-0.29	-0.34	-0.04	-0.17	-0.02
Average	-0.03	-0.03	-0.25	-0.05	0.25	0.07	0.09	0.01	0.04
SD	0.18	0.44	0.23	0.38	0.72	0.50	0.11	0.26	0.28

Precision	Calcaneus: Beads 1-3			Talus: Beads 4-6			Tibia: Beads 7-9		
	X	Y	Z	X	Y	Z	X	Y	Z
Position 2,2	0.09	0.11	0.09	0.13	0.12	0.06	0.07	0.09	0.06
Position 3,1	0.18	0.21	0.10	0.05	0.18	0.09	0.04	0.06	0.03
Position 3,2	0.04	0.04	0.06	0.07	0.08	0.08	0.02	0.03	0.02
Position 3,3	0.03	0.04	0.02	0.04	0.09	0.02	0.02	0.06	0.06
Position 4,1	0.05	0.04	0.04	0.03	0.04	0.05	0.02	0.03	0.01
Position 4,2	0.02	0.03	0.02	0.06	0.11	0.02	0.10	0.05	0.06
Position 4,3	0.05	0.34	0.07	0.04	0.06	0.02	0.02	0.03	0.02
Position 4,4	0.08	0.09	0.05	0.03	0.08	0.06	0.06	0.05	0.07
Position 5,1	0.05	0.05	0.09	0.04	0.06	0.03	0.02	0.04	0.02
Position 5,2	0.03	0.06	0.02	0.03	0.08	0.04	0.06	0.14	0.08
Position 5,3	0.18	0.41	0.17	0.05	0.09	0.05	0.05	0.04	0.02
Position 5,4	0.02	0.05	0.02	0.05	0.09	0.12	0.03	0.05	0.02
Position 6,1	0.26	0.18	0.20	0.03	0.05	0.03	0.03	0.05	0.03
Position 6,2	0.12	0.18	0.08	0.04	0.09	0.05	0.04	0.05	0.03

Position 6,3	0.10	0.08	0.03	0.04	0.07	0.04	0.04	0.06	0.02
Position 6,4	0.09	0.07	0.03	0.05	0.07	0.07	0.04	0.10	0.02
Position 7,1	0.03	0.05	0.02	0.03	0.06	0.06	0.02	0.04	0.02
Position 7,2	0.03	0.04	0.02	0.03	0.06	0.03	0.03	0.07	0.02
Position 7,3	0.09	0.06	0.03	0.05	0.08	0.06	0.02	0.04	0.06
Position 7,4	0.14	0.24	0.10	0.06	0.06	0.04	0.02	0.04	0.02
Position 8,2	0.04	0.07	0.03	0.04	0.08	0.03	0.02	0.05	0.07
Position 8,3	0.02	0.05	0.02	0.08	0.10	0.07	0.04	0.05	0.02
Average	0.07	0.13	0.07	0.05	0.09	0.05	0.04	0.06	0.04
SD	0.06	0.13	0.04	0.03	0.04	0.02	0.03	0.03	0.02

RMS Error	Calcaneus: Beads 1-3		
	X	Y	Z
Position 2,2	0.21	0.69	0.28
Position 3,1	0.33	0.50	0.52
Position 3,2	0.18	0.67	0.50
Position 3,3	0.42	0.81	0.49
Position 4,1	0.28	1.36	1.00
Position 4,2	0.28	0.75	0.52
Position 4,3	0.88	1.23	0.61
Position 4,4	0.42	1.25	0.76
Position 5,1	0.30	0.70	0.35
Position 5,2	0.78	1.56	0.52
Position 5,3	0.27	0.67	0.28
Position 5,4	0.24	0.62	0.44
Position 6,1	0.40	0.41	0.27
Position 6,2	0.27	0.28	0.29
Position 6,3	0.36	0.50	0.69
Position 6,4	0.31	0.74	0.29
Position 7,1	1.14	1.74	0.52
Position 7,2	0.31	0.87	0.12
Position 7,3	0.38	0.77	0.46
Position 7,4	0.30	0.86	0.69
Position 8,2	0.38	0.91	0.42
Position 8,3	0.23	0.34	0.51
Average	0.39	0.83	0.48
SD	0.24	0.38	0.20

Talus: Beads 4-6		
X	Y	Z
0.22	0.35	0.52
0.17	0.92	0.82
0.28	0.53	0.23
0.19	1.18	0.94
0.87	1.46	0.28
0.09	0.40	0.20
0.28	0.45	0.63
0.57	1.02	0.29
0.24	0.43	0.07
0.25	0.63	0.26
0.38	1.10	0.53
0.66	1.14	0.19
0.87	0.60	0.24
0.14	0.31	0.10
0.45	0.43	0.16
0.47	0.41	0.23
0.23	0.90	0.86
0.76	1.70	0.19
0.69	1.00	0.27
0.37	0.26	0.28
0.52	1.71	0.25
0.13	0.43	0.46
0.40	0.79	0.36
0.24	0.45	0.25

Tibia: Beads 7-9		
X	Y	Z
0.26	0.17	0.08
0.18	0.12	0.16
0.05	0.12	0.35
0.84	0.28	0.34
0.19	0.23	0.49
0.39	0.42	0.07
0.14	0.41	0.35
0.23	0.28	0.22
0.35	0.43	0.11
0.12	0.19	0.31
0.18	0.27	0.37
0.21	0.68	0.13
0.31	0.60	0.22
0.16	0.63	0.08
0.16	0.32	0.18
0.26	0.18	0.09
0.11	0.15	0.45
0.28	0.18	0.33
0.44	0.09	0.36
0.24	0.55	0.11
0.21	0.25	0.14
0.14	0.22	0.26
0.25	0.31	0.24
0.16	0.18	0.13

Appendix E. Dynamic Validation: Bias, Precision, RMS

Bias	Calcaneus: Beads 1-3			Talus: Beads 4-6			Tibia: Beads 7-9		
	X	Y	Z	X	Y	Z	X	Y	Z
Trial 1	-0.09	-0.32	-0.25	0.13	-0.06	-0.07	-0.16	-0.46	-0.08
Trial 2	0.15	-0.33	-0.10	-0.12	0.03	-0.13	0.07	-0.08	-0.30
Trial 3	0.23	0.01	-0.47	-0.24	0.00	-0.19	0.12	-0.20	-0.31
Trial 4	0.00	-0.23	-0.67	-0.14	-0.08	-0.19	-0.13	-0.05	-0.31
Trial 5	0.15	-0.19	-0.17	-0.19	-0.04	-0.20	-0.10	-0.41	-0.30
Trial 6	0.00	-0.27	-0.17	-0.14	0.21	0.37	0.11	0.02	-0.20
Trial 7	-0.04	-0.30	-0.36	-0.15	0.02	0.05	0.07	-0.22	-0.12
Trial 8	0.12	0.05	-0.18	0.06	0.19	-0.28	0.23	0.11	-0.21
Trial 9	-0.03	-0.07	-0.45	-0.04	-0.23	0.61	0.01	0.08	-0.14
Trial 10	-0.06	-0.67	-0.20	0.25	-0.51	-0.13	0.12	0.27	-0.21
Average	0.05	-0.23	-0.30	-0.06	-0.05	-0.02	0.03	-0.09	-0.22
SD	0.11	0.21	0.18	0.16	0.21	0.29	0.13	0.23	0.09

Precision	Calcaneus: Beads 1-3			Talus: Beads 4-6			Tibia: Beads 7-9		
	X	Y	Z	X	Y	Z	X	Y	Z
Trial 1	0.53	0.85	0.44	0.32	0.70	0.41	0.36	0.47	0.35
Trial 2	0.39	0.65	0.46	0.30	0.54	0.40	0.31	0.40	0.36
Trial 3	1.03	1.71	1.02	0.36	0.72	0.36	0.31	0.47	0.34
Trial 4	0.94	1.56	0.87	0.40	0.73	0.44	0.49	0.46	0.33
Trial 5	0.60	1.08	0.65	0.36	0.71	0.33	0.30	0.36	0.31
Trial 6	0.41	0.86	0.71	0.29	0.68	0.32	0.33	0.38	0.40
Trial 7	0.93	1.36	0.71	0.47	0.93	0.51	0.35	0.32	0.53
Trial 8	0.65	1.34	0.72	0.41	1.00	0.42	0.34	0.40	0.43
Trial 9	0.77	1.33	0.60	0.42	0.71	0.45	0.51	0.56	0.41
Trial 10	0.72	1.14	0.77	0.40	0.74	0.38	0.46	0.42	0.46
Average	0.70	1.19	0.69	0.37	0.75	0.40	0.38	0.42	0.39
SD	0.22	0.33	0.17	0.06	0.13	0.06	0.08	0.07	0.07

RMS Error	Calcaneus: Beads 1-3			Talus: Beads 4-6			Tibia: Beads 7-9		
	X	Y	Z	X	Y	Z	X	Y	Z
Trial 1	0.77	1.06	0.58	0.32	0.71	0.43	0.40	0.56	0.31
Trial 2	0.45	0.65	0.52	0.30	0.51	0.36	0.29	0.43	0.45
Trial 3	0.81	1.33	0.95	0.39	0.64	0.37	0.30	0.46	0.38
Trial 4	0.80	1.26	0.90	0.39	0.64	0.53	0.47	0.48	0.44
Trial 5	0.76	1.24	0.59	0.40	0.72	0.46	0.32	0.51	0.42
Trial 6	0.56	1.02	0.66	0.31	0.66	0.45	0.34	0.40	0.43
Trial 7	0.87	0.98	0.77	0.34	0.87	0.41	0.31	0.38	0.40
Trial 8	0.67	1.11	0.70	0.40	0.96	0.51	0.41	0.45	0.45
Trial 9	0.64	1.08	0.73	0.39	0.73	0.67	0.38	0.55	0.41
Trial 10	0.70	1.34	0.73	0.44	0.89	0.40	0.45	0.49	0.49
Average	0.70	1.11	0.71	0.37	0.73	0.46	0.37	0.47	0.42
SD	0.13	0.21	0.14	0.05	0.14	0.09	0.06	0.06	0.05

Appendix F. User Error: Bias, Precision, RMS

Bias	Manual: Tibia				Automated: Tibia			
	X	Y	Z	Overall	X	Y	Z	Overall
Trial 4: Repeat 1	0.17	0.45	0.46	0.36	0.06	0.23	-0.01	0.09
Trial 4: Repeat 2	0.23	0.31	0.14	0.23	0.06	0.20	-0.17	0.03
Trial 4: Repeat 3	-0.03	0.22	0.24	0.14	0.06	0.19	-0.18	0.02
Trial 4: Repeat 4	0.19	0.47	-0.05	0.21	-0.07	0.20	-0.17	-0.01
Trial 4: Repeat 5	0.15	0.36	0.06	0.19	0.01	0.19	-0.23	-0.01
Trial 4: Repeat 6	0.17	0.23	0.18	0.19	0.00	0.19	-0.18	0.00
Trial 4: Repeat 7	0.19	0.44	0.18	0.27	-0.02	0.20	-0.24	-0.02
Trial 4: Repeat 8	0.20	0.56	0.04	0.27	0.01	0.23	-0.22	0.01
Trial 4: Repeat 9	0.18	0.37	0.10	0.22	0.02	0.17	-0.19	0.00
Trial 4: Repeat 10	0.14	0.36	0.17	0.22	0.06	0.14	-0.14	0.02
Average	0.16	0.38	0.15	0.23	0.02	0.19	-0.17	0.01
SD	0.07	0.11	0.14	0.11	0.04	0.03	0.07	0.05

Precision	Manual: Tibia				Automated: Tibia			
	X	Y	Z	Overall	X	Y	Z	Overall
Trial 4: Repeat 1	0.42	0.54	0.73	0.56	0.46	0.46	0.68	0.54
Trial 4: Repeat 2	0.39	0.47	0.56	0.47	0.46	0.45	0.64	0.51
Trial 4: Repeat 3	0.39	0.54	0.51	0.48	0.49	0.49	0.68	0.55
Trial 4: Repeat 4	0.41	0.46	0.38	0.42	0.61	0.48	0.71	0.60
Trial 4: Repeat 5	0.37	0.41	0.52	0.43	0.54	0.46	0.73	0.58
Trial 4: Repeat 6	0.39	0.52	0.60	0.50	0.55	0.49	0.69	0.57
Trial 4: Repeat 7	0.40	0.48	0.58	0.49	0.48	0.49	0.62	0.53
Trial 4: Repeat 8	0.41	0.57	0.70	0.56	0.58	0.60	0.70	0.63
Trial 4: Repeat 9	0.45	0.65	0.75	0.62	0.54	0.58	0.70	0.61
Trial 4: Repeat 10	0.46	0.50	0.50	0.48	0.53	0.51	0.65	0.57
Average	0.41	0.51	0.58	0.50	0.52	0.50	0.68	0.57
SD	0.03	0.07	0.12	0.07	0.05	0.05	0.04	0.05

RMS Error	Manual: Tibia				Automated: Tibia			
	X	Y	Z	Overall	X	Y	Z	Overall
Trial 4: Repeat 1	0.42	0.67	0.58	0.55	0.45	0.56	0.65	0.55
Trial 4: Repeat 2	0.45	0.59	0.69	0.58	0.47	0.53	0.63	0.54
Trial 4: Repeat 3	0.41	0.66	0.67	0.58	0.52	0.57	0.65	0.58
Trial 4: Repeat 4	0.45	0.67	0.62	0.58	0.42	0.54	0.59	0.52
Trial 4: Repeat 5	0.37	0.56	0.61	0.51	0.51	0.54	0.67	0.58
Trial 4: Repeat 6	0.42	0.61	0.60	0.55	0.55	0.58	0.64	0.59
Trial 4: Repeat 7	0.45	0.68	0.64	0.59	0.51	0.59	0.67	0.59
Trial 4: Repeat 8	0.46	0.78	0.65	0.63	0.48	0.65	0.69	0.60
Trial 4: Repeat 9	0.50	0.70	0.66	0.62	0.55	0.60	0.66	0.60
Trial 4: Repeat 10	0.44	0.62	0.59	0.55	0.49	0.56	0.64	0.56
Average	0.44	0.65	0.63	0.57	0.50	0.57	0.65	0.57
SD	0.03	0.06	0.04	0.04	0.04	0.04	0.03	0.03